

Online Decision Analytics with Deep Learning: Non-invasive Fever Screening

by

CHIN, Jing Wei

A Thesis Submitted to
The Hong Kong University of Science and Technology
In Partial Fulfillment of the Requirements for
The Degree of Doctor of Philosophy
In Industrial Engineering and Logistics Management

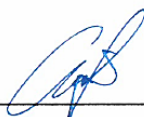
July 2021, Hong Kong

Authorization

I hereby declare that I am the sole author of the thesis.

I authorize the Hong Kong University of Science and Technology to lend this thesis to other institutions or individuals for the purpose of scholarly research.

I further authorize the Hong Kong University of Science and Technology to reproduce the thesis by photocopying or by other means, in total or in part, at the request of other institutions or individuals for the purpose of scholarly research.

A handwritten signature in blue ink, appearing to be 'CHIN, Jing Wei', is positioned above a horizontal line.

CHIN, Jing Wei

13 July 2021

Online Decision Analytics with Deep Learning:
Non-invasive Fever Screening

by

CHIN, Jing Wei

This is to certify that I have examined the above PhD thesis
and have found that it is complete and satisfactory in all respects,
and that any and all revisions required by
the thesis examination committee have been made.



Professor Richard H.Y. SO (Supervisor)



Professor Guillermo GALLEGO (Head of the Department)

Department of Industrial Engineering and Decision Analytics

13 July 2021

Acknowledgement

First and foremost, I would like to express my great appreciation to my supervisor Professor Richard H. Y. SO, who has been very supportive, understanding, and caring throughout my doctoral study. His willingness to offer his time, guidance on both research and life journeys have been very much appreciated. Without his guidance and advice, this thesis would not be possible. Thank you!

I want to thank my thesis defense committee members: Prof. Ravindra Stephen GOONETILLEKE, Prof. Ning CAI, Prof. Ajay JONEJA, Prof. Bertram Shi, and Prof George BACIU. Thank you for all the comments and guidance.

I would also like to thank our department staff and the lab technicians: Ms. Fona WONG, Ms. Joyce CHAN, Ms. Vera LI, Ms. Winnie CHOY, Mr. Denil, Mr. Yong, Mr. Tin, and Ms. Peggy MAK. Thank you for the various help provided throughout my study.

I am grateful to my colleagues and friends at HKUST. Special thanks to Kyle WONG, Teric CHAN, Kristian SUHARTONO, Eddie LAU, MEN Yixin, and Phoebe CHING for their help on the EMSD project. We worked very hard together and had been through tough times together. In addition, I would like to thank my close friends during my Ph.D. study, Dr. Guangyuan ZHANG, Dr. Xuhan TIAN, Prof. Pi-Ying YEN, and Dr. Tingyi WANG. We had terrific times studying and playing together. They are amazing companions! I wish them luck and all the best in their future career, please keep in touch. Furthermore, I would like to thank my research lab members for various supports on the EMSD project and the RFSS systems installed on the HKUST campus. They have been friendly and helpful. After that, I also want to thank my badminton friends. They have offered loads of fun throughout my study. Thank you.

Most importantly, I am thankful for my family members: CHIN Yoong Keong, YIP Sow Fong, CHIN Rui Yi, and CHIN Jing Yi, for their unconditional love and support. Last but not least, my girlfriend, Dr. Xiaojin Fu, words cannot express how grateful I am to her, the one who has been loving me and taking care of me, especially during the most challenging times in 2020. Thank you!

Table of Contents

Title Page.....	i
Authorization Page.....	ii
Signature Page.....	iii
Acknowledgements.....	iv
Table of Contents.....	v
List of Figures.....	viii
List of Tables.....	xii
Abstract.....	xiii
Chapter 1 INTRODUCTION.....	1
Summary.....	1
1.1 Background and Motivation.....	1
1.2 Contributions.....	2
1.3 Thesis Organization.....	4
Chapter 2 LITERATURE REVIEW.....	6
Summary.....	6
2.1 Principles of Infrared Thermography (IRT) and Temperature Measurement.....	6
2.2 Temperature Screening.....	8
2.3 Human and Face Detection.....	8
2.4 Object Tracking.....	10
2.5 Person Re-identification (ReID).....	10
2.6 Research Gaps.....	11
Chapter 3 STUDY ONE: EFFECTS OF DISTANCE ON NON-INVASIVE TEMPERATURE SCREENING 13	
Summary.....	13
3.1 Introduction.....	13
3.2 Hypothesis.....	13
3.3 Method.....	14
3.4 Results and Analysis.....	17
3.5 Discussion and Conclusion.....	27
Chapter 4 STUDY TWO: EFFECTS OF AMBIENT TEMPERATURE ON NON-INVASIVE TEMPERATURE SCREENING.....	28
Summary.....	28

4.1	Introduction	28
4.2	Method	28
4.3	Results and Analysis.....	45
4.4	Discussion and Conclusion.....	55
Chapter 5	STUDY THREE: REDUCTION OF NOISE IN NON-INVASIVE TEMPREATURE MEASUREMENT WITH HUMAN TRACKING.....	57
	Summary	57
5.1	Introduction	57
5.2	Method	57
5.3	Results and Analysis.....	61
5.4	Discussion and Conclusion.....	66
Chapter 6	STUDY FOUR: ONLINE DECISION ANALYTICS SYSTEM: LIVE-STREAMING AI FEVER SCREENING SYSTEM	67
	Summary	67
6.1	Introduction	67
6.2	Data and Design Requirements	67
6.3	System Architecture and Design	68
6.4	Multi-person Loading Test and Mass Temperature Screening ($N \geq 40$)	78
6.5	Role-play Simulation	79
6.6	Benchmark Results	81
6.7	Deployments of Live-Streaming AI Fever Screening System in the Public.....	82
6.8	User Surveys and Feedbacks	93
6.9	Discussions and Conclusions	93
Chapter 7	CONCLUSIONS, LIMITATIONS AND FUTURE WORKS	95
7.1	Conclusions	95
7.2	Limitations and Future Works	97
	REFERENCE.....	99
	Appendix	104
3.1	Hardware Specifications of RFSS	104
3.2	Infrared Thermometer FS-300	108
3.3	Hot patches	108
3.4	Code for the analysis (the effects of distance, ambient temperature, and tracking) .	108
3.5	Analysis of the effects of distance	109
4.1	Face box estimation with Open-Pose	110

4.2 Motion filter	110
4.3 Data calibration at HKUST North Gate.....	111
4.4 Analysis of the effects of ambient temperature.....	112
6.1 Equipment list	113
6.2 Thermal block.....	114
6.3 RFSS User feedbacks	115

List of Figures

Figure 1-1: Thesis structure.	5
Figure 1-2: An overview of the thesis research.	5
Figure 2-1: A General Model of Radiation for Temperature Measurement	7
Figure 3-1: An experiment setup using our Remote Fever Screening System (RFSS). Temperature measurements were recorded throughout the whole experiment.....	14
Figure 3-2: A photo of the experiment setup using Remote Fever Screening System (RFSS).	15
Figure 3-3: The ambient temperature and humidity recorded during the experiment. The mean ambient temperature was 23.46°C and the mean humidity was 77.62%.....	17
Figure 3-4: Temperature Measurements using a FLIR E8. Data shows that the temperature drops linearly when the sensor-subject distance increases.	18
Figure 3-5: Temperature Distribution of the Normal and Reference Fever Group.....	19
Figure 3-6: (a) Temperature measurements measured using a FLIR E8. (b) Temperature measurements measured using a FLIR A315.	20
Figure 3-7: The error reduces with our thermal compensation.	24
Figure 3-8: Temperature distribution of the normal group and reference fever group with and without thermal compensation.	25
Figure 3-9: Sensitivity and specificity of fever screening with and without thermal compensation.	26
Figure 4-1: Distance estimation using the diagonal length of face box on the collected field data at HKUST North Gate.	30
Figure 4-2. 3D plot of the peak temperature with respect to the distance and ambient temperature collected at HKUST's north gate entrance over 5 months.	31
Figure 4-3: NG data after distance filtering.	33
Figure 4-4: NG data after removing the unsynchronized data	35
Figure 4-5: NG data after removing the extremely long and wide faces.	37
Figure 4-6: Remaining data after the patch filtering removes the people who are not showing their forehead.	39
Figure 4-7: Remaining data after head orientation filtering removes the people who are not front-facing.	41

Figure 4-8: Remaining data after the temperature filtering removes the data with temperature lower than 20°C and higher than 40°C.....	43
Figure 4-9: Data visualization before and after the data filtering. There is a more apparent pattern shown in the filtered data.	45
Figure 4-10: Temperature measurement comparison of the field data and the experimental data over distances at 23.5°C ambient temperature.....	46
Figure 4-11: Example of the thermal faces under 23.5°C ambient temperature.	47
Figure 4-12: Temperature measurement over distance in different ambient temperatures.	48
Figure 4-13: Temperature measurement over ambient temperature at different distances.	49
Figure 4-14: A drop in ambient temperature from 28°C to 14°C reduces the non-invasive temperature measurements by 4.1°C to 7.2°C on average, depending on the distance.	50
Figure 4-15: 3D visualization of the measured temperature and the compensated temperature versus distance and ambient temperature. (a) Training data. (b) Testing data.	52
Figure 4-16: Reference fever data extrapolated to different ambient temperatures	53
Figure 4-17: Sensitivity and specificity of fever screening with and without our thermal compensation at different distances and different ambient temperatures.	55
Figure 5-1: Temporal information of the subject with ID 397. Back-facing the camera causes the measured temperature to be much lower than an average human temperature. Utilizing temporal information can suppress the noise due to back-facing.....	60
Figure 5-2: Temporal information of the subject with ID 5250. A typical subject walked towards and left the field of view of our system.....	61
Figure 5-3: The effects of percentile of the valid historical temperature distribution chosen for temperature estimation.	62
Figure 5-4: The analysis of the percentile of the valid historical temperature distribution chosen for temperature estimation. (a) The kurtosis and skewness of the temperature distribution of 53 subjects with different percentile chosen. (b) The percentage of the passersby having fever. (c) The mean and median temperature of the passersby.	63
Figure 5-5: The mean and distribution of the percentage of duration with valid temperature measurement. There is a low percentage of duration with valid temperature measurement before any treatment on the raw measured temperature. The percentage of duration increases to 89.36% with treatment 1 (applied our thermal compensation) and further	

increases to 98.61% with treatment 2 (applied our thermal compensation and human tracking).	64
Figure 5-6: Comparing with no treatment, root-mean-square error (RMSE) decreases with treatment 1 and further decreases with treatment 2. Results show that our thermal compensation and the human tracking improve the accuracy of non-invasive temperature measurement.....	65
Figure 6-1: Hardware Connection Diagram	69
Figure 6-2: Software Architecture of Smart Fever Screening System (SFSS).....	70
Figure 6-3: Software Stack of SFSS.....	71
Figure 6-4: System Diagram	72
Figure 6-5: ReID Network Structure.....	76
Figure 6-6: Examples of data stored in database.	77
Figure 6-7: Example of user interface (UI) of our system. The left part of the photo shows the UI on the mobile phones and tablet PC, the right part of the photo shows the UI in the web application on the desktop PC or laptop.	78
Figure 6-8: Mass temperature screening for moving crowds with our system ($N \geq 40$).	79
Figure 6-9: The setup for measuring the response time of the SFSS and the conventional TIS	81
Figure 6-10: Our system detects fever suspects in a shorter time consistently	82
Figure 6-11: The locations of our deployed systems	83
Figure 6-12: The Installations of the SFSS at the Hong Kong International Airport (HKIA)	84
Figure 6-13: The Installation of the SFSS at the Kai Tak Cruise Terminal (KTCT).....	85
Figure 6-14: Our system at Hong Kong International School (HKIS)	86
Figure 6-15: The Salvation Army William Booth Secondary School, The Salvation Army Shek Wu School, The Salvation Army Lam Butt Chung Memorial School, The Salvation Army Tin Ka Ping School.....	87
Figure 6-16: Five elderly daycare centers	88
Figure 6-17: Tsing Yi Public Library and Tiu Keng Leng Public Library	89
Figure 6-18: The installation of our system at the entrance of science museum	90
Figure 6-19: The installation at a government building and one of the border control points	91

Figure 6-20: The installation at HKUST: Lee Shau Kee Business Building, South Gate, North Gate, Atrium, Cheng Yu Tung Building, and the HKUST Library	92
Figure 6-21: The survey results regarding to our technology and system.	93

List of Tables

Table 1: A list of variables in study one	16
Table 2: The Pearson Correlation, Mean Absolute Error and Root Mean Square Error comparison between the Measured Temperature and Compensated Temperature vs the Reference Temperature.....	23
Table 3: A list of variables in study two	29
Table 4: Examples of discarded thermal faces by the distance filter and the remaining data	34
Table 5: Example of the thermal faces removed by the second set of filters and the remaining data. The second set of filters keeps the thermal faces with more than 80% active thermal pixels, and the hottest pixel on the face does not lie on the edges of the face.	36
Table 6: Example of the long and wide discarded thermal faces discarded by the filter and the remaining data	38
Table 7: Example of discarded thermal faces by the patch filter, and the remaining thermal faces show more of the forehead region.	40
Table 8: Example of discarded thermal faces by head orientation filter to remove people who are not facing forward, there is a higher chance of having forward-facing thermal faces in the remaining data.....	42
Table 9: Example of thermal faces not in the range of 20°C to 40°C and the remaining thermal faces.	44
Table 10: Mean Absolute Error and Root Mean Square Error comparison between the measured temperature and compensated temperature vs the reference temperature	51
Table 11: Comparison of the temperature screening distance ($\geq 90\%$ sensitivity and specificity) with and without our thermal compensation.	55

Online Decision Analytics with Deep Learning: Non-invasive Fever Screening

By CHIN, Jing Wei

Department of Industrial Engineering and Decision Analytics
The Hong Kong University of Science and Technology

Abstract

Research in artificial intelligence (AI) has focused on performance advancement while sacrificing consideration for real-time applications. Consequently, online decision-analytic systems utilizing multiple AI computer vision algorithms to replace human decisions receive less attention. This dissertation reports the design, implementation, and study of a live-streaming AI fever screening system (LAFSS) to replace human decisions. The LAFSS addresses four major challenges of designing an online-decision analytic system on fever screening.

The first challenge is the difficulty in long-distance non-invasive temperature screening. In current practice, temperature screening with Infrared Thermography (IRT) is limited to a narrow distance range for febrile detection to bypass the inaccuracies due to the distance. Results show that our novel proposed model can compensate for the loss due to the effects of distance and extends the temperature screening distance in a controlled thermal environment. The second challenge is the influence of ambient temperature on long-distance temperature screening. Data shows that our system can compensate for the effects of distance and ambient temperature for semi-outdoor temperature screening. This system is also the first of its kind.

Moreover, we study the possibility of noise suppression in non-invasive temperature measurement with human tracking. Our study shows that the temporal information by human tracking suppresses the noise effectively. Last but not least, the fourth challenge is the design and implementation of a large-scale real-time fever screening system with multiple AI. Our system can detect febrile people in a moving crowd and track them across multiple cameras in real-time. LAFSS has been designed, implemented, and deployed in multiple cross-border checkpoints, libraries, schools, and elderly centers. Finally, lessons learned are discussed to facilitate more real-time implementation of AI algorithms, especially on non-invasive temperature screening applications.

Chapter 1 INTRODUCTION

Summary

The background of the study, challenges, and research problems are briefly introduced in this chapter. The main contributions are summarized, and the thesis structure is presented at the end of the chapter.

1.1 Background and Motivation

Human body temperature has been one of the good vital indicators for health. Elevated body temperature or fever has often been associated with a physical illness caused by infectious diseases. To prevent the spreading of diseases, Thermal Imaging System (TIS) for mass fever screening has been promising [1]–[3] since the outbreak of severe acute respiratory syndrome (SARS) back in almost two decades ago.

As a measure of health screening of travelers entering HKSAR borders, the Department of Health set up Infrared camera stations at the border control points with “eye-ball” checking. If a suspect is identified from watching the thermal images captured by the camera, they will approach them to get a second confirmation using handheld thermal infrared guns. However, the current incessant “eye-ball” checking procedure requires high concentration and can be tiring. This step can also attract human errors. In addition, as there is no means to capture the pictures of the suspects and track their locations once they walked past the checking points, the staff is under constant pressure to react immediately. Consequently, this can impose heavy stress on the operators concerned throughout the entire shift.

With the advancement of artificial intelligence (AI) technologies in the computer vision field, it is possible to replace the tedious round-the-clock “eye-ball” checking tasks with a real-time decision analytics system that adopts these state-of-the-art computer vision technologies. However, there are several challenges to be resolved. Firstly, automatic fever suspect detection in a moving crowd using video analytics techniques is non-trivial. Human operators exploit their experiences to analyze different information to identify and track the fever suspects easily. However, it is challenging and non-trivial to replicate this ability using machines. Accurate detection of febrile persons requires precise human or face detection in a color video stream and association of the temperature information and other inputs. The second challenge is the tracking and localization of the febrile persons. Occlusion has been

one of the challenges in the video analytics community and yet to be solved. Finally, the effect of many factors on the non-invasive temperature measurements of the thermal cameras vastly affects the results of the online decision analytics system. Hence, this is also the most crucial factor for the success of the system.

This thesis explores the challenges in designing an online decision analytics system that consists of multiple deep learning techniques to replace complex human decisions in time-critical daily operations. To be precise, our objective is to study the problems and potential solutions for fever screening in a moving crowd. We introduced two thermal compensation models to confront the distance effect and environmental effects on temperature measurement for temperature screening. Furthermore, we investigated the feasibility of noise suppression using human subject tracking. Last but not least, we proposed a novel Online Decision Analytics System (ODAS) for efficient preliminary mass fever screening.

1.2 Contributions

In this thesis, we proposed novel thermal compensation models to improve non-invasive temperature measurements and fever screening. In addition, our study showed that temporal information with human subject tracking suppresses measurement noise to improve the accuracy and robustness of non-invasive temperature measurements and screening. Finally, a novel patent-protected Online Decision Analytics System (ODAS) has been developed, site-tested, and deployed. The main contributions of this thesis are as follows:

I. Effects of Distance

- a. Increasing distance reduces non-invasive temperature measurements significantly in a linear fashion.
- b. Without compensation, fever (1 C elevation) screening with $\geq 90\%$ sensitivity and specificity can only be achieved within 3.2m or closer.
- c. With our proposed model and compensation, the range of fever screening with $\geq 90\%$ sensitivity and specificity is increased to 8.2m.

II. Effects of Ambient Temperature

- a. Decreasing ambient temperature significantly reduces non-invasive temperature measurements linearly.
- b. A drop in ambient temperature from 28°C to 14°C can reduce non-invasive temperature measurements by 4.1°C to 7.2°C on average, depending on the distance.
- c. There is significant interaction between the effects of distance and ambient temperature on non-invasive temperature measurements.
- d. Results show that it is impossible to detect fever with $\geq 90\%$ sensitivity and specificity with changing ambient temperature.
- e. With our proposed model and compensation, it enables fever screening at different ambient temperatures and achieves $\geq 90\%$ sensitivity and specificity up to 6.8m in 17.5°C ambient temperature.

III. Further enhancements with human tracking

- a. With compensation on distance (0.9m – 24.4m) and ambient temperature (26.7°C to 28.9°C) effects, the duration of having valid temperature measurement increases to 89.36%, and root mean square error (RMSE) decreases to 0.87°C.
- b. With compensation on distance and ambient temperature effect + human tracking, the duration of having valid temperature measurement increases to 98.61%, and RMSE decreases to 0.43°C.
- c. Our study shows that temporal information suppresses noise in non-invasive temperature measurements.

IV. Test trial of a novel deep learning-based non-invasive temperature screening system

- a. A novel patent-protected Online Decision Analytics System (ODAS) utilizing multiple AI in computer vision on non-invasive fever screening (SFSS & RFSS) has been developed, site-tested, and deployed.
- b. Our study shows that our system detects fever suspects in a shorter time significantly compare to conventional Thermal Imaging System (TIS) and requires less human resources for the operation. Findings validated by EMSD and DH.
- c. User Acceptances of deployments in various public locations in Hong Kong: five schools, three libraries, one Non-Governmental Organization (NGO), 1 museum, nine elderly centers, the Electrical and Mechanical Services Department (EMSD), and the Department of Health of the HKSAR Government (various border control points). Positive feedbacks have been received.

1.3 Thesis Organization

The thesis structure is as follows:

Chapter 1 introduces the background and motivation of the study and summarizes the thesis contributions.

Chapter 2 summarizes the literature reviews on non-invasive temperature measurement and the state-of-the-art AI algorithms on human detection and tracking.

Chapter 3 is about the study on the effects of distance on non-invasive temperature measurements and fever screening.

Chapter 4 documents the study on the effects of ambient temperature on non-invasive temperature measurements and fever screening.

Chapter 5 studies the possibility of noise suppression in temperature measurement with temporal information by human subject tracking.

Chapter 6 details the design and the deployment of the online decision analytics system on fever screening in moving crowds.

Chapter 7 concludes the thesis and details possible future works.

Figure 1-1 shows the thesis structure, and Figure 1-2 shows the overview of the thesis research.

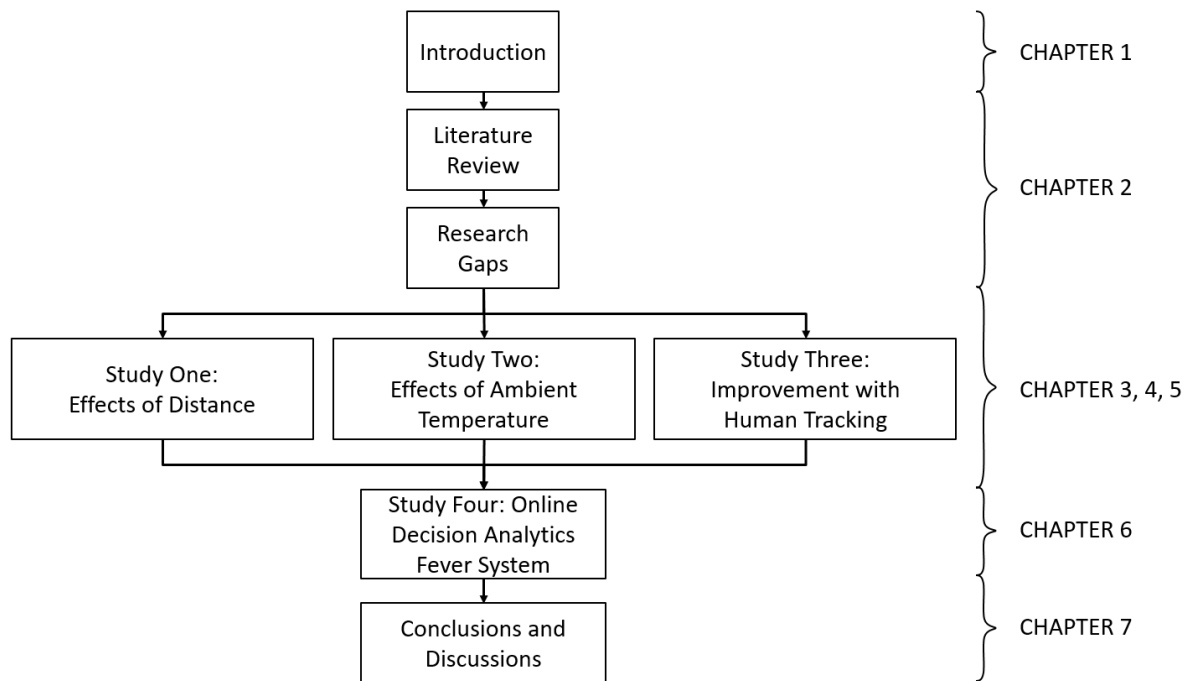


Figure 1-1: Thesis structure.

Another Way to Visualize My Research

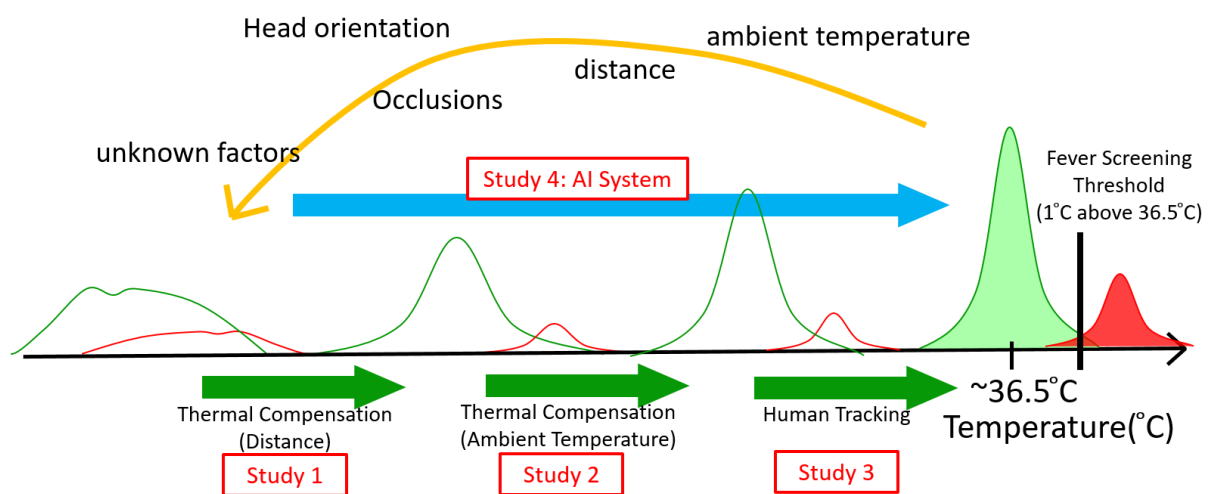


Figure 1-2: An overview of the thesis research.

Chapter 2 LITERATURE REVIEW

Summary

This chapter critically reviews the literature on principles of temperature measurement with infrared thermograph, non-invasive fever screening application, algorithms on human detection, face detection, object tracking, and person re-identification. The chapter ends with a summary of research gaps.

2.1 Principles of Infrared Thermography (IRT) and Temperature Measurement

With surface temperature higher than absolute zero, objects emit electromagnetic radiation [4], and the infrared dissipation is more prominent when the object's surface temperature is higher in general. The fraction of radiant emittance from infrared dissipation can be characterized with three parameters[5] at any wavelength, which are the spectral absorption(α_λ), spectral transmission (τ_λ) and spectral reflection (ρ_λ), the equation can be written as follows:

$$\alpha_\lambda + \tau_\lambda + \rho_\lambda = 1 \quad (1)$$

With opaque materials, the fraction of radiant emittance is either absorbed or reflected. Therefore, equation 19 can be simplified as follows:

$$\alpha_\lambda = 1 - \rho_\lambda \quad (2)$$

A *blackbody* is defined as a physical body that absorbs all incident radiant emittance that falls onto it regardless of the angle of incidence or frequency of the electromagnetic radiation. According to Stefan-Boltzmann law, the radiation intensity (M) of a blackbody can be obtained using the following equation:

$$M_b = \sigma * T^4 \quad (3)$$

where σ is Stefan – Boltzmann constant $= 5.67 * 10^{-8} Wm^{-2}K^{-4}$

T is the object temperature

However, objects do not behave like blackbody in reality, and the *emissivity* of an object is defined as the ratio of the radiant emittance of the object and the radiant emittance of a blackbody at the same temperature. Hence, the emissivity of an object at a specific wavelength can be expressed as follows:

$$\varepsilon_\lambda = \frac{M_\lambda}{M_{\lambda b}} \quad (4)$$

In reality, the emissivity of an object varies, and it is wavelength-dependent. Nevertheless, the emissivity of a solid object is slow-varying within short-wavelength intervals and is often assumed to be a constant in infrared thermography (IRT). So then, the emissivity of an object is represented as ε , where $0 \leq \varepsilon \leq 1$, $\varepsilon=0$ is considered as a perfect thermal mirror, and $\varepsilon=1$ is considered as a blackbody.

From Equation (4), we can obtain the radiation intensity of a solid object by the following equation:

$$M = \varepsilon * \sigma * T^4 \quad (5)$$

For temperature measurement using IRT, a general model of radiation received by the infrared camera is illustrated in Figure 2-1.

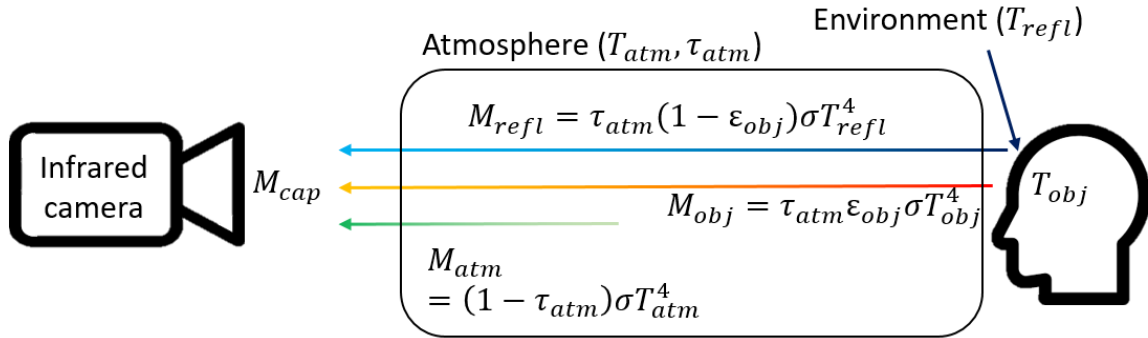


Figure 2-1: A General Model of Radiation for Temperature Measurement

When measuring a solid object with an infrared camera, the total radiant emittance (M_{cap}) captured at the infrared camera is a sum of three sources. They are the radiant emittance of the object (M_{obj}), the surrounding reflected by the object (M_{refl}), and the atmosphere (M_{atm}). It can be expressed in the equation below:

$$M_{cap} = M_{obj} + M_{refl} + M_{atm} \quad (6)$$

From Figure 2-1, M_{obj} and M_{refl} will be transmitted through the atmosphere. The transmittance of the atmosphere (τ_{atm}) describes the efficiency of the radiant emittance being

transmitted through the atmosphere. Then, the emissivity of the atmosphere is $(1 - \tau_{atm})$. Equation (6) can be rewritten as follows:

$$M_{cap} = \tau_{atm}(\varepsilon_{obj}\sigma T_{obj}^4 + (1 - \varepsilon_{obj})\sigma T_{refl}^4) + (1 - \tau_{atm})(\sigma T_{atm}^4) \quad (7)$$

2.2 Temperature Screening

The effectiveness of IRT in fever screening with different thermal imagers was studied with over 1,000 subjects under different ambient temperatures and distances between subjects and the cameras[1]. The study suggested that the temperature readings captured by thermal infrared cameras could measure core body temperatures. This finding is consistent with another study conducted to examine the effectiveness of thermal imagers for the mass screening of fever subjects such as SARS patients [2]. However, the effects of distance are not well-controlled as the data of different distances were collected on different days. Another clinical study [6] agrees to use IRT for fever screening with the canthi temperature and suggests that full-face maximum temperature may be another choice. Another study in Nagoya Airport reported that IRT has good accuracy in detecting febrile subjects, and the accuracy was further improved with self-reporting questionnaires [7]. Together, these four studies indicate that thermal infrared imagers are a promising tool for mass fever screening. However, the systems used in those studies require manual identification of fever suspects by skilled human operators. Indeed, similar procedures are being used daily at border control points. These procedures can result in human errors and can be stressful for the operators. A more recent study, Shaikofci shows that outdoor ambient temperature and human forehead temperature are significantly correlated [8]. However, they did not address the joint effects of distance and ambient temperature at a more extended range. The reason is due to the short operating range of the thermopiles system used in their study.

2.3 Human and Face Detection

In recent years, object detection algorithms have matured. Earlier object detection algorithms include classic object detection methods in computer vision using features such as Haar-like filters with motion cues[9] and the histograms of oriented gradients + support vector machine (HOG+SVM) classifier[10]. The renaissance of better deep learning methods began with the likes of fast region-based convolutional neural networks (R-CNNs)[11], the single shot multibox detector (SSD), and You Only Look Once (YOLO)[12]–[14]. In general, one-stage detectors like SSD and YOLO trade accuracy for speed, while two-stage detectors like R-CNNs

achieve higher accuracy but are much slower. Subsequently, the region proposal network (RPN) was proposed in [12] to speed up the fast R-CNNs to almost real-time. In addition, RetinaNet trained with focal loss, proposed in [15], can enhance the accuracy of one-stage detectors to a level comparable to the state-of-the-art benchmarks set by two-stage detectors. These object detectors are great options for human detection, face detection, or both. In particular, the faster one-stage detectors are more suitable for real-time applications.

Nonetheless, human pose estimation (HPE) algorithms can also be applied in human detection. The concept of part-based modeling for facial structure estimation was introduced by Fischler and Elschlager in 1973 [16]. It is known as pictorial structures for human pose estimation. The algorithm mainly consists of two modules: the first consists of recognizing different parts in the image, and the second forms a structure with the recognized parts. Dalal et al. proposed histograms of oriented gradients (HOG) for human detection in 2005 [10]. The application of HOG descriptors as features to detect human or human joints has gained much traction in this field. Yang et al. [17] proposed using flexible mixtures-of-parts to break down the human parts into even smaller parts. This approach has increased the flexibility and accuracy of articulated pose estimation. These crucial works lay the foundation of modern-day human pose estimation algorithms.

The use of the two-module approach and flexible mixtures-of-parts has not been changed much even after introducing deep learning approaches. Alexander Toshev and Christian Szegedy proposed DeepPose and brought deep learning techniques into human pose estimation in 2014 [18]. It achieved state-of-the-art performance in two popular datasets for human pose estimation: (1) Leeds Sports Pose (LSP) [19] and its extension [20], and (2) Frames Labeled In Cinema (FLIC) [21]. Since the introduction of DeepPose, deep learning approaches have dominated HPE in terms of performance. These deep learning approaches can be summarized into two primary categories: the top-down and bottom-up approaches. Top-down approaches [22]–[24] require a separate human detector to localize the humans in the image and perform key points estimation on each of the humans. These methods are usually state-of-the-art in terms of accuracy, as the image of the humans can be scaled to the same size for key points of human joints detection. However, these methods are often more computationally intensive and are affected by the number of persons in the images. On the other hand, the bottom-up approaches [25]–[31] first identify the different human joints

independently, then incorporate them to form the humans. This approach needs to deal with scale variation problems, often having difficulties in identifying relatively small human forms in the images. In contrast to the top-down methods, the run time of the bottom-up approaches is shorter, and is not affected by the number of people in the images.

2.4 Object Tracking

Object tracking has been one of the popular topics in the computer vision community for years. It is often modelled as a data association problem to correlate the same person in the current frame and the previous frames. Before 2015, many sophisticated methods were proposed to solve this data association problem. There are six main types of major approaches: appearance model, motion model, interaction model, exclusion model, occlusion handling, and inference approach [32]. These sophisticated methods mainly tried to overcome the deficiency of subject detection, especially when subjects were occluded. Since 2015, deep learning approaches for object detection became popular and dominated all other approaches. The tracking-by-detection framework has regained popularity in object tracking tasks in recent years. Quick and straightforward tracking algorithm [33] only using location cues can outperform those conventional sophisticated algorithms before 2015.

In recent years, appearance and affinity-based approaches have been dominating the field. However, there is a trade-off between speed and accuracy. SORT, which utilizes a simple deep appearance descriptor to associate the same person across frames, is lightweight and fast [34]. TrackR-CNN extends Mask R-CNN to provide accurate tracking features by learning association head, but the method is too slow for real-time application [35]. Joint Detection and Embedding (JDE) is another method utilizing CNN to extract the subject's appearance and affinity [36]. It balances speed and accuracy effectively.

This thesis focuses on the multiple object tracking (MOT) problem as we are tracking multiple persons in the scene in real-time. Since we already have the detection results from the human detector, the quick and straightforward location-based algorithm is the best option to balance the speed and accuracy. Custom modifications were made to suit our applications.

2.5 Person Re-identification (ReID)

Person re-identification (ReID) associates images of the same person taken from different angles and cameras. The research on this task started with tracking the same person across

multiple cameras [37]. There are mainly two kinds of ReID approaches: image-based and video-based. Image-based algorithms examine and match image pairs independently, whereas video-based algorithms use the spatial-temporal information of having few images consequently from slightly different angles over time. [38], [39] are the representative works from video-based approaches that show accumulated frames for the same person effectively improves the performance of ReID compare with algorithms based on a single image. However, the performance saturates as the number of frames given increases [39].

On the other hand, there have been more studies on image-based algorithms. Before the penetration of deep learning approaches in the ReID task, algorithms mainly utilized hand-crafted features or image descriptors for ReID. Gary et al. proposed the use of AdaBoost to extract important features in 8 color channels (RGB, HS, YCbCr) and image descriptors generated by 21 texture filters (rotationally symmetric Schmid filters, horizontal and vertical Gabor filters) [40]. More works [41]–[45] utilize similar features and formulate optimization problems to solve the ReID problem. With deep learning started gaining traction in 2012, [46], [47] brings deep learning techniques to ReID. In recent years, [48] achieved state-of-the-art accuracy on Market-1501 [49], a popular high-quality dataset for ReID. In this thesis, a modification was made on the baseline method [50] according to the needs of this study.

2.6 Research Gaps

Based on the literature review, it was observed that long-distance non-invasive temperature screening with deep learning technologies had received little attention. On the other hand, studies showed that thermal imaging technologies for temperature screening are promising. However, the effects of different factors on non-invasive temperature measurement and screening have not been carefully studied. The research gaps identified from the literature review are summarized as follows:

Gap1: The effects of distance on non-invasive human temperature measurement and screening at long-range have received less attention.

Gap2: There are fewer studies on the effects of ambient temperature on non-invasive temperature measurement and screening, especially at long range.

Gap3: There is no study on noise suppression with human subject tracking on non-invasive temperature measurement.

Gap4: There is no large-scale mass fever screening system integrated with multiple deep learning technologies that can track fever suspects over multiple cameras.

Chapter 3 STUDY ONE: EFFECTS OF DISTANCE ON NON-INVASIVE TEMPERATURE SCREENING

Summary

Due to the absorption of infrared wave energy by the atmosphere, the non-invasive temperature measurement of the same subject at a smaller distance from the thermal camera is different from the measurement at a larger distance. This chapter reports the details and findings of study one. Study one was designed to examine the effects of distance from the thermal camera in taking on non-invasive temperature measurements within the scope of fever screening. In addition to the empirical investigation, details on a thermal compensation model developed to optimize the measurement of forehead temperature are also presented. Results of a sensitivity analysis on the thermal compensation model are also reported.

3.1 Introduction

Non-invasive temperature measurement is intrinsically complex and can be affected by many factors. One of the decisive factors is the distance between the thermal camera and the subject. An experiment was designed to study the effects of sensor-subject distance on non-invasive temperature measurement and temperature screening for both ordinary and fever persons.

3.2 Hypothesis

3.2.1 Due to the absorption of infrared wavelengths by the atmosphere, the non-invasive temperature measurement decreases with increasing distance between the thermal camera and the subject.

3.2.2 Fever screening range increases as a result of the thermal compensation for the temperature loss due to distance.

3.3 Method

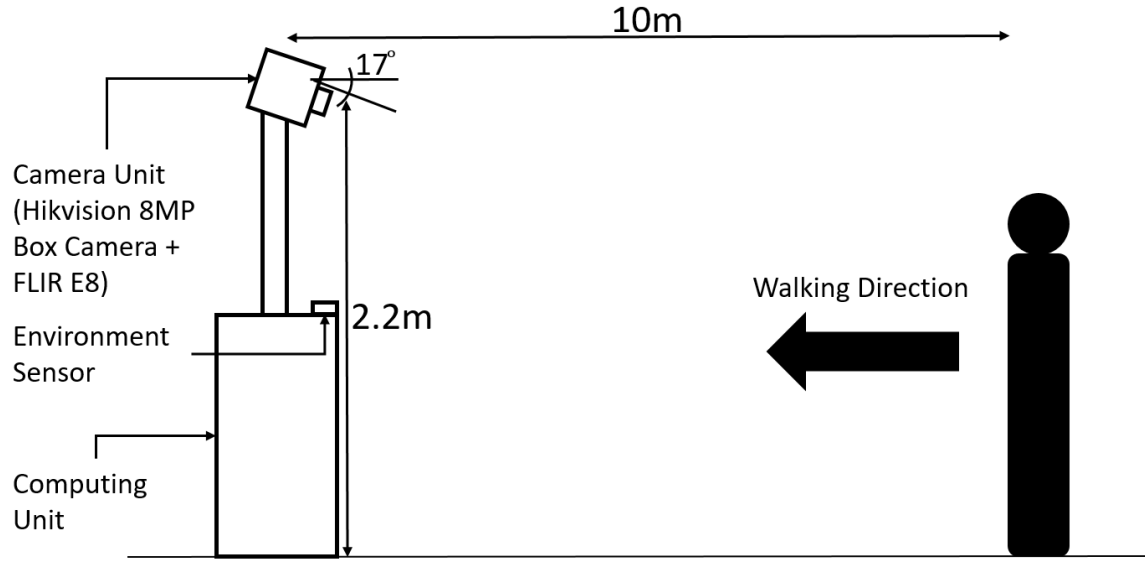


Figure 3-1: An experiment setup using our Remote Fever Screening System (RFSS). Temperature measurements were recorded throughout the whole experiment.

The experiment was set up using our developed Remote Fever Screening System (RFSS). The RFSS [Appendix 3.1, page 104] consists of a camera unit, an environmental sensor, and a computing unit (Intel Core i9 and NVIDIA RTX 2080 Super). The camera unit consisted of a Hikvision 8MP Box Camera and a FLIR E8-XT thermal camera and was placed at a height of 2.2m with a tilting angle of 17 degrees below the horizontal. The color images were spatially registered to the thermal images using the homography transformation described in [51] to ensure image alignment. Figure 3-2 shows the photo of our experiment setup using RFSS.

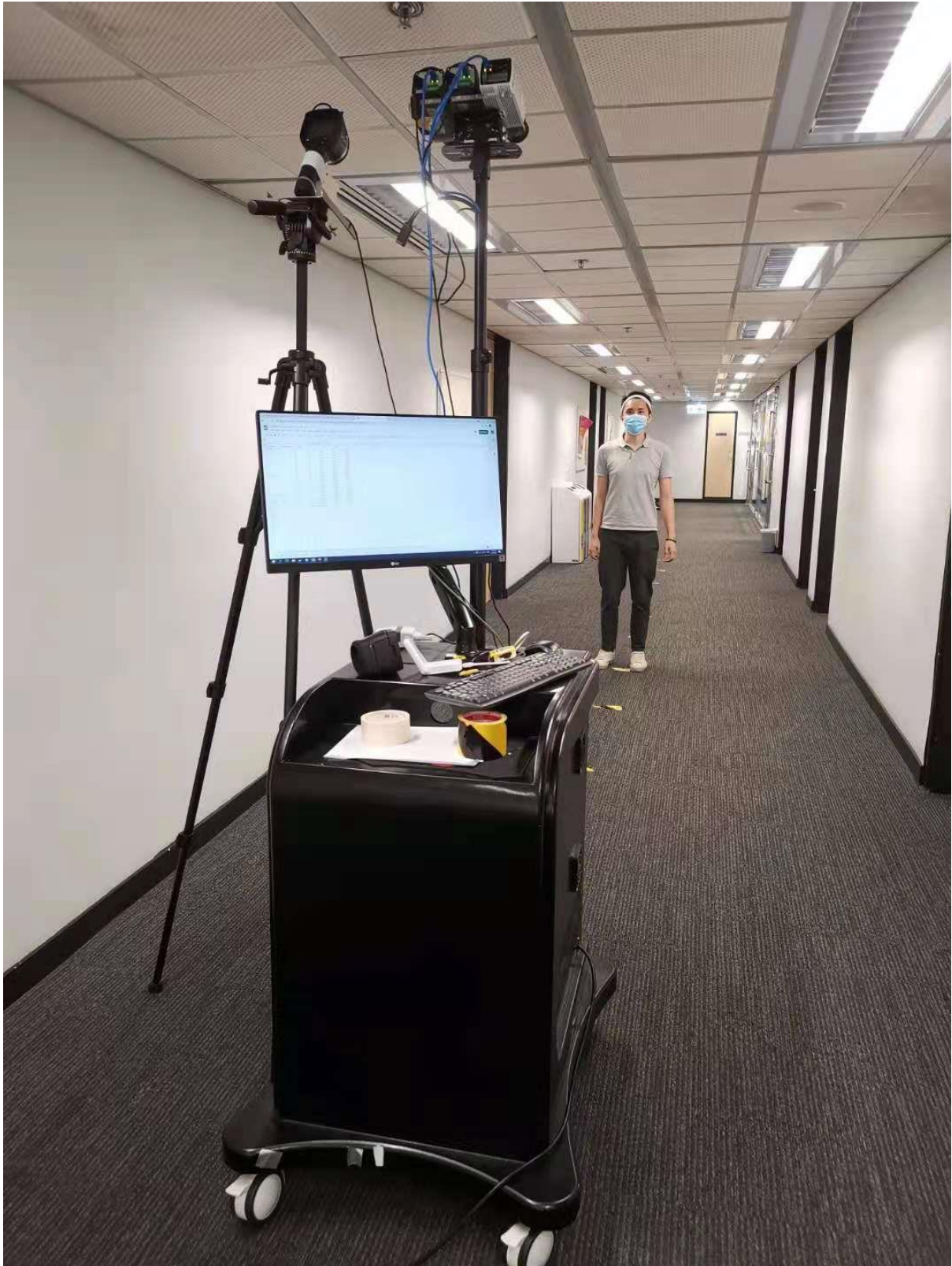


Figure 3-2: A photo of the experiment setup using Remote Fever Screening System (RFSS).

3.3.1 Variables

Our goal is to understand the effects of distance and different fever statuses on the temperature measurement of the subject and the ability to separate the two groups of people (normal and febrile).

Variables were summarized in Table 1.

Independent Variable	
Name	Type
Distance	Continuous
Fever Status	Categorical
Dependent Variable	
Name	Type
Temperature Measurement	Continuous
Sensitivity and Specificity	Continuous

Table 1: A list of variables in study one

3.3.2 Experimental Setup and Protocol

The experiment was conducted with eight healthy subjects (five males and three females) in a controlled indoor environment. An overview of the experimental setup is illustrated in Figure 3-1. Each subject stood front facing the RFSS at nine different distances (2m-10m in 1m increments). The subject's forehead temperature was measured and recorded with the system at each distance, and three times with a handheld thermometer (HuBDIC Non-Contact Infrared Thermometer FS [Appendix 3.2, page 108]). The raw thermal data stream with the resolution of 320x240 at ten frames per second was recorded in the system. This process was conducted once with the subject's natural forehead temperature, and again with their heated forehead temperature. A hot pack was placed [Appendix 3.3, page 108] on the subject's forehead for ten seconds before the temperature measurement to simulate the heated forehead temperature.

The range of forehead temperatures of normal persons measured with the handheld thermometer is between 36.2°C and 36.7°C, with a mean of 36.5°C. The range of simulated elevated temperatures is between 38°C and 39.7°C, with a mean of 38.6°C. In addition, the mean ambient temperature throughout the experiment was 23.46°C with an S.D. of 0.05°C, and the mean humidity was 77.62% with an S.D. of 0.25%, as shown in the figure below:

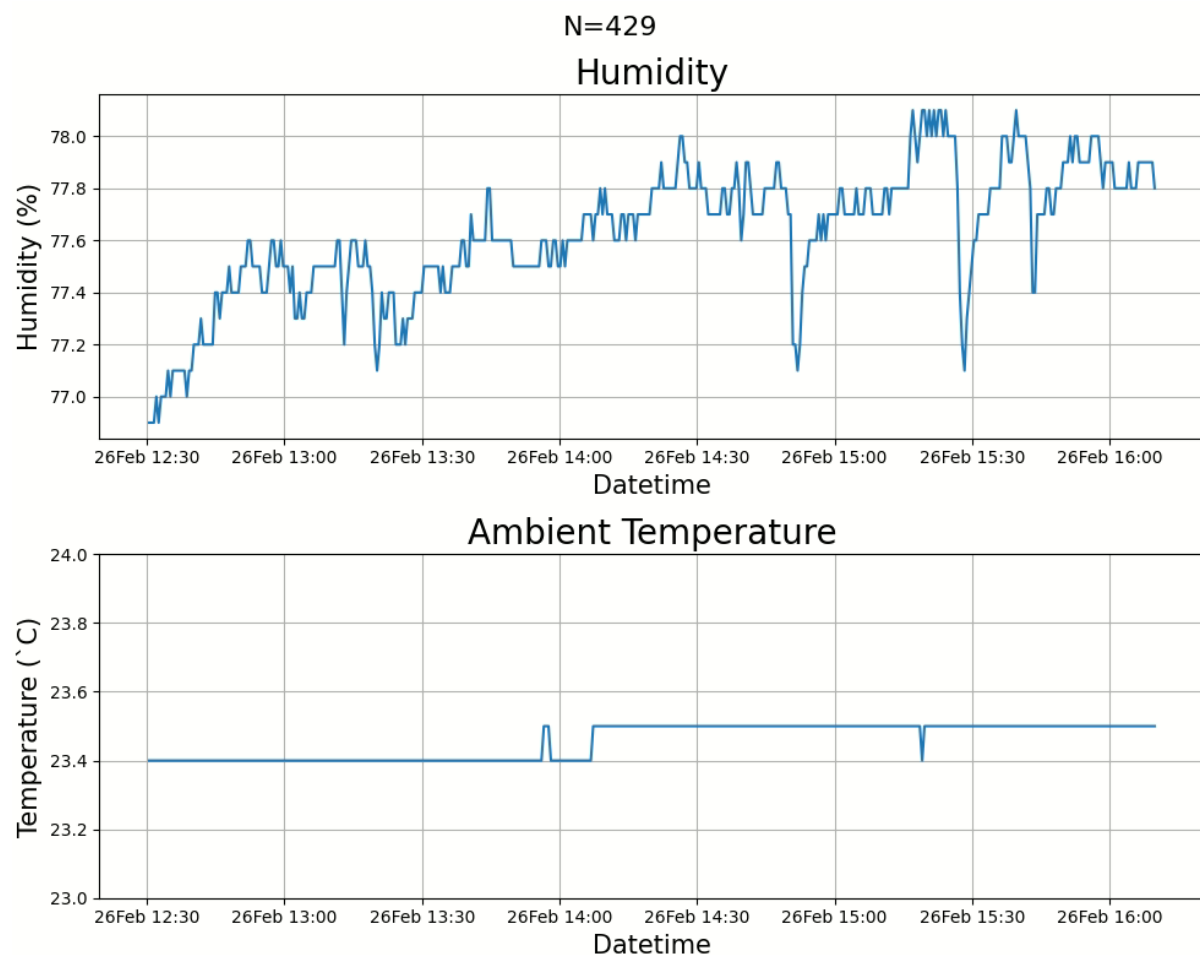


Figure 3-3: The ambient temperature and humidity recorded during the experiment. The mean ambient temperature was 23.46°C and the mean humidity was 77.62%.

3.4 Results and Analysis

The results show the effects of distance in non-invasive temperature measurements. In addition, a thermal compensation model was developed to compensate for the loss due to the effects of distance and increase the distance for high accuracy fever screening. Last, the code for analysis is in [Appendix 3.4, page 108] sensitivity analysis on the thermal compensation model was done at the end of the section.

3.4.1 Effects of Distance on Temperature Measurements

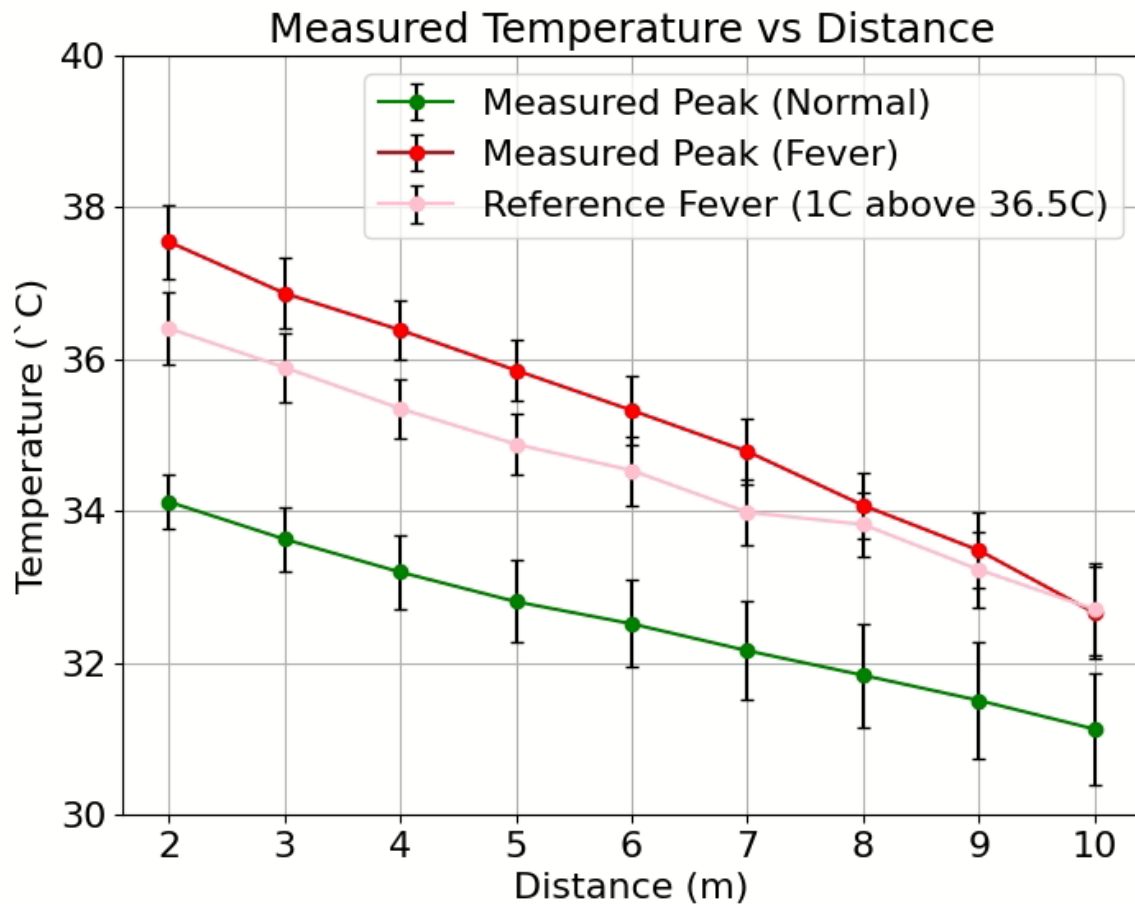


Figure 3-4: Temperature Measurements using a FLIR E8. Data shows that the temperature drops linearly when the sensor-subject distance increases.

Figure 3-4 shows the temperature measurements using FLIR E8 in our system and HuBDIC Non-Contact Infrared Thermometer FS-300 as the reference temperature of the subjects. The green, red and pink lines indicate the forehead temperature measurement of the normal group, fever group, and reference fever group, respectively. Since we have the measured temperature of the normal and fever group, they are extrapolated to obtain the temperature values of the reference fever group. At each distance, we multiplied a scaling factor to the measured temperature of the fever group. The lowest and highest temperature of the reference fever group was 37.5°C (1°C elevation from green) and 38.9°C, respectively. The extrapolated temperature is defined as the “measured temperature by the thermal infrared camera” of the reference fever group, and it will be used for the consequent studies. The temperature distributions of the normal and reference fever group are shown in Figure 3-5. ANOVA has been conducted on the collected data. The result shows that increasing distance

reduces non-invasive temperature measurements significantly [Normal: $F(1, 214) > 524$, $P < 0.001$; Reference Fever: $F(1, 209) = 1231.97$, $P < 0.001$] in a linear fashion [|Pearson correlation| $> .8$, $P < 0.001$].

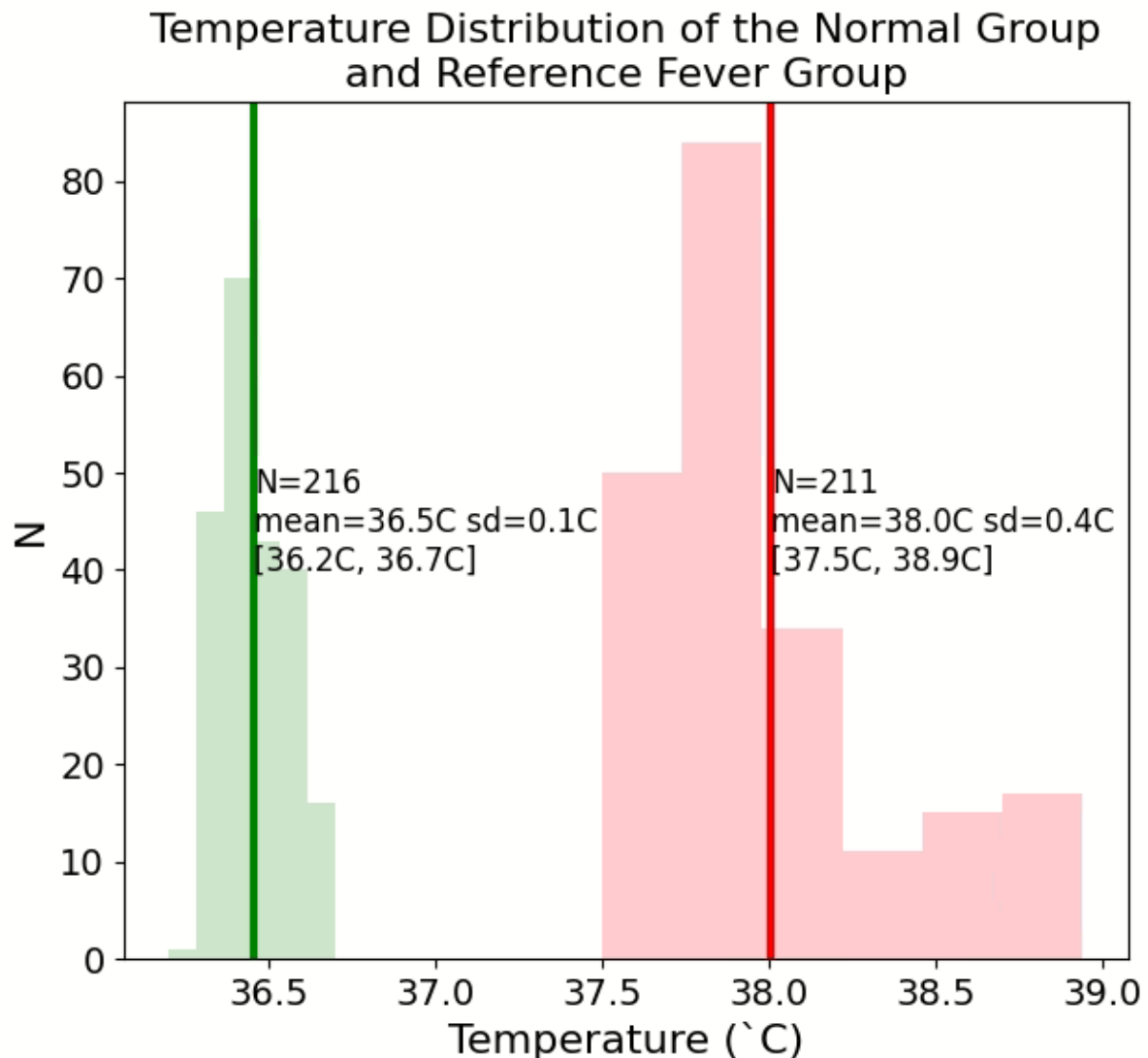


Figure 3-5: Temperature Distribution of the Normal and Reference Fever Group.

Figure 3-6 shows that the temperature measurements measured using two different thermal cameras: (a) a FLIR E8 and (b) a FLIR A315. Results show that our finding is consistent across different thermal cameras [Appendix 3.5, page 109], but we see different slopes in the curves with different cameras. FLIR A315 is a more expensive thermal camera, and we see a smaller measured temperature loss compare over the distance than the cheaper FLIR E8.

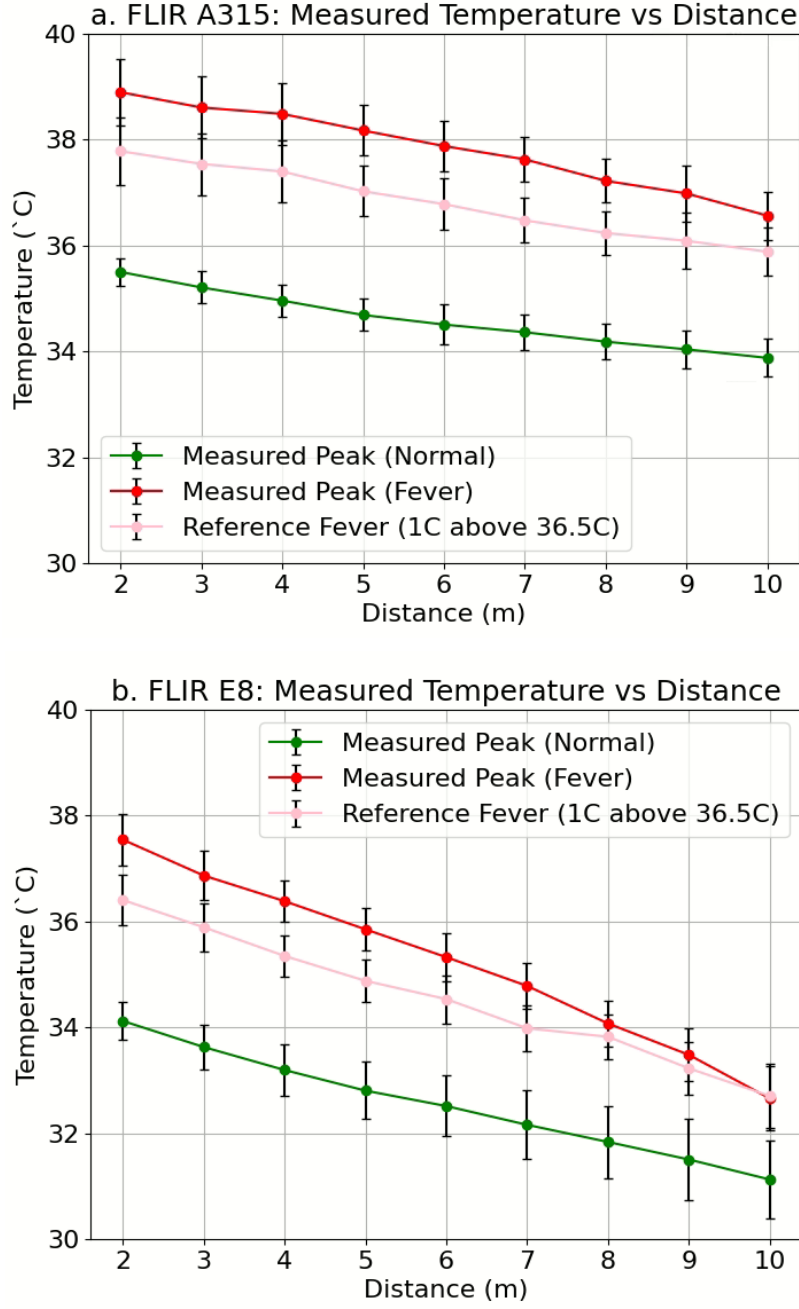


Figure 3-6: (a) Temperature measurements measured using a FLIR E8. (b) Temperature measurements measured using a FLIR A315.

3.4.2 Model for Thermal Compensation on the Effects of Distance

Knowing the loss in temperature measurement due to distance from Figure 3-4, we can derive a thermal compensation statistical model. Since the quadratic and cubic terms of the distance are not significant [Appendix 3.5, page 109], the statistical model only consists of the linear term of the distance. The compensated temperature (T'_{obj}) can be expressed as follows:

$$T'_{obj} = a_0d + a_1 + T_0 \quad (8)$$

Where a_0 is the estimated coefficient related to distance, such as loss due to image resolution decrease over distance and loss due to atmospheric absorption, a_1 is the estimated coefficient for the other uncontrolled factors like potential calibration error from the thermal camera. Finally, T_0 is the temperature measurement readings provided by the thermal infrared camera.

There is a general model of radiation for temperature measurement (equation (7)). Therefore, part of the statistical model can be expressed using the physics model from the general radiation model for temperature measurement.

Let M_0 be the total radiant emittance measured at the infrared camera, ϵ_{obj} to be $\epsilon_{obj(set)}$ which typically be 0.98 for fever screening application, T_{refl} to be $T_{refl(set)}$ with the default setting in the thermal infrared camera to be 20°C. T_0 is the temperature measurement readings provided by the thermal infrared camera, and assume $\tau_{atm}=1$. Then, we have:

$$M_0 = \epsilon_{obj(set)}\sigma T_0^4 + (1 - \epsilon_{obj(set)})\sigma T_{refl(set)}^4 \quad (9)$$

From equation (6), the estimated radiant emittance from the object (\hat{M}_{obj}) can be calculated as follows:

$$\hat{M}_{obj} = M_0 - \hat{M}_{refl} - \hat{M}_{atm} \quad (10)$$

Where \hat{M}_{refl} is the estimated reflected radiant emittance, and \hat{M}_{atm} is the estimated radiant emittance from the atmosphere.

Then, estimated temperature (\hat{T}_{obj}) can be calculated as follows:

$$\hat{T}_{obj} = \sqrt[4]{\frac{M_0 - \hat{M}_{refl} - \hat{M}_{atm}}{\hat{\tau}_{atm}\epsilon_{obj}\sigma}} \quad (11)$$

According to [52], the ϵ_{obj} of human forehead is 0.969.

\hat{M}_{refl} is the estimated radiant emittance reflected from the environment which can be modeled as follows:

$$\hat{M}_{refl} = \hat{\tau}_{atm}(1 - \epsilon_{obj})\sigma(\hat{T}_{atm} + a_2)^4 \quad (12)$$

where a_2 is the estimated offset from the background considering that the system might be installed in different environments.

\hat{M}_{atm} is also estimated by the environment sensor and can be expressed as follows:

$$\hat{M}_{atm} = (1 - \hat{\tau}_{atm})\sigma\hat{T}_{atm}^4 \quad (13)$$

where $\hat{\tau}_{atm}$ is the atmospheric transmittance estimated from the sensor-subject distance, according to [53], it can be modeled as the following form:

$$\hat{\tau}_{atm} = e^{-a_3(\sqrt{d}-\sqrt{d_{cal}})-a_4(d-d_{cal})} \quad (14)$$

Where a_3 and a_4 are the estimated coefficients affected by the environment atmosphere, d is the distance between the subject and the infrared camera, d_{cal} is the calibration distance (assumed to be 0).

Finally, we have the compensated temperature (T'_{obj}) as follows:

$$T'_{obj} = a_0d + a_1 + \hat{T}_{obj} \quad (15)$$

$$T'_{obj} = \overbrace{a_0d + a_1}^{\text{statistical model}} + \overbrace{\sqrt[4]{\frac{M_0 - \hat{M}_{refl} - \hat{M}_{atm}}{\hat{\tau}_{atm}\epsilon_{obj}\sigma}}}^{\text{physics model}} \quad (16)$$

The data of the normal group in Figure 3-4 was used to train and test our compensation model. The 216 data points were divided into the training data and testing data randomly, with 90% of them were training data and 10% of them are testing data. Furthermore, the reference fever data (pink) is also counted as the testing data. Based on [54], a linear model optimization program was developed to find the optimal solution for all the coefficients (from a_1 to a_4). The loss function is defined as the root-mean-square-error between compensated temperature (T'_{obj}) and reference temperature. A global optimization technique (Basin-hopping algorithm by David J. Wales and Jonathan Doye with 'L-BFGS-B' method implemented by [55]) is utilized to find the optimal solution for the coefficients that can minimize the error between T'_{obj} and the reference temperature.

The Pearson correlation coefficient, mean absolute error (MAE), and root-mean-square error (RMSE) are utilized to compare the measured temperature from the thermal camera and compensated temperature from the system against the reference temperature using the handheld thermometer. The MAE and RMSE between the compensated temperature from the system and the reference temperature measured using the handheld thermometer

reduce significantly. The MAE and RMSE of the compensated temperature on the training data reduce from 3.908°C and 4.057°C to 0.426°C and 0.513°C, respectively. Similarly, we see a significant reduction in the MAE and RMSE on the testing data, as illustrated in Table 2. The significant error reduction can also be seen in Figure 3-7.

	Pearson Correlation	MAE(°C)	RMSE(°C)
Training data only with the normal group (N=194)			
Measured Temperature	0.4106	3.908	4.057
Compensated Temperature	0.8550	0.426	0.513
Testing data only with the normal group (N=22)			
Measured Temperature	0.5278	3.629	3.749
Compensated Temperature	0.8315	0.338	0.409
Testing data only with the fever group (N=211)			
Measured Temperature	0.3848	3.438	3.630
Compensated Temperature	0.5873	0.525	0.618

Table 2: The Pearson Correlation, Mean Absolute Error and Root Mean Square Error comparison between the Measured Temperature and Compensated Temperature vs the Reference Temperature

Since our thermal compensation model is trained with the normal group only, there is an overestimation for the reference fever group, and this might cause some false alarms. However, this is a minor issue for temperature screening because having false alarms is better than having missing suspects in practice.

Figure 3-8 shows the temperature distribution of the normal group and reference fever group with and without the thermal compensation at all distances. The area of overlap between two distributions decreases with our thermal compensation. The result suggests that the thermal compensation model improves the theoretical upper bound to separate the normal and febrile groups.

Measured Temperature vs Distance

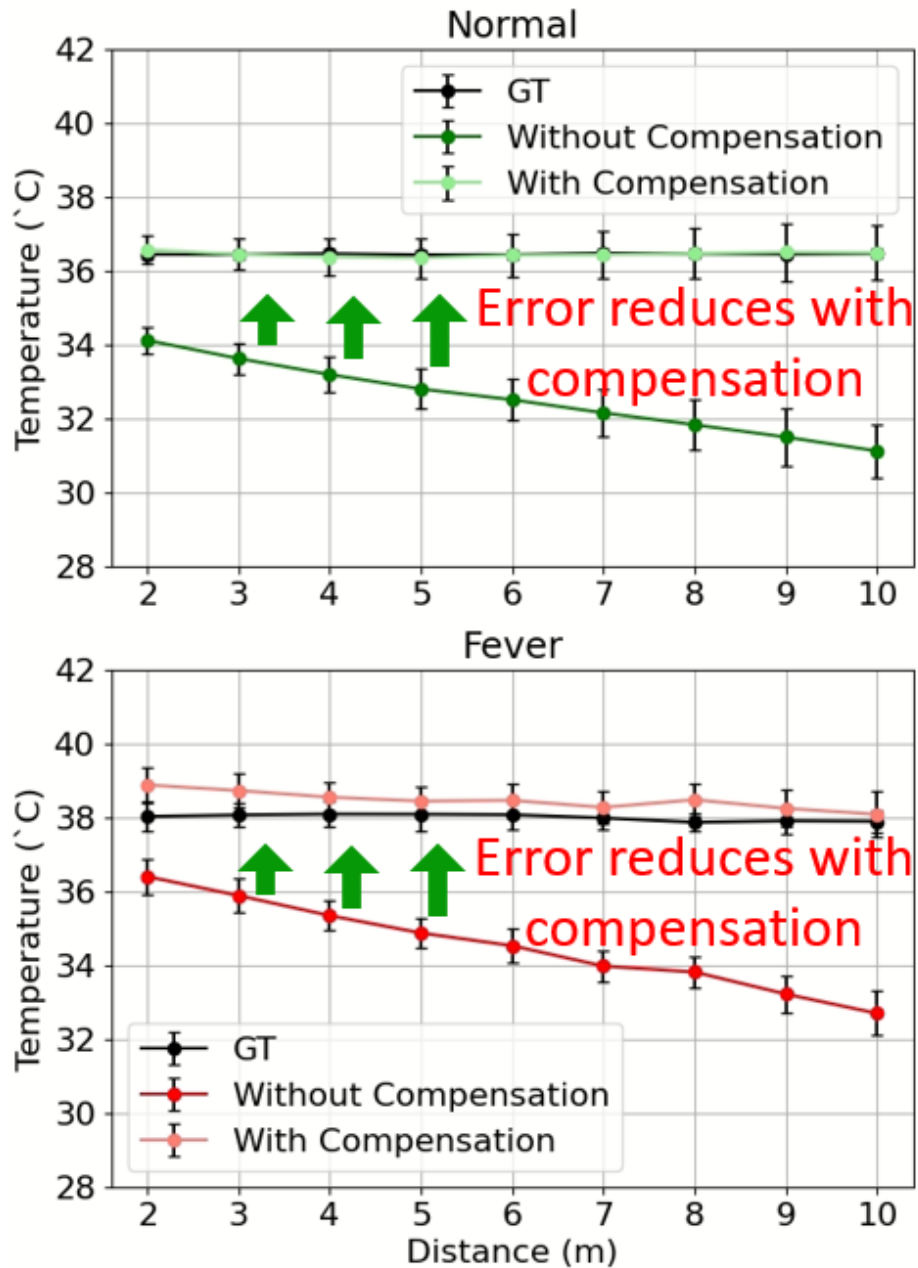


Figure 3-7: The error reduces with our thermal compensation.

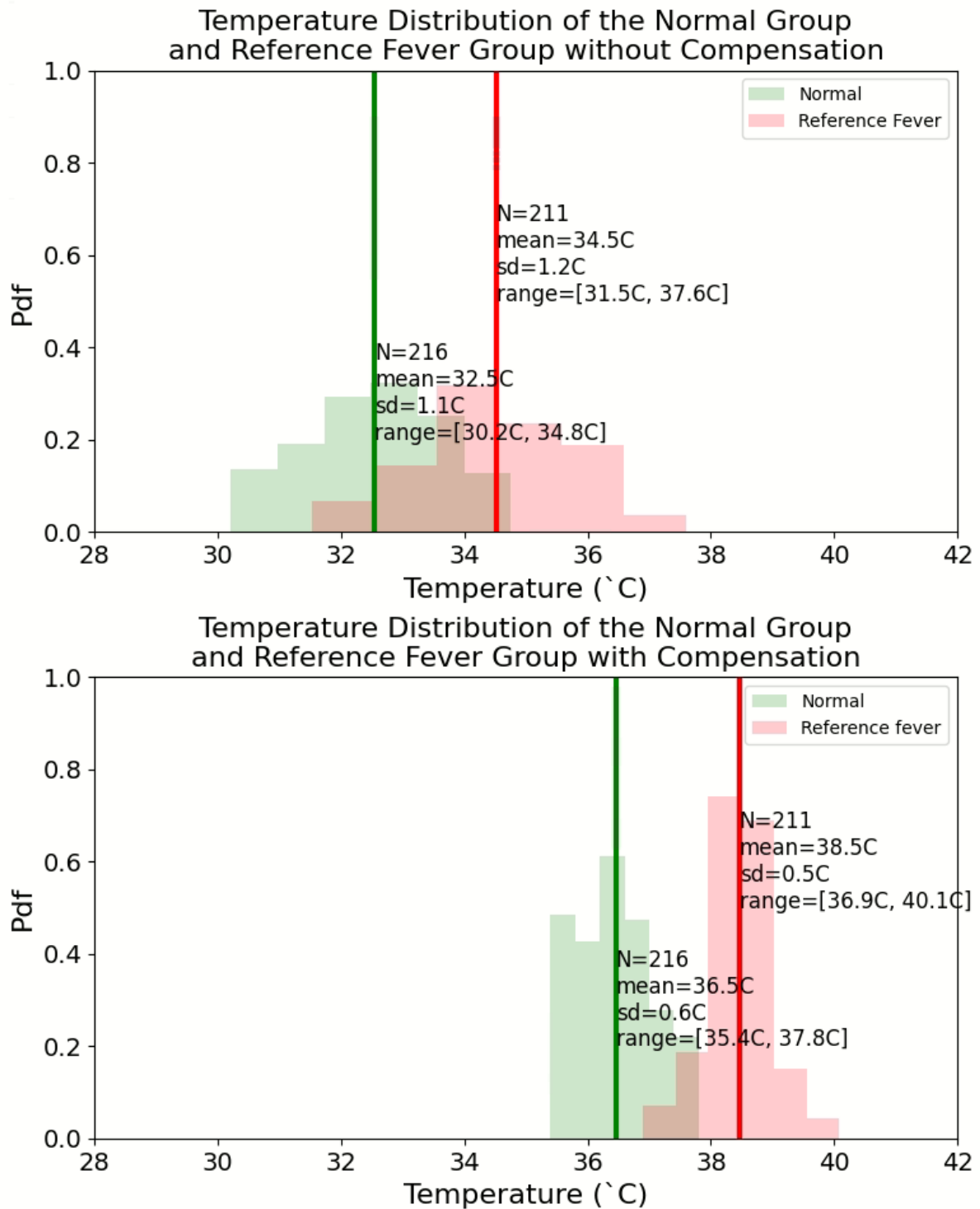


Figure 3-8: Temperature distribution of the normal group and reference fever group with and without thermal compensation.

3.4.3 Sensitivity and Specificity of Fever Screening at Different Distances with and without Thermal Compensation

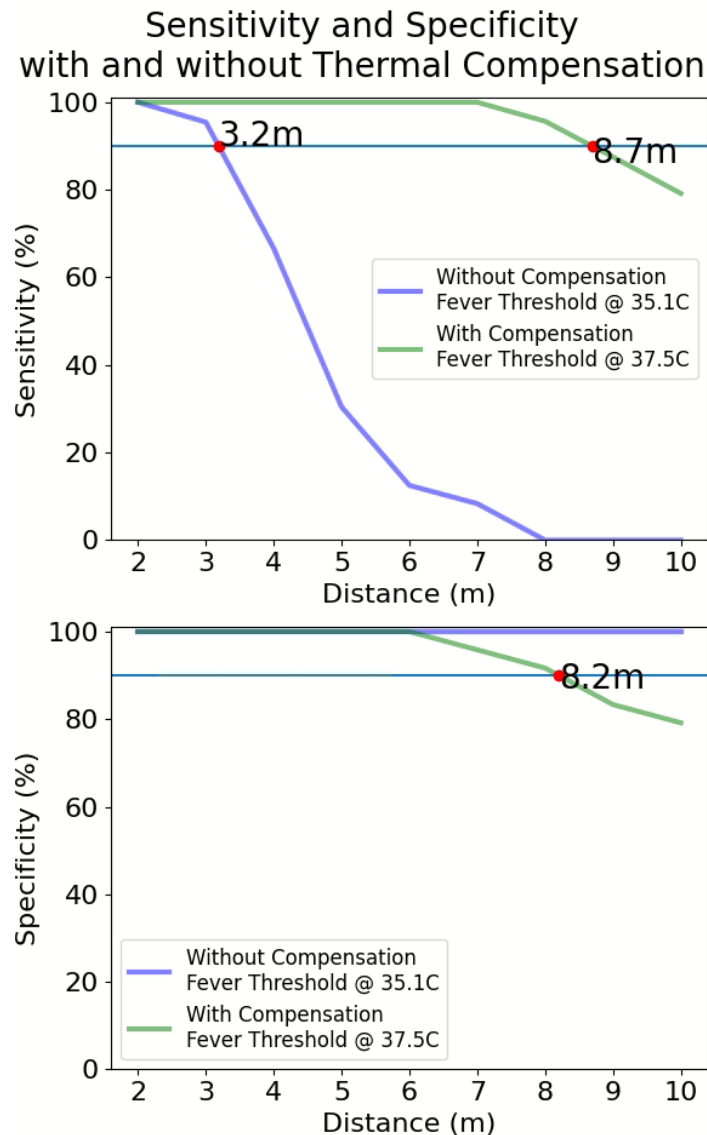


Figure 3-9: Sensitivity and specificity of fever screening with and without thermal compensation.

Figure 3-9 shows the sensitivity and specificity of fever screening with and without our thermal compensation. Sensitivity is the true positive amongst the total positive samples, and specificity is the actual negative amongst the total negative samples. Thus, high sensitivity and high specificity are desired in the fever screening system. Fever thresholds of 35.1°C (1°C above the mean of normal group at 2m) and 37.5°C (1°C above 36.5°C) were used as the alarm thresholds to separate the normal and fever groups, with and without compensation, respectively. The results show that the distance for temperature screening with $\geq 90\%$

sensitivity and $\geq 90\%$ specificity is up to 3.2m without compensation. Additionally, the distance for temperature screening is extended to 8.2m with our proposed model and compensation. Based on the application requirements for sensitivity and specificity, the distance for accurate temperature screening can be determined.

3.5 Discussion and Conclusion

This chapter studies the effects of distance on non-invasive temperature measurement and temperature screening. We proposed a baseline thermal compensation model that confronts the effects of distance to improve the accuracy and robustness of non-invasive temperature measurement and screening. It increased the temperature measurement accuracy and extended the effective range for accurate temperature screening to longer distances.

The forehead temperature of the subjects by the thermal infrared camera is being underestimated without the thermal compensation. The error between the temperature measurement by the thermal infrared camera against the temperature measurement by the handheld thermometer increases when the sensor-subject distance increases. The mean absolute error (MAE) and the root-mean-square error (RMSE) can be as large as 3.707°C and 3.875°C . Regardless of the errors in temperature measurements, separating the normal and febrile groups of people with a lower alarm threshold is possible. However, the temperature screening is limited to a short range of distances up to 3.2m with this approach.

With our proposed model and compensation, the MAE and RMSE were reduced to 0.474°C and 0.567°C , respectively. The distance for temperature screening increased to 8.2m. The improvements in screening distance can effectively increase the efficiency of temperature screening.

The proposed method and its results show significant advancement in non-invasive temperature measurement and temperature screening technology. Nevertheless, it is still relatively simple. In reality, it is more complicated and can be affected by other factors. The following chapter will study the effects of the environment on the non-invasive temperature measurement.

Chapter 4 STUDY TWO: EFFECTS OF AMBIENT TEMPERATURE ON NON-INVASIVE TEMPERATURE SCREENING

Summary

Study two was conducted to examine the effects of ambient temperature on temperature measurements within the scope of fever screening. More than 14M data points were collected using our developed and deployed Remote Fever Screening System (RFSS) to facilitate study two. The steps and rationale of data cleaning and filtering are detailed. In addition to the empirical investigation, details of the second thermal compensation model developed to optimize the measurement of forehead temperature are also presented. Finally, a simulation is done to study the distance for temperature screening under different ambient temperatures and different distances.

4.1 Introduction

As mentioned in study one, the effects of distance cause measurement errors for non-invasive temperature measurement at various distances, and a thermal compensation model is proposed to compensate for it. Results suggested a promising direction for the proposed thermal compensation model, but it is relatively simple and only works in a controlled environment. Therefore, the focus of this study is on the effects of ambient temperature.

4.2 Method

4.2.1 Variables

Based upon the understanding of the effects of distance in study one, study two aims to expand the study to investigate the effects of ambient temperature on non-invasive temperature measurement and temperature screening.

Variables are summarized in Table 3.

Independent Variable	
Name	Type
Ambient Temperature	Continuous
Distance	Continuous
Dependent Variable	
Name	Type
Temperature Measurement	Continuous

Table 3: A list of variables in study two

4.2.2 Data Collection

Data collection was using our developed RFSS installed at the north gate (NG) on the HKUST campus. The RFSS consists of a camera unit, an environmental sensor, and a computing unit (Intel Core i9 and NVIDIA RTX 2080 Ti). The camera units of the RFSS consist of a Logitech BRIO color camera mounted 73mm below a FLIR E8-XT thermal camera and placed at the height of 2.2m with a tilting angle of 17 degrees below the horizontal. In the RFSS software, Open-Pose [31] was applied to obtain all human key points in the color image. Based on upper body key point information, the face box coordinates of each detected human were estimated [Appendix 4.1, page 110] and used to predict the sensor-subject distance. Next, the face box coordinates in the thermal image were calculated with the face box coordinates in the color image via homography transformation. Then, the temperature of the persons can be measured.

Furthermore, the version of RFSS software installed in the NG RFSS system is an upgraded version with a motion filter enabled [Appendix 4.2, page 110] on the thermal images to encounter the influences from the hot background (heated fixtures) that can cause false alarms in fever detection. The motion filter detects the pixels that are belonged to the fixtures and suppresses the effects from the hot background by deactivating them (turn them to 0 value). Data of the passersby were collected at roughly ten frames per second. The collected data includes the key point information, thermal information, fever status of the passersby

predicted by our system, ambient temperature, and the relative humidity of the environment. The data was collected from 27 September 2020 to 01 March 2021. Most importantly, there is no personally identifiable information (color photo of the faces) collected during the data collection period.

Due to the lack of a depth sensor being installed in the system, the sensor-subject distance is estimated using the diagonal length of the face box. Calibration data, which consists of the diagonal length of the face box and reference distance [Appendix 4.3, page 110], were collected at NG. Figure 4-1 shows the distance estimation using the reciprocal function with the calibration data. The distance estimation was being applied to the collected data at HKUST's NG entrance.

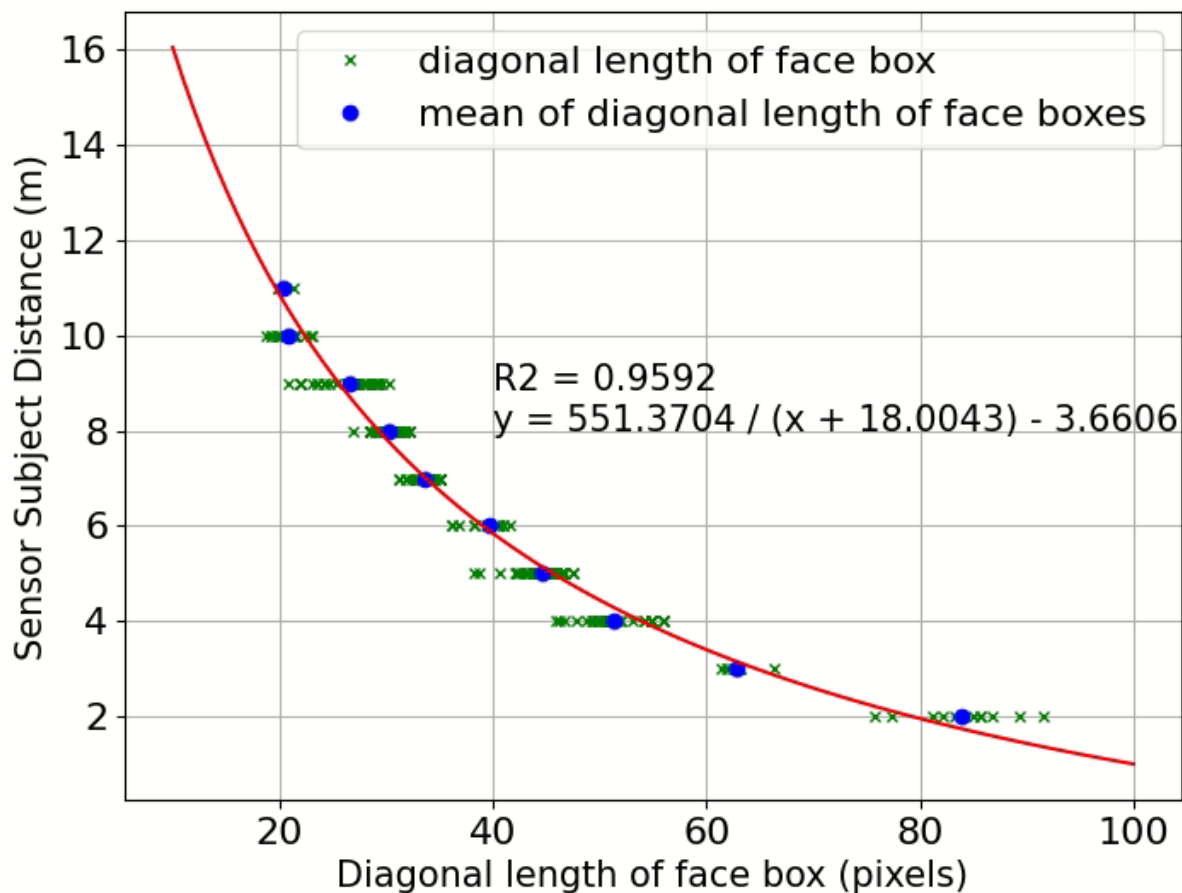


Figure 4-1: Distance estimation using the diagonal length of face box on the collected field data at HKUST North Gate.

Due to the enormous size of the data collected at NG, a preliminary set of filters was being applied to the collected data to create the “raw” data. This initial set of filters aims to remove the data with low confidence in the key points (The confidence of the key points ranges from

0 to 1). The criteria are as follows:

- I. Start date: 2020-09-27
- II. End date: 2021-03-01
- III. Key-point confidence of the left and right eyes > 0.001
- IV. Key-point confidence of the left and right ears > 0.001
- V. Percentage of activated thermal pixels in the thermal face box > 0.2
- VI. The ratio of the thermal face is within (0.5, 3)

Figure 4-2 shows the 3D plot of the “raw” data collected at HKUST’s north gate entrance with our RFSS system over five months. Each of the dots indicates a human at a particular time instance, where red means fever as examined by our system and blue means non-fever. There is no clear pattern on the raw data.

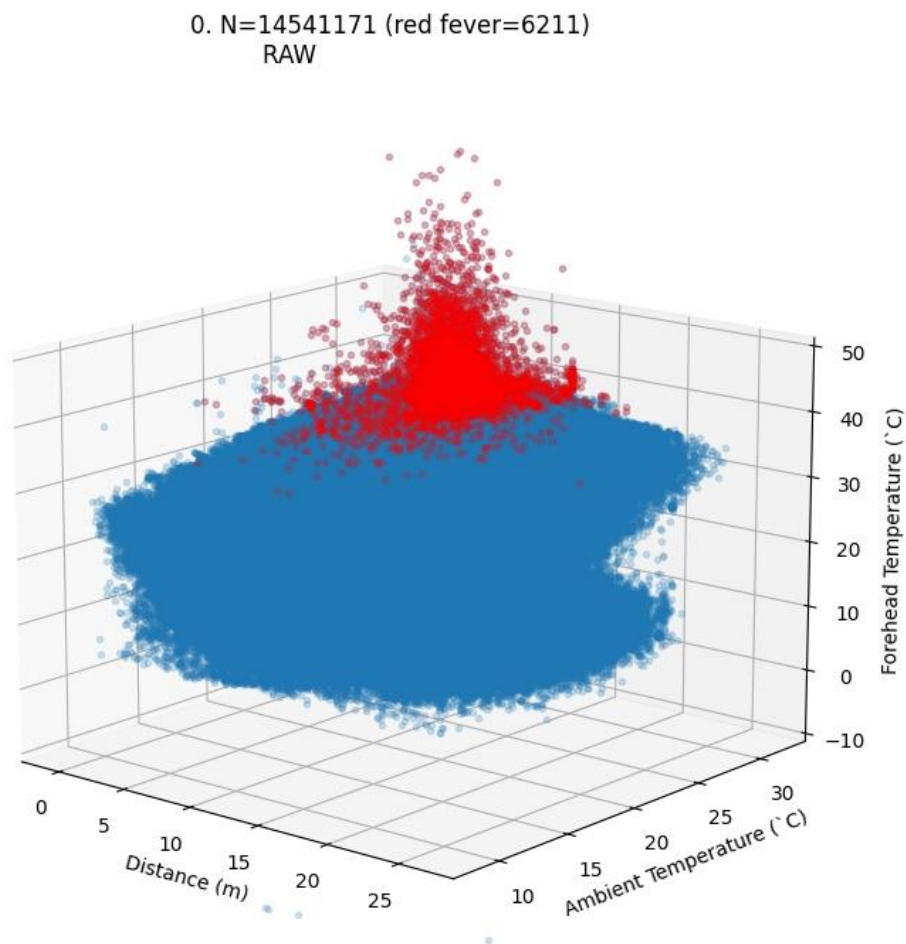


Figure 4-2. 3D plot of the peak temperature with respect to the distance and ambient temperature collected at HKUST’s north gate entrance over 5 months.

4.2.3 Data Filtering

Many factors can affect non-invasive temperature measurements, such as distance, ambient temperature, different head orientations, imperfect synchronization, and more. Data cleaning and mining are required to isolate these effects. The objective is to obtain the data for front-facing subjects with clearly visible faces. A series of six criteria for filtering is being shown as below:

- I. Distance Filter
 - a. The estimated distance between the subject and the camera in (0m – 11m)
- II. “In-Sync” filter (removing unsynchronized data)
 - a. Percentage of activated thermal pixels in the thermal face box > 0.8
 - b. The hottest pixel on the face is not on the edges (within 50% center left-right and 60% top-bottom and starting from 10% from the top)
- III. “Face-Ratio” filter (removing extraordinary long and wide faces caused by key points errors). The face ratio is defined as the height of the face divided by the width of the face.
 - a. The ratio of the color face is within (0.8, 2)
 - b. The ratio of the thermal face is within (0.8, 2)
- IV. Patch filter (removing forehead covered by hairs, hat, or other things)
 - a. Percentage of the pixels with temperature between $T_{\text{peak}} - 1.5^{\circ}\text{C}$ and $T_{\text{peak}} > 0.1$
- V. Head orientation filter to get people who are facing the camera.
 - a. Key-point confidence of the left and right eyes > 0.75
 - b. Key-point confidence of the left and right ears > 0.5
 - c. Key-point confidence difference in left and right ears < 0.05
- VI. Temperature filter to filter out invalid temperature
 - a. Valid temperature is within (20°C, 40°C)

Since the distance estimation is calibrated until 11m (Figure 4-1), only data up until 11m is used. Figure 4-3 shows the measured temperature distribution of the north gate (NG) data after distance filtering.

1. N=7654836 (red fever=4579)
Distance: 0 - 11m

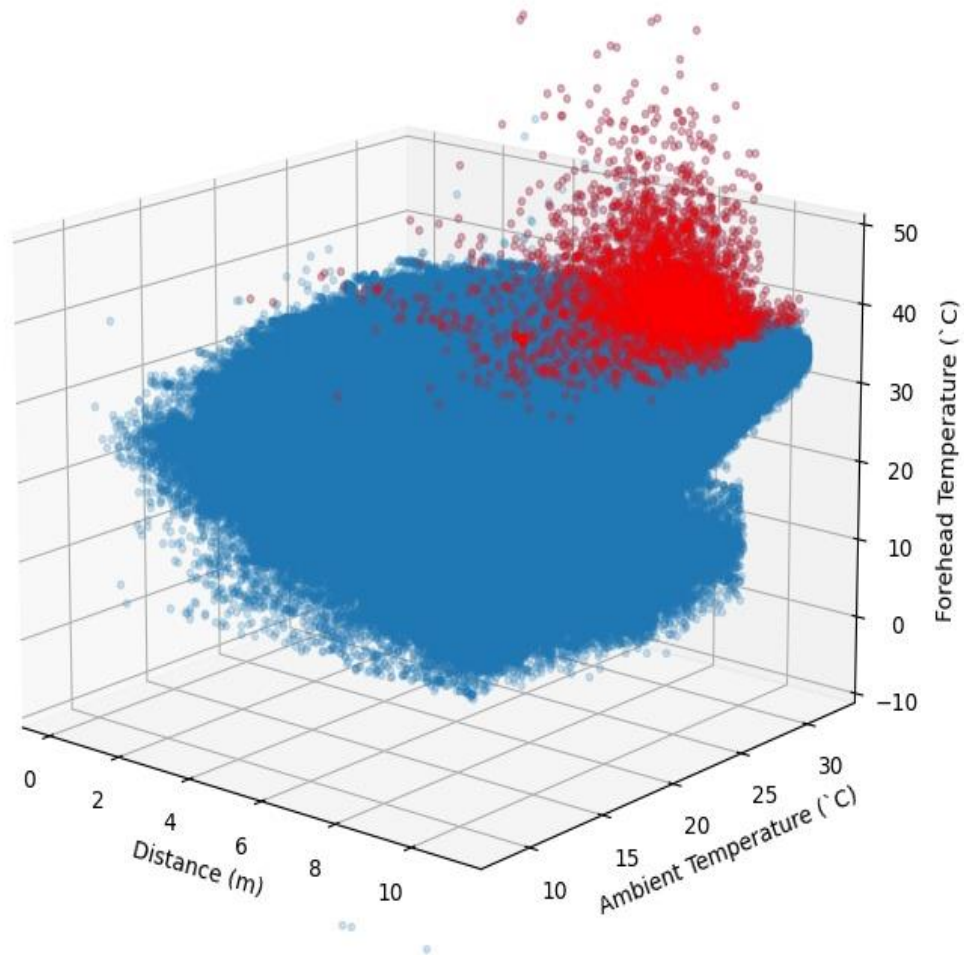


Figure 4-3: NG data after distance filtering.

The table below shows the example of the discarded thermal faces, and the data remains after the distance filter.




















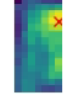


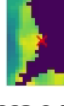
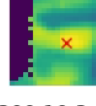
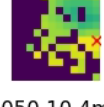
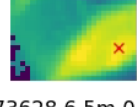
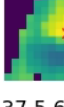





Discarded by the distance filter	1820593 12.9m 0.81 Tobj=30.7C@28.5C 	10601566 13.2m 0.28 Tobj=25.2C@20.4C 	8593037 12.2m 0.42 Tobj=29.9C@22.5C 	5966861 14.6m 0.29 Tobj=26.2C@20.8C 
	12340510 12.1m 0.03 Tobj=27.0C@19.3C 	7831325 12.1m 0.02 Tobj=27.7C@20.1C 	13540726 12.6m 0.13 Tobj=26.3C@21.1C 	3650946 12.3m 0.23 Tobj=30.3C@26.5C 
	1293436 12.6m 0.19 Tobj=28.3C@24.5C 	8227471 16.0m 0.90 Tobj=26.6C@21.2C 	6131120 16.1m 0.28 Tobj=26.5C@21.6C 	8737392 14.3m 0.11 Tobj=27.2C@22.1C 
	6942135 12.7m 0.64 Tobj=23.8C@19.6C 	5190294 11.6m 0.33 Tobj=30.3C@24.1C 	10881128 11.4m 0.14 Tobj=28.3C@19.3C 	13466923 12.2m 0.21 Tobj=17.3C@23.7C 
Remaining data	6853280 7.9m 0.08 Tobj=28.7C@17.4C 	4919438 9.3m 0.11 Tobj=33.2C@25.0C 	11286696 3.5m 0.02 Tobj=29.4C@20.5C 	11632113 9.6m 0.04 Tobj=17.9C@8.6C 
	1586155 7.2m 0.24 Tobj=28.3C@27.4C 	864640 10.1m 0.23 Tobj=33.4C@29.2C 	3976594 4.9m 0.06 Tobj=32.3C@26.7C 	10583660 5.2m 0.07 Tobj=31.8C@20.7C 
	1685037 8.7m 0.10 Tobj=34.0C@29.6C 	7020311 4.1m 0.18 Tobj=29.1C@15.3C 	10331663 9.5m 0.07 Tobj=28.8C@19.1C 	7088300 10.3m 0.05 Tobj=23.0C@15.9C 
	8103050 10.4m 0.07 Tobj=30.7C@21.4C 	573628 6.5m 0.10 Tobj=32.3C@28.7C 	7957137 5.6m 0.05 Tobj=30.4C@20.9C 	10498200 10.5m 0.02 Tobj=26.2C@19.4C 

Table 4: Examples of discarded thermal faces by the distance filter and the remaining data

Next, the system only runs at 10 frames per second, and it does not always have the perfect synchronization between color image and thermal image. Therefore, the second set of filters is being applied and filters out the data that is not in sync. Figure 4-4 shows the NG data after distance filtering and removing the unsynchronized data.

3. N= 350337 (red fever= 403)
Peak not on edges. ($0.25 < \text{Peak}_x < 0.75$, $0.1 < \text{Peak}_y < 0.7$)

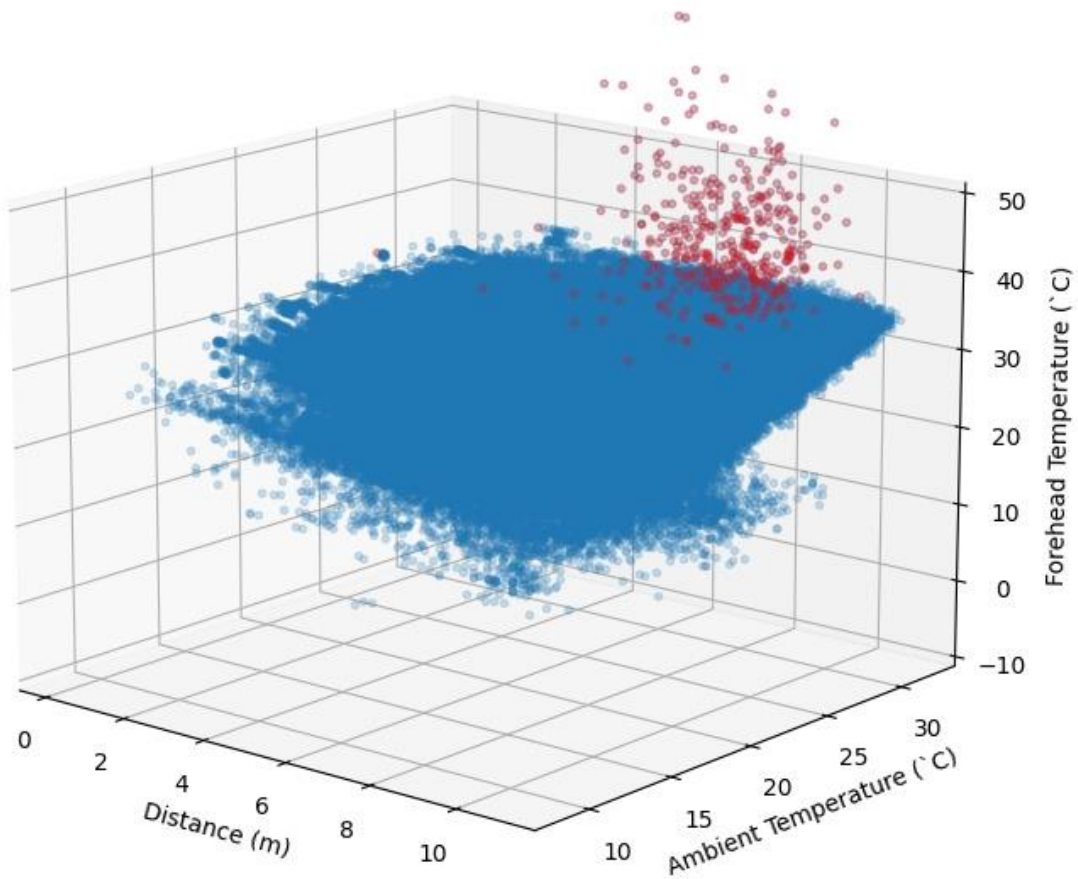


Figure 4-4: NG data after removing the unsynchronized data

The table below shows examples of the discarded thermal faces by the second filter and the remaining data after removing the unsynchronized data.





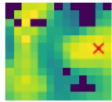










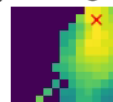

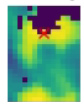
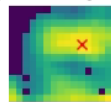
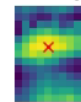
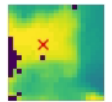
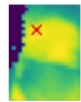
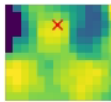
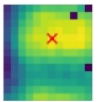
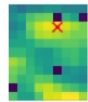
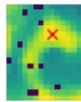
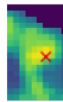
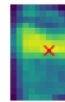
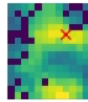
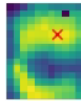

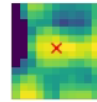
Discarded by “In-Sync” filter	381425 10.0m 0.32 Tobj=33.7C@30.7C 	12464244 10.1m 0.07 Tobj=26.1C@19.4C 	4248725 8.5m 0.07 Tobj=32.8C@26.2C 	6413395 10.4m 0.21 Tobj=24.4C@18.2C 
	2353436 8.5m 0.21 Tobj=32.9C@26.4C 	12452923 10.7m 0.03 Tobj=25.8C@19.6C 	14122725 8.2m 0.03 Tobj=27.3C@20.0C 	3147623 9.4m 0.15 Tobj=33.1C@26.8C 
	2900303 9.6m 0.14 Tobj=30.1C@25.1C 	14102627 11.0m 0.19 Tobj=27.8C@19.9C 	14518472 8.8m 0.56 Tobj=28.0C@20.8C 	6076511 10.0m 0.31 Tobj=27.7C@22.3C 
	4236741 10.9m 0.21 Tobj=28.5C@27.1C 	14422363 10.0m 0.17 Tobj=27.2C@20.8C 	13914114 10.8m 0.11 Tobj=26.9C@21.1C 	13847357 8.5m 0.21 Tobj=32.6C@24.8C 
After removing unsynchronized data	5782927 10.4m 0.17 Tobj=30.5C@23.3C 	6480076 6.0m 0.14 Tobj=31.6C@20.7C 	10833008 7.2m 0.18 Tobj=31.0C@21.0C 	8705654 9.2m 0.09 Tobj=31.1C@21.4C 
	973360 4.6m 0.29 Tobj=33.8C@26.3C 	5456065 3.5m 0.25 Tobj=32.4C@22.3C 	5358285 8.2m 0.15 Tobj=32.2C@26.7C 	8165354 7.8m 0.31 Tobj=29.9C@20.8C 
	4207898 10.1m 0.16 Tobj=33.3C@28.3C 	4102882 6.1m 0.12 Tobj=33.4C@25.4C 	10545851 8.1m 0.07 Tobj=29.9C@19.4C 	14259092 6.7m 0.09 Tobj=29.9C@20.5C 
	6418907 8.4m 0.15 Tobj=29.7C@18.3C 	12875692 9.0m 0.21 Tobj=31.4C@17.7C 	10230640 10.7m 0.14 Tobj=28.2C@16.9C 	3857138 9.2m 0.14 Tobj=31.4C@25.1C 

Table 5: Example of the thermal faces removed by the second set of filters and the remaining data. The second set of filters keeps the thermal faces with more than 80% active thermal pixels, and the hottest pixel on the face does not lie on the edges of the face.

Due to the limitation of the Open-Pose key points detector, the key points from two or multiple nearby persons can be joined together as one single person when it is crowded and under different kinds of occlusion. Consequently, the predicted face box can be extremely long or wide, and covers faces of two or multiple persons. This phenomenon is not desired

for the study of the effects of ambient temperature on non-invasive temperature measurement.

Face ratio is defined as the face length divided by the face breadth. The filter is being applied on two kinds of faces where one is detected in the color image by Open-Pose (“color face”), and another one is being transformed onto the thermal image coordinate space via homography transformation (“thermal face”). Figure 4-5 shows the data after long and wide faces are being removed.

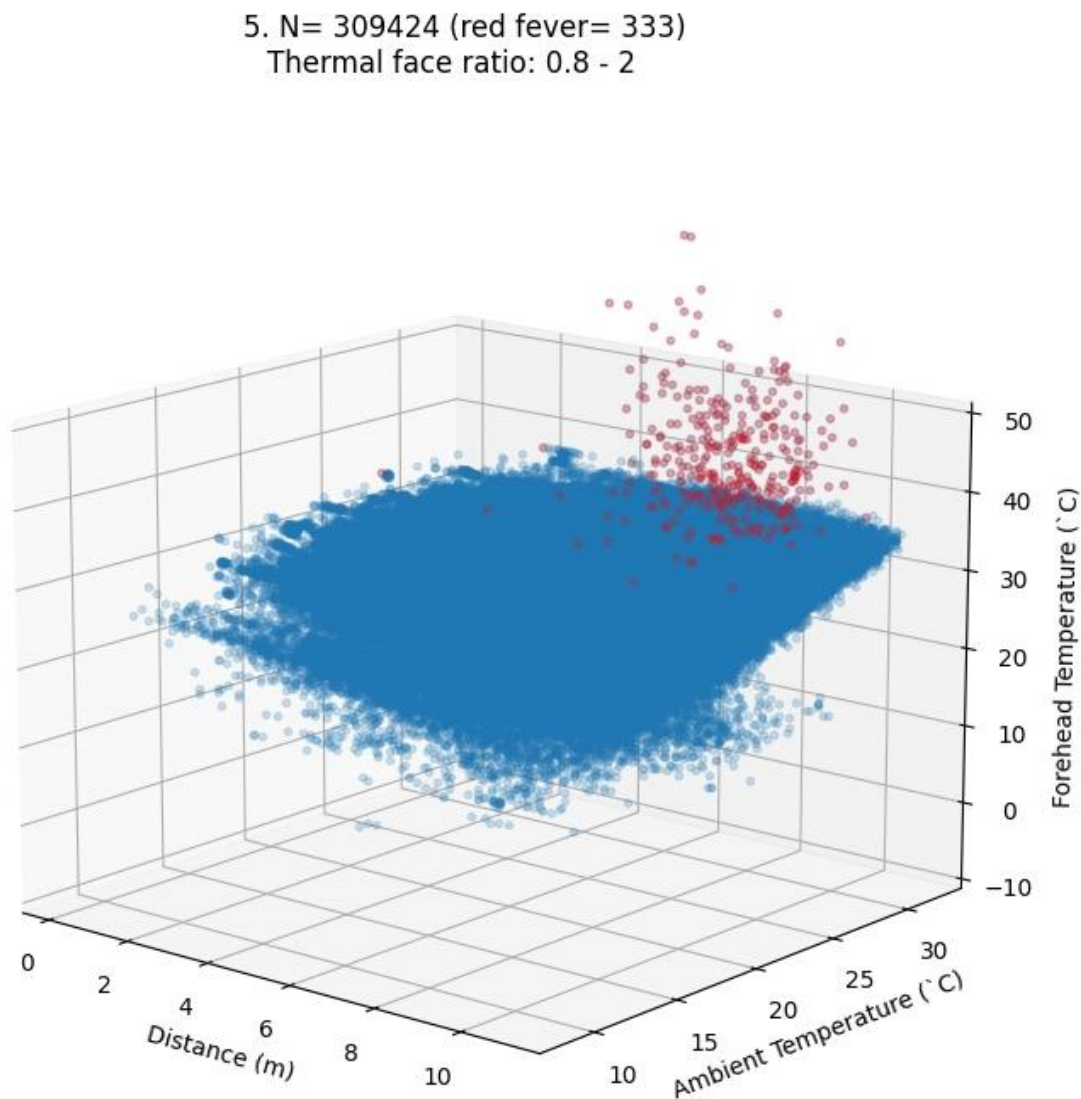


Figure 4-5: NG data after removing the extremely long and wide faces.

The table below shows the example of discarded thermal faces by the “face-ratio” filter and the remaining data.

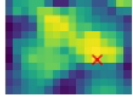
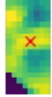


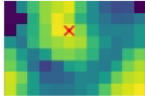
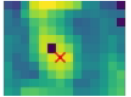
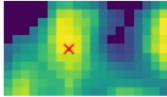
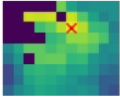
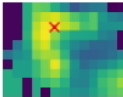
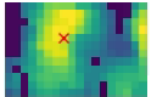
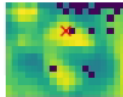

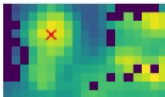
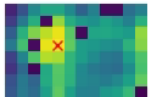


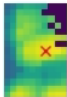
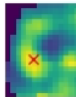
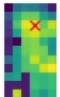
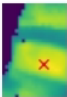
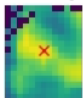

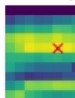
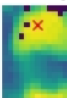
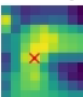


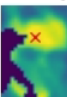
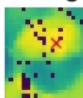
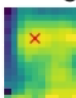
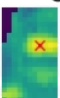
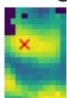
Discarded by the Face- Ratio filter	2308173 7.5m 0.63 Tobj=33.4C@27.7C 	387264 8.5m 0.23 Tobj=34.6C@30.6C 	10343884 10.9m 0.21 Tobj=27.1C@19.1C 	6211777 10.9m 0.15 Tobj=30.0C@17.6C 
	8545403 10.1m 0.25 Tobj=26.6C@21.5C 	5932451 8.4m 0.05 Tobj=30.1C@18.3C 	9828858 7.3m 0.07 Tobj=24.8C@15.1C 	6628294 9.8m 0.12 Tobj=30.9C@18.8C 
	12623158 9.0m 0.16 Tobj=27.5C@21.1C 	7588440 7.6m 0.13 Tobj=28.7C@19.5C 	8274984 6.5m 0.06 Tobj=29.8C@23.1C 	2313032 9.9m 0.36 Tobj=33.7C@27.2C 
	12621496 7.1m 0.04 Tobj=29.2C@21.4C 	12699305 10.4m 0.07 Tobj=25.9C@17.2C 	13308044 11.0m 0.82 Tobj=11.7C@21.1C 	1738438 8.9m 0.52 Tobj=31.8C@26.2C 
After removing the extremely long and wide faces	3961327 9.7m 0.13 Tobj=32.6C@26.4C 	9842385 6.2m 0.04 Tobj=23.8C@13.9C 	6748016 10.4m 0.41 Tobj=28.5C@22.4C 	10570167 4.1m 0.14 Tobj=32.0C@20.5C 
	6681938 8.2m 0.18 Tobj=29.0C@20.5C 	12365853 10.3m 0.11 Tobj=27.6C@20.1C 	12938721 11.0m 0.14 Tobj=18.3C@15.3C 	6052728 6.8m 0.24 Tobj=32.8C@22.4C 
	11023464 10.9m 0.50 Tobj=29.5C@24.9C 	2092414 8.2m 0.16 Tobj=34.5C@27.9C 	10971591 5.8m 0.07 Tobj=26.5C@21.2C 	9020584 4.2m 0.11 Tobj=28.7C@14.1C 
	3300552 5.7m 0.22 Tobj=33.8C@25.2C 	105057 7.9m 0.49 Tobj=31.9C@29.6C 	13739067 7.6m 0.04 Tobj=25.0C@19.5C 	2283806 8.4m 0.32 Tobj=32.8C@26.3C 

Table 6: Example of the long and wide discarded thermal faces discarded by the filter and the remaining data

Next, people might wear hats, or their hair might block the forehead while passing in front of our system. These people often have smaller “hot patches” on their forehead area. The “hot patch” is defined as the pixels with temperature value between $T_{\text{peak}} - 1.5^{\circ}\text{C}$ and T_{peak} , where T_{peak} is the peak temperature of the person measured by the thermal camera. The “hot patch”

percentage is the “hot patch” area over the area of the face box predicted using key points information. A High “hot patch” percentage implies a larger forehead area, which is desired for the study. Figure 4-6 shows the temperature distribution after applying the patch filter.

6. N= 255193 (red fever= 127)
Percentage of pixels with temp in between ($T_{peak} - 1.5^{\circ}\text{C}$) to $T_{peak} > 0.1$

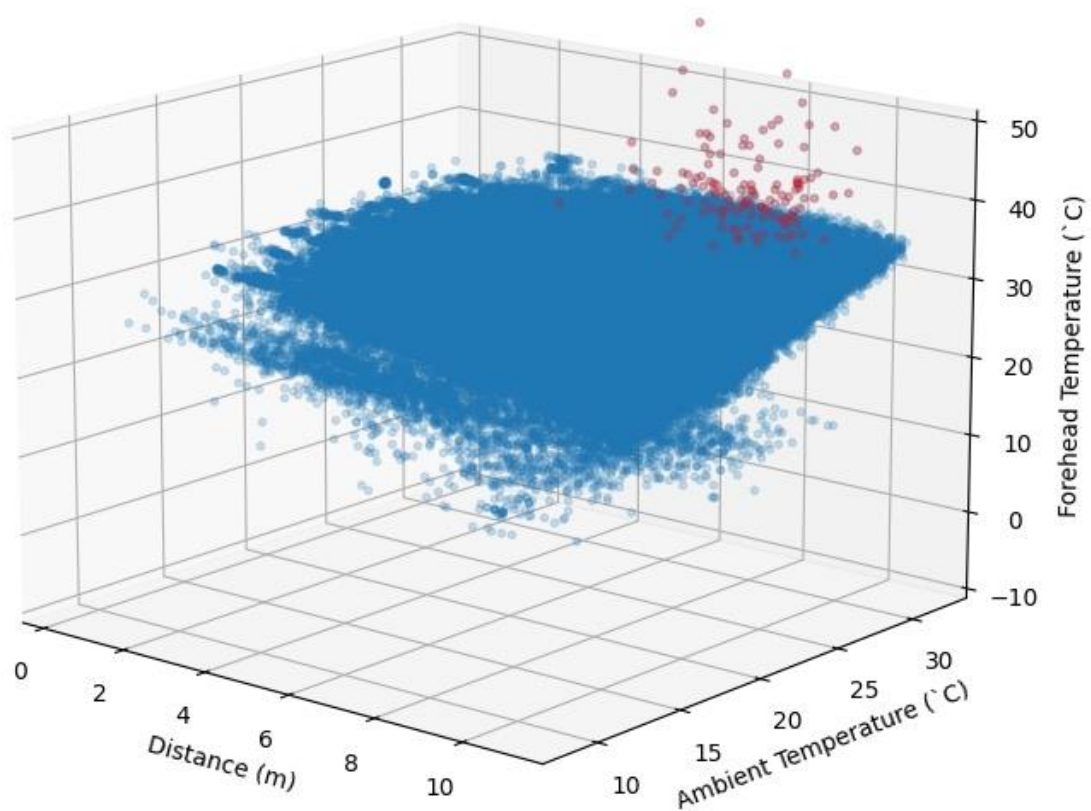


Figure 4-6: Remaining data after the patch filtering removes the people who are not showing their forehead.

The table below shows the example of discarded thermal faces by the occlusion filter and the remaining data.

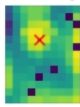
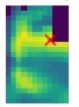
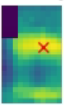
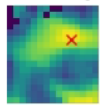
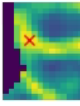
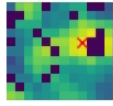
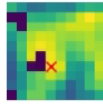
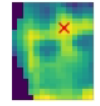
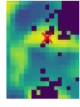
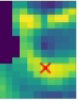
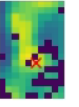
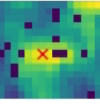
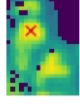
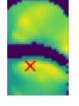
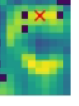
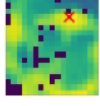
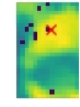
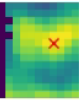
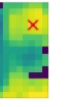
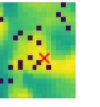
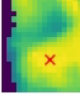
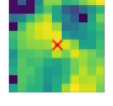
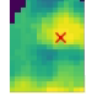
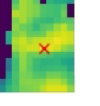

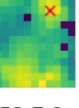
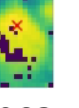
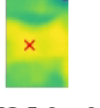
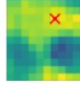
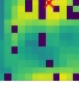

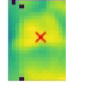
Discarded by the patch filter	14438692 8.3m 0.07 Tobj=29.0C@20.8C 	10603034 6.8m 0.02 Tobj=30.6C@20.5C 	12263793 6.8m 0.08 Tobj=27.7C@18.6C 	11677783 7.3m 0.07 Tobj=27.9C@9.3C 
	9526358 7.1m 0.08 Tobj=25.7C@17.1C 	9235172 9.3m 0.08 Tobj=28.7C@15.2C 	9076066 9.8m 0.09 Tobj=24.8C@15.7C 	8547333 6.4m 0.07 Tobj=29.3C@21.6C 
	9441568 5.3m 0.04 Tobj=26.1C@15.6C 	10765015 8.6m 0.06 Tobj=28.4C@19.9C 	6563809 7.8m 0.05 Tobj=25.4C@20.7C 	11720150 7.2m 0.04 Tobj=27.1C@12.6C 
	8376554 4.9m 0.07 Tobj=30.8C@22.0C 	6599973 2.9m 0.01 Tobj=27.6C@19.2C 	10638531 8.2m 0.09 Tobj=29.5C@20.6C 	14091375 6.1m 0.04 Tobj=30.4C@21.6C 
After removing the thermal faces with small "hot patch"	4915494 4.9m 0.24 Tobj=33.1C@24.9C 	6054626 8.5m 0.19 Tobj=31.8C@22.3C 	4993666 9.3m 0.33 Tobj=34.2C@28.6C 	3590988 6.5m 0.15 Tobj=32.5C@24.9C 
	5384221 5.6m 0.30 Tobj=32.8C@25.3C 	6616365 9.2m 0.26 Tobj=27.4C@18.4C 	3317873 7.1m 0.17 Tobj=30.6C@25.2C 	139588 9.4m 0.15 Tobj=33.1C@28.0C 
	1141603 9.4m 0.25 Tobj=32.1C@25.3C 	8736786 8.9m 0.14 Tobj=32.0C@22.1C 	3561203 5.3m 0.29 Tobj=33.2C@25.3C 	3733702 3.0m 0.31 Tobj=34.5C@25.5C 
	11401309 8.9m 0.23 Tobj=32.0C@24.7C 	2226852 7.9m 0.11 Tobj=33.4C@23.4C 	2507469 6.3m 0.19 Tobj=34.2C@27.5C 	112863 5.0m 0.18 Tobj=34.0C@29.5C 

Table 7: Example of discarded thermal faces by the patch filter, and the remaining thermal faces show more of the forehead region.

Previous studies evaluated temperature measurement with infrared thermography on different parts of the human face like forehead, nose, cheek, ear, mouth, and entire face. A clinical study [52] suggested that front-facing full-face has the best performance for human

temperature measurement and febrile detection. Therefore, the front-facing filter is applied to the NG data to reduce noise in the temperature measurement. A combination of criteria is being applied to get data points where the people are facing forward and towards the camera. To be more specific, high key points confidence of both eyes (> 0.75) and both ears (> 0.5) is to ensure that both eyes and both ears are clearly seen. Furthermore, a small difference (< 0.05) in confidence between the two ears assures the people are not facing sideways. Figure 4-7 shows the temperature distribution of the passersby at NG after head orientation filtering. There is a more apparent pattern shown in the data.

9. N= 18145 (red fever= 1)
conf difference in left and right ears < 0.05

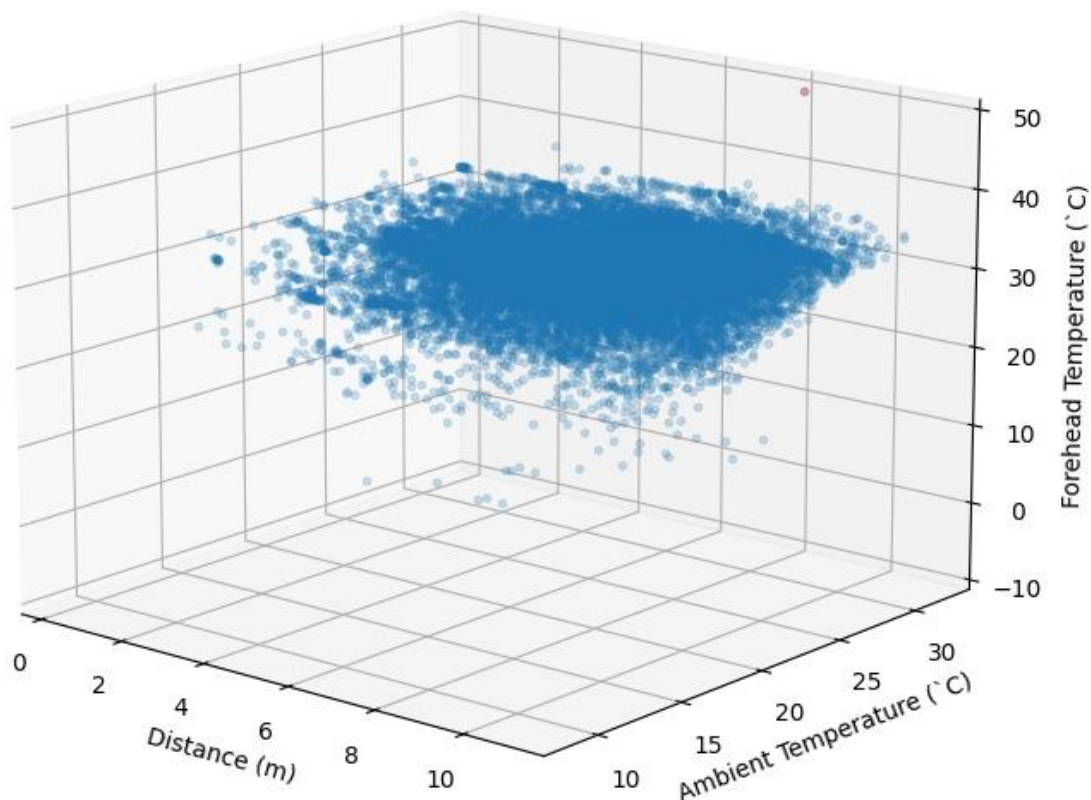


Figure 4-7: Remaining data after head orientation filtering removes the people who are not front-facing.

The table below shows the example of discarded thermal faces by the head orientation filter and the remaining data.

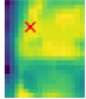
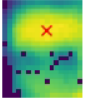
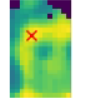
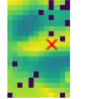
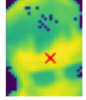

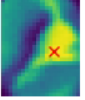
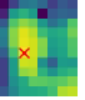
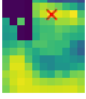

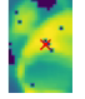
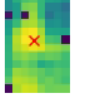
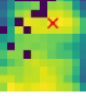
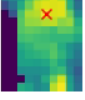
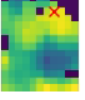
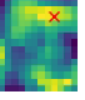
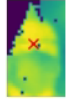
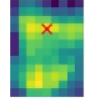
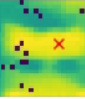
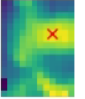
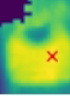
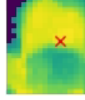
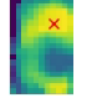
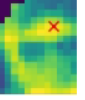
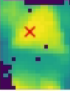
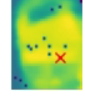
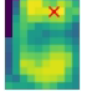


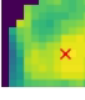
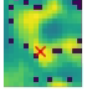
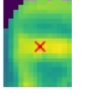
Discarded by the head orientation filter	10581361 5.4m 0.38 Tobj=31.1C@20.6C 	5978854 4.8m 0.23 Tobj=33.5C@21.5C 	2868827 5.7m 0.19 Tobj=31.7C@25.6C 	13996579 7.2m 0.10 Tobj=30.9C@23.8C 
	7881036 2.3m 0.14 Tobj=31.2C@21.8C 	2415920 9.4m 0.44 Tobj=33.1C@23.2C 	7342757 4.9m 0.13 Tobj=33.0C@20.1C 	10910636 10.2m 0.15 Tobj=26.7C@19.1C 
	10750780 9.1m 0.11 Tobj=31.0C@21.2C 	662915 8.5m 0.42 Tobj=33.1C@28.5C 	11320810 3.5m 0.18 Tobj=31.6C@21.0C 	5358416 9.5m 0.66 Tobj=32.0C@26.7C 
	4517969 8.5m 0.17 Tobj=32.6C@24.9C 	10663416 9.7m 0.17 Tobj=32.2C@22.4C 	3471695 8.8m 0.23 Tobj=32.1C@25.2C 	9766989 8.0m 0.22 Tobj=31.4C@18.4C 
After removing the people who are not facing forward	4303392 2.9m 0.17 Tobj=32.2C@23.2C 	2610211 9.6m 0.12 Tobj=29.8C@23.0C 	2473047 5.2m 0.21 Tobj=32.4C@26.2C 	13572127 7.5m 0.14 Tobj=30.4C@19.9C 
	9075966 4.4m 0.30 Tobj=30.1C@15.7C 	2710910 5.8m 0.45 Tobj=33.1C@23.6C 	7229918 7.2m 0.20 Tobj=30.7C@16.3C 	10688 7.7m 0.12 Tobj=33.5C@27.3C 
	3322867 4.7m 0.18 Tobj=33.3C@25.4C 	10089565 2.5m 0.25 Tobj=32.0C@18.4C 	5671172 9.1m 0.19 Tobj=31.3C@19.7C 	540268 7.4m 0.24 Tobj=33.9C@30.1C 
	10045595 10.6m 0.11 Tobj=27.5C@15.9C 	1705389 8.1m 0.31 Tobj=33.5C@28.1C 	6726092 5.8m 0.14 Tobj=30.5C@22.9C 	3750587 5.8m 0.13 Tobj=31.1C@25.0C 

Table 8: Example of discarded thermal faces by head orientation filter to remove people who are not facing forward, there is a higher chance of having forward-facing thermal faces in the remaining data.

Last but not least, the core temperature of a living human is in the range of 36.5°C to 37.5°C. Humans in hypothermia (< 35°C) or hyperpyrexia (> 41.1°C) [56] require medical attention, and are less likely to be in the dataset. Due to the effects of distance and ambient

temperature, the temperature measured by the thermal camera should be lower. Therefore, temperature filtering ranging from 20°C to 40°C is applied. Figure 4-8 shows the remaining data after all the filtering criteria to retain good quality data. There are 18,116 data points left in the dataset.

10. N= 18116 (red fever= 0)
Measured temperature in 20`C - 40`C

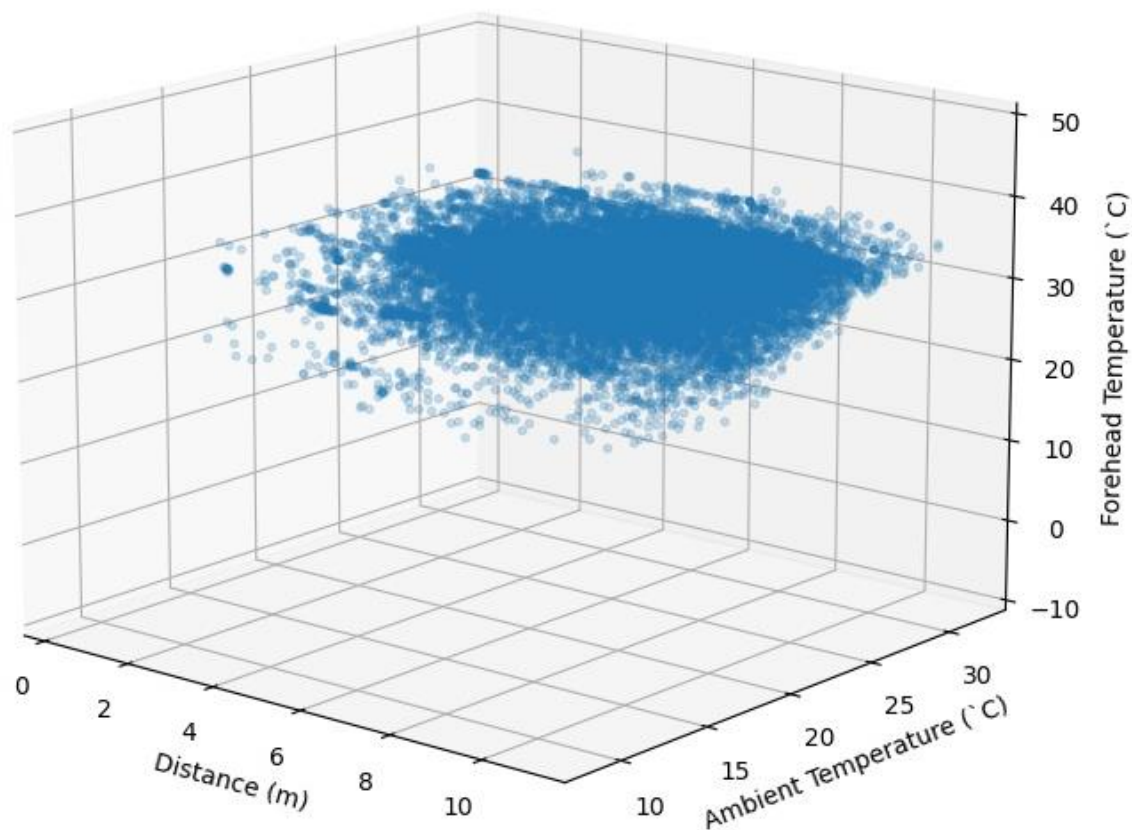


Figure 4-8: Remaining data after the temperature filtering removes the data with temperature lower than 20°C and higher than 40 °C.

The table below shows the example of discarded thermal faces by the temperature filtering. The remaining data is mostly front-facing and showing large area of the skin of the faces.

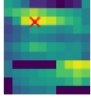
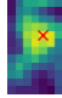
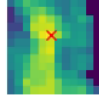
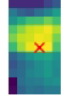
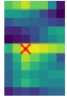
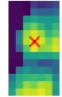

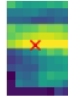
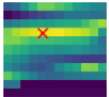
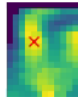
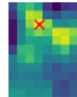



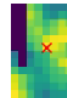
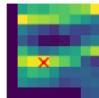

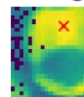
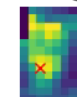
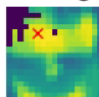
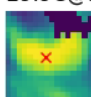
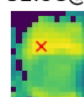
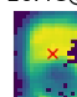
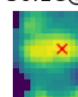
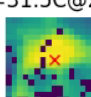
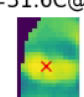

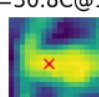
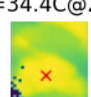
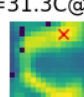


Discarded by temperature filter	12905457 9.9m 0.12 Tobj=18.4C@9.8C 	9015003 10.6m 0.13 Tobj=19.6C@14.1C 	11655603 8.7m 0.26 Tobj=16.0C@8.8C 	13446794 10.8m 0.33 Tobj=15.7C@20.4C 
	13001786 10.8m 0.10 Tobj=16.6C@16.7C 	11652097 9.8m 0.11 Tobj=15.5C@8.7C 	13039616 10.3m 0.19 Tobj=15.7C@15.3C 	13127238 9.4m 0.23 Tobj=14.7C@18.9C 
	13419794 9.2m 0.42 Tobj=13.7C@21.8C 	12118577 7.4m 0.14 Tobj=18.4C@15.5C 	11678489 10.6m 0.10 Tobj=19.3C@9.4C 	3672227 10.2m 0.12 Tobj=54.4C@26.9C 
	11800737 10.5m 0.18 Tobj=17.8C@12.1C 	13260259 10.6m 0.35 Tobj=13.8C@23.3C 	9688215 10.1m 0.52 Tobj=18.0C@14.4C 	13355691 10.7m 0.30 Tobj=12.8C@21.2C 
	3081811 10.3m 0.53 Tobj=27.2C@24.7C 	9043763 5.1m 0.22 Tobj=28.2C@14.1C 	4455585 10.6m 0.37 Tobj=29.8C@23.9C 	11159415 5.9m 0.20 Tobj=30.4C@22.9C 
	7470253 6.7m 0.16 Tobj=29.9C@17.6C 	3479859 6.6m 0.26 Tobj=32.8C@25.4C 	11810347 4.5m 0.18 Tobj=26.4C@11.5C 	4861861 6.9m 0.11 Tobj=30.1C@23.0C 
	5970601 6.4m 0.15 Tobj=31.5C@20.9C 	11453931 4.9m 0.13 Tobj=31.6C@22.2C 	11280972 4.9m 0.21 Tobj=28.8C@20.4C 	7799622 6.6m 0.22 Tobj=30.8C@19.2C 
	3387267 2.0m 0.21 Tobj=34.4C@25.4C 	13776917 6.6m 0.13 Tobj=31.3C@21.3C 	1731210 9.1m 0.36 Tobj=34.2C@26.3C 	7812249 8.0m 0.24 Tobj=29.5C@19.5C 

Table 9: Example of thermal faces not in the range of 20°C to 40°C and the remaining thermal faces.

After the six sets of filtering, 18116 data points are left, and the majority of the thermal faces should be showing the forehead region. Figure 4-9 shows a more apparent pattern after the series of filtering.

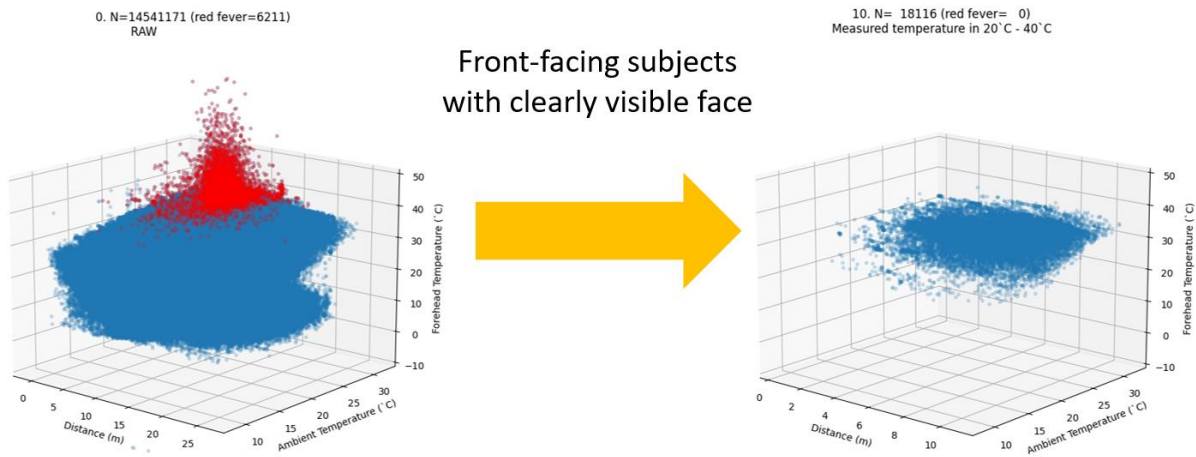


Figure 4-9: Data visualization before and after the data filtering. There is a more apparent pattern shown in the filtered data.

4.3 Results and Analysis

4.3.1 Comparison of the Field Data with the Experimental Data

Figure 4-10 compares the temperature collected in the experiment mentioned in study one and the temperature collected at NG (field data). The experimental data were collected under the ambient temperature of 23.46°C with an S.D. of 0.05°C . The field data collected at NG are with the temperature at $23.5^{\circ}\text{C} \pm 0.2^{\circ}\text{C}$. The two data overlap, but the field data is noisier than the experimental data. The two datasets show consistency in temperature measurements. At NG, the passersby usually do not get close to our system. Therefore, there are fewer people at a distance of less than 3m from the thermal camera.

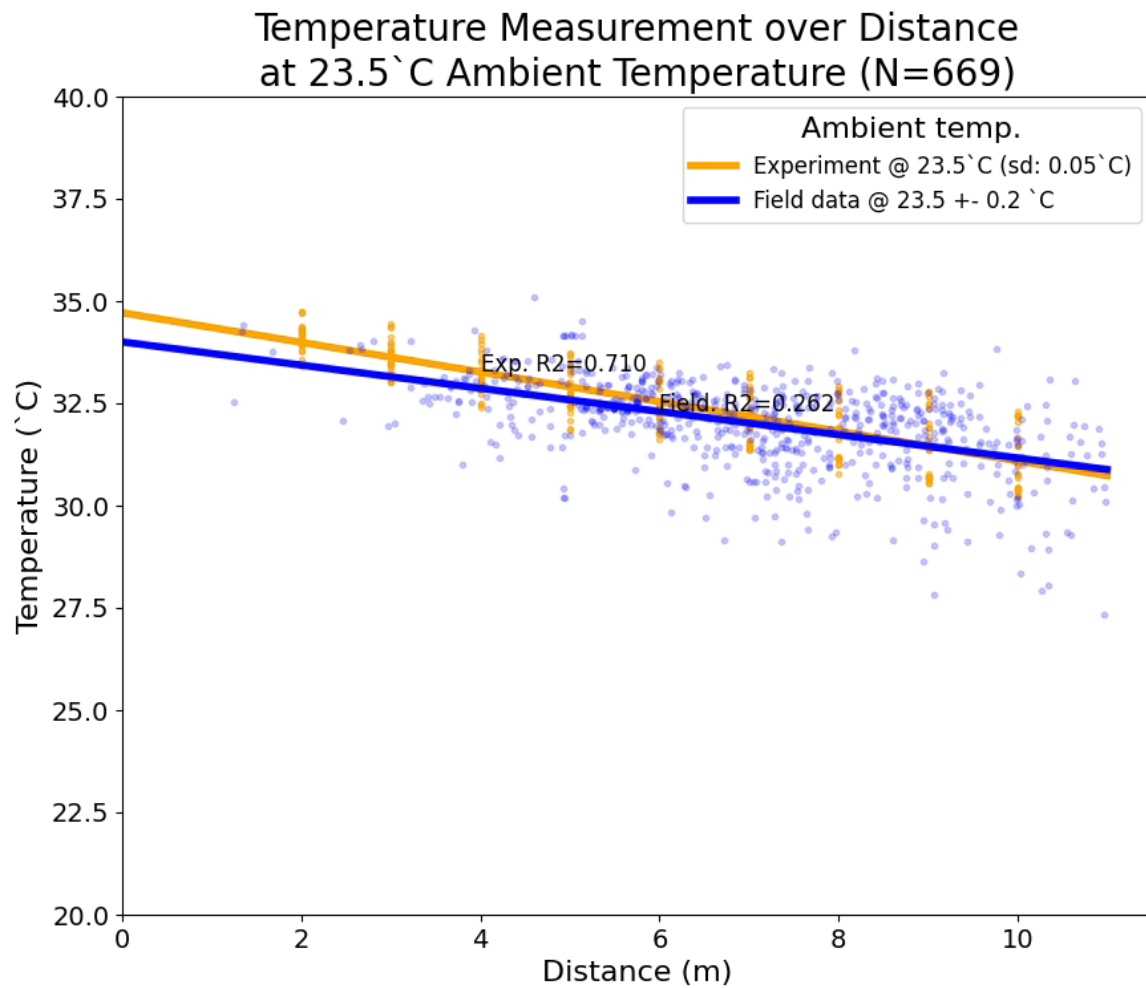


Figure 4-10: Temperature measurement comparison of the field data and the experimental data over distances at 23.5`C ambient temperature.

Figure 4-11 shows the example of the thermal faces from the field data.

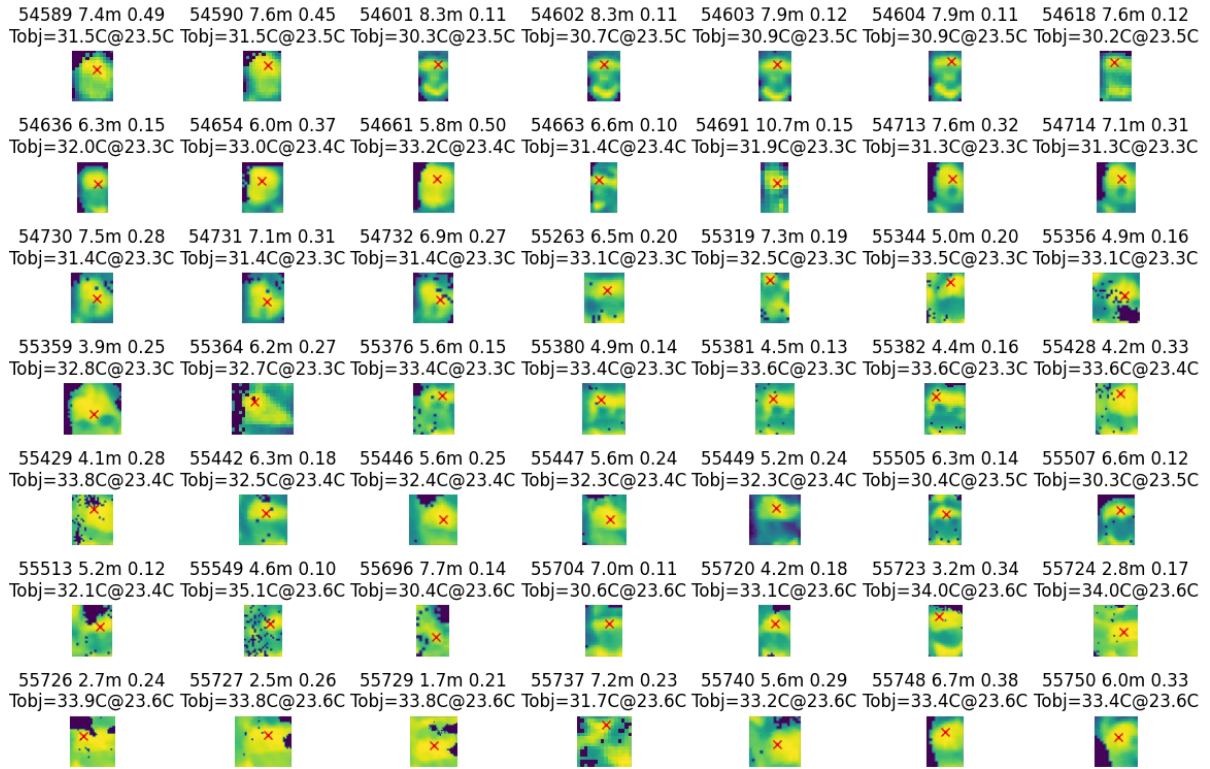


Figure 4-11: Example of the thermal faces under 23.5°C ambient temperature.

4.3.2 Effects of Ambient Temperature on Temperature Measurements

A standard dataset is required to study the joint effects of distance and ambient temperature. Therefore, another smaller common dataset is extracted at eight distances, and seven ambient temperatures from the filtered dataset (after ten filtering criteria mentioned) showed in Figure 4-8. The data in the range of plus and minus 0.5m for each of the distances and a range plus and minus 1 degree Celsius for each ambient temperature was extracted to form the smaller common dataset to facilitate the study of joint effects between distance and ambient temperature. The number of data points in the smaller common dataset becomes 12942.

Figure 4-12 shows the temperature measurement over distances in different ambient temperatures. From the figure, the effects of distance at each ambient temperature are still present. However, the more interesting finding is that there is an interaction between distance and ambient temperature. The lower the ambient temperature, the higher the drop in temperature measurement over further distances. At a distance equal to 0m, the temperature does not converge to a single value. There are two reasons behind it; the first is that the skin temperature can be reduced by heat loss due to the cold environment resulting in lower temperature reading, as shown in [8]. The second reason is due to the automatic

self-calibration of the FLIR E8xt camera. The ambient temperature can affect the camera calibration.

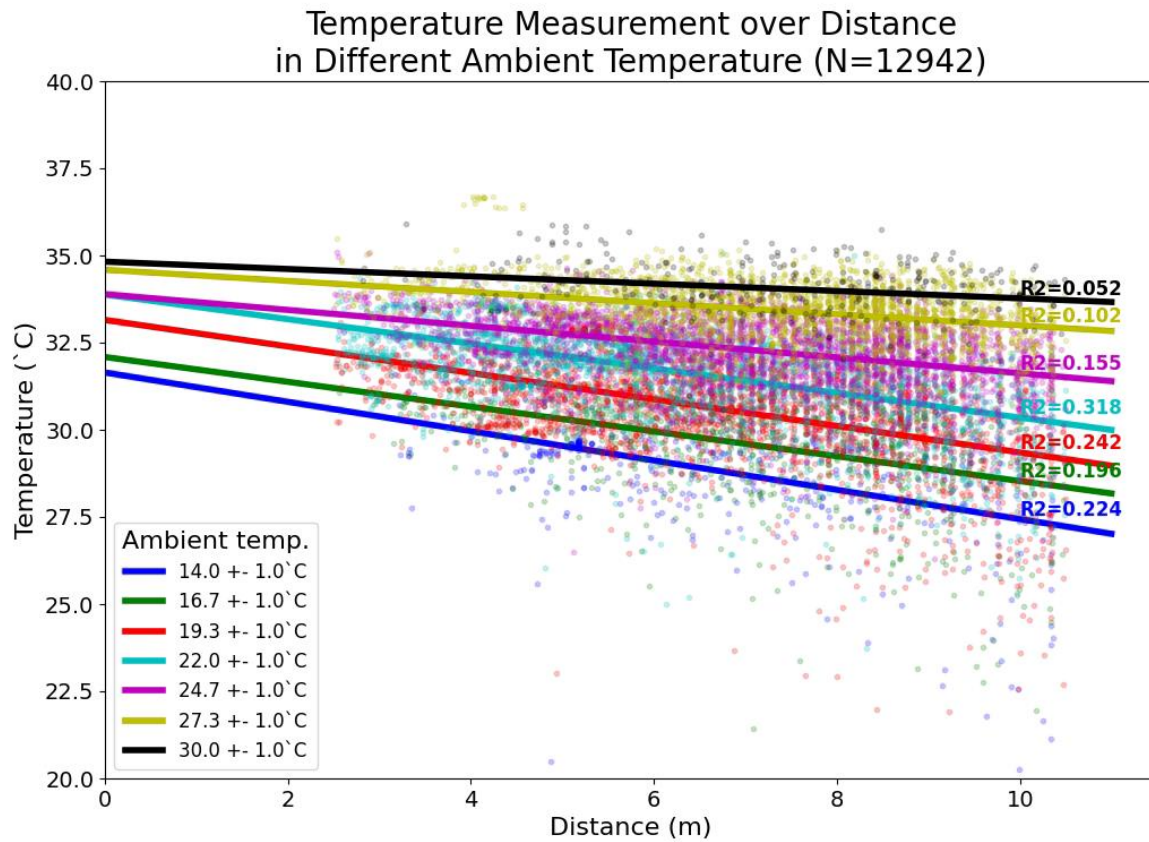


Figure 4-12: Temperature measurement over distance in different ambient temperatures

Figure 4-13 shows the same smaller common dataset with 12942 data points but over different ambient temperatures. In the figure, results show that the ambient temperature significantly reduces the non-invasive temperature measurement linearly [ANOVA: $F(1, 12938) > 10$, $p = 0.001$]. The quadratic term [$F(1, 12938) < 3$, $p = 0.155$] and cubic term [$F(1, 12938) < 2$, $p = 0.194$] are not significant. Furthermore, the results in both Figure 4-12 and Figure 4-13 show that there are significant interactions between distance and ambient temperature [ANOVA: $F(1, 12938) > 264$, $p < 0.001$]. At further distances, the ambient temperature has higher effects on the measured temperature.

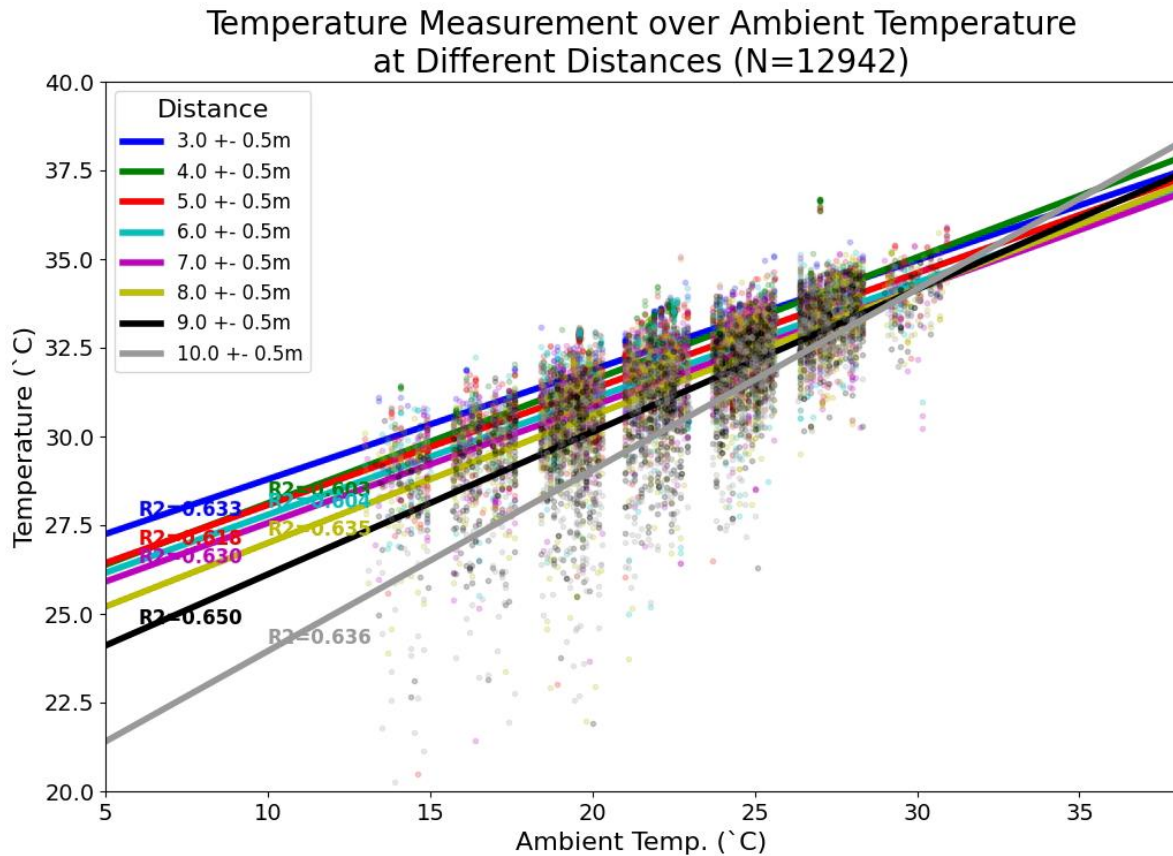


Figure 4-13: Temperature measurement over ambient temperature at different distances.

Figure 4-14 shows that a drop in ambient temperature from 28°C to 14°C reduces non-invasive temperature measurements by 4.1°C to 7.2°C on average, depending on the distance. The results suggest that it is impossible to have accurate fever screening when the ambient temperature varies.

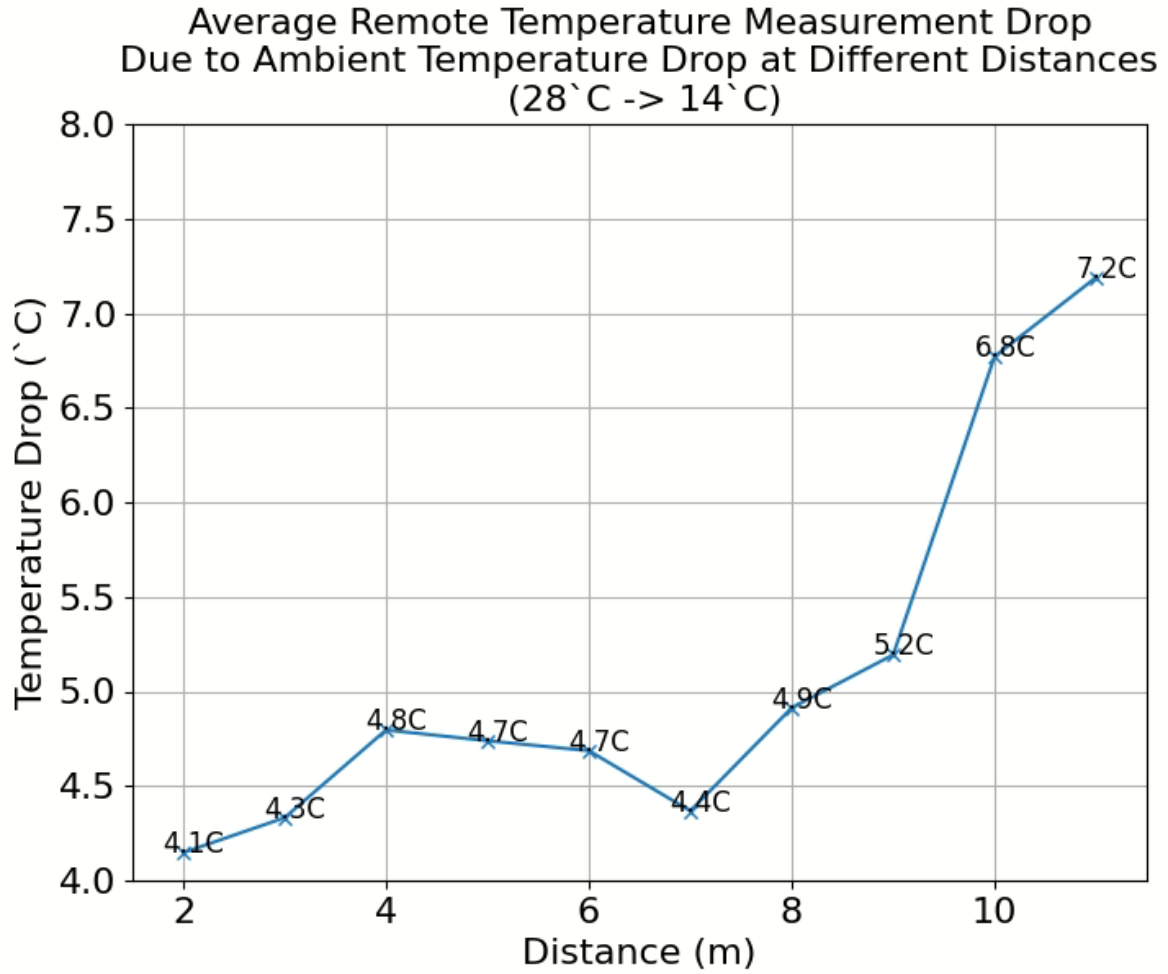


Figure 4-14: A drop in ambient temperature from 28°C to 14°C reduces the non-invasive temperature measurements by 4.1°C to 7.2°C on average, depending on the distance.

4.3.3 Enhanced Thermal Compensation Model for the Joint Effects of Distance and Ambient Temperature

We found that both distance and ambient temperature reduces the non-invasive temperature measurements significantly and linearly. Furthermore, there is an interaction between distance and ambient temperature. Therefore, we modified the thermal compensation model in study one to include the ambient temperature and the interaction between distance and ambient temperature ($a_5 T_{amb}$, $a_6 d * T_{amb}$). As a result, equation (16) is modified as follows:

$$T'_{obj} = \overbrace{a_0 d + a_1 + a_5 T_{amb} + a_6 d * T_{amb}}^{\text{statistical model}} + \overbrace{\sqrt[4]{\frac{M_0 - \hat{M}_{refl} - \hat{M}_{atm}}{\hat{\tau}_{atm} \epsilon_{obj} \sigma}}}}^{\text{physics model}} \quad (17)$$

Where a_5 is the coefficient related to the ambient temperature, and a_6 is the coefficient related to the interaction between distance and ambient temperature.

There is no forehead temperature of the passersby measured by the handheld thermometer. Therefore, the reference temperature of 36.5°C with an S.D. of 0.1°C in study one is used as the reference temperature.

The filtered dataset shown in Figure 4-8 was used to train and test our compensation model. The 18116 data was divided into the training data and testing data randomly, with 90% of them were training data and 10% of them are testing data. Similar to section 3.4.2, the same program was used to train the enhanced compensation model. However, we changed to use 'Powell' instead of using 'L-BFGS-B' method.

	MAE(°C)	RMSE(°C)
Training data (N=16304)		
Measured Temperature	4.799	5.158
Compensated Temperature (Distance only)	1.711	2.167
Compensated Temperature (Ambient only)	0.912	1.238
Compensated Temperature (Distance + Ambient)	0.633	0.863
Compensated Temperature (Distance + Ambient + Interaction between distance and ambient)	0.609	0.836
Testing data (N=1812)		
Measured Temperature	4.805	5.137
Compensated Temperature (Distance only)	1.717	2.141
Compensated Temperature (Ambient only)	0.892	1.201
Compensated Temperature (Distance + Ambient)	0.628	0.858
Compensated Temperature (Distance + Ambient + Interaction between distance and ambient)	0.601	0.836

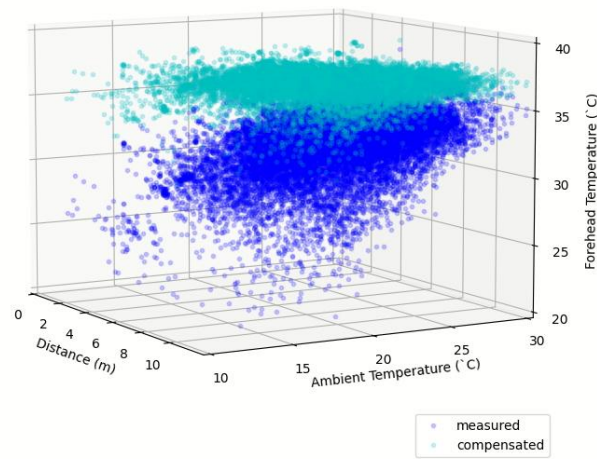
Table 10: Mean Absolute Error and Root Mean Square Error comparison between the measured temperature and compensated temperature vs the reference temperature

The results are shown in Table 10. The MAE and RMSE drop significantly with our compensation model. The RMSE drops to 2.167°C and 1.238°C with compensation for distance only and ambient temperature only on the training data set. It further reduces to 0.863°C with compensation for both distance and ambient temperature. Finally, the RMSE drops to 0.836

°C with compensation for distance, ambient temperature, and interaction between distance and ambient temperature. Similar results can be seen in the testing data.

Figure 4-15 shows the 3D plot of the temperature distribution versus distance and ambient temperature on the filtered dataset (N=18116). The tilted blue surface represents the measured temperature distribution, and the horizontal cyan surface represents the compensated temperatures with our thermal compensation model.

a.
Temperature Distribution of the Measured Temperatures
and the Compensated Temperatures
in the Training Data(N=16304)



b.
Temperature Distribution of the Measured Temperatures
and the Compensated Temperatures
in the Testing Data(N=1812)

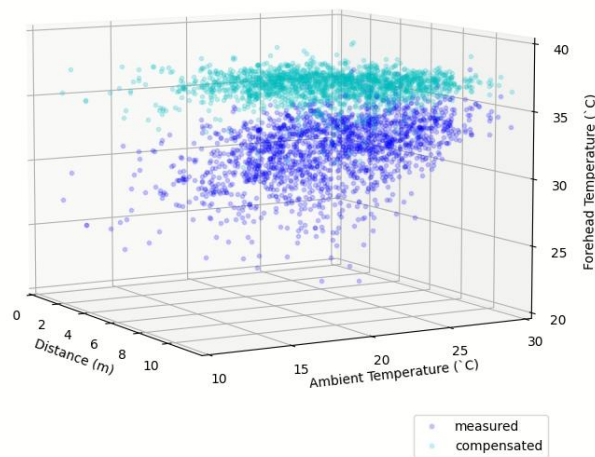


Figure 4-15: 3D visualization of the measured temperature and the compensated temperature versus distance and ambient temperature. (a) Training data. (b) Testing data.

4.3.4 Fever Screening at Different Ambient Temperatures and Different Distances with and without Thermal Compensation

As the main concern is fever screening, we would like to study how the thermal compensation model can improve its accuracy and robustness under different ambient temperatures. As data collected on the field lacked fever suspects, we extrapolated the fever data in study one to study fever screening in different ambient temperatures. As the ambient temperature reduces the non-invasive temperature measurement linearly (Figure 4-13), the reference fever data (pink dots) were extrapolated to different ambient temperatures linearly (purple dots) [the code is in Appendix 3.4, page 108]. It is shown in Figure 4-16. Furthermore, we were interested in three ambient temperatures: the low ambient temperature at 17.5°C, room temperature at 22.5°C, and high ambient temperature at 27.5°C. In particular, the low and high ambient temperatures were chosen to study the possibility of fever screening in a semi-outdoor environment where the ambient temperatures deviated from the room temperature.

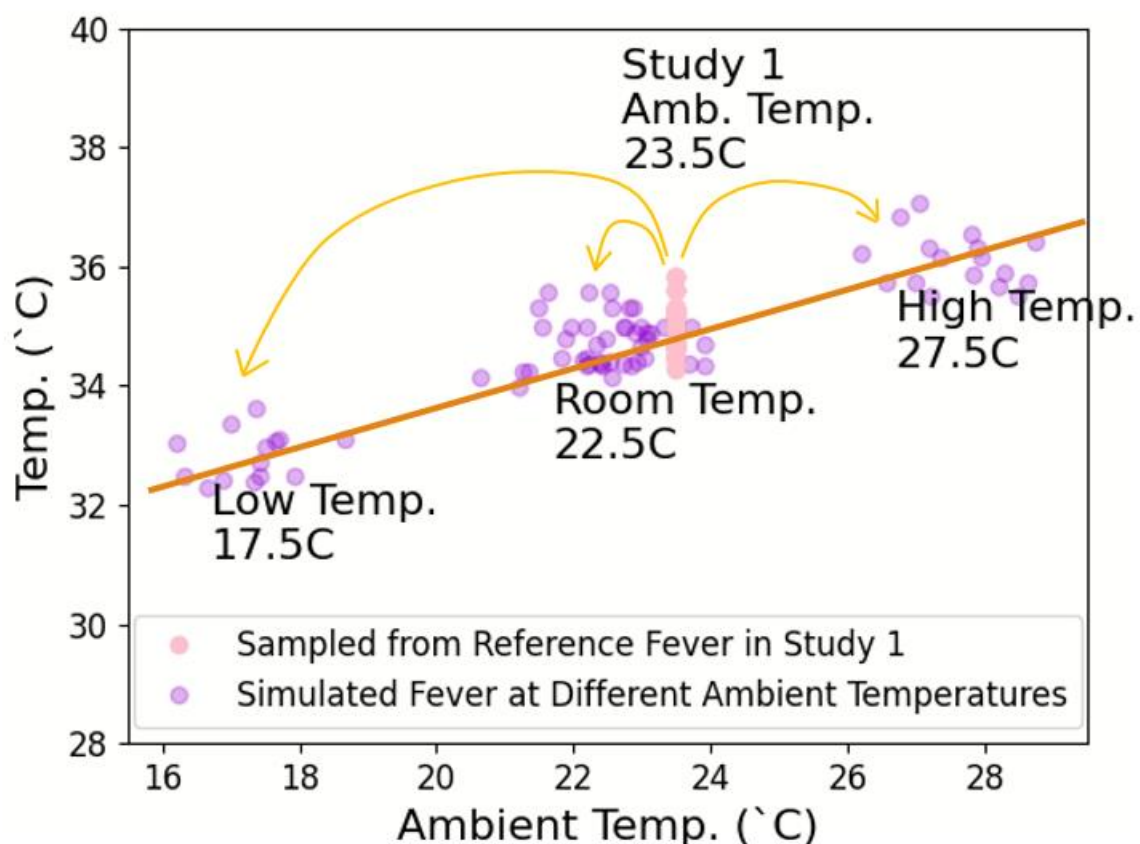


Figure 4-16: Reference fever data extrapolated to different ambient temperatures

The sensitivity and specificity of fever screening with and without our thermal compensation at different distances and different ambient temperatures are shown in Figure 4-17. The X-axes in all the six figures are distance in meter, the Y-axes in the top row are the sensitivity, and the Y-axes in the bottom row are the specificity. The left, middle, and right columns are the low temperature, room temperature, and high temperature. In addition, the green and blue curves are with and without our thermal compensation, respectively. The higher value, the better it is for both the sensitivity and specificity. They are defined as follows:

$$Sensitivity = \frac{True\ Positive}{Total\ Positive\ Population} \quad (18)$$

$$Specificity = \frac{True\ Negative}{Total\ Negative\ Population} \quad (19)$$

The results show that it is impossible to detect fever with $\geq 90\%$ for sensitivity and specificity under changing ambient temperatures without compensation. It is shown in Figure 4-17A that the sensitivity is low, and this indicates a high missing rate without our thermal compensation. Similarly, Figure 4-17F shows low specificity without the thermal compensation, indicating a high false alarm rate during hot weather. This finding is consistent with ISO and FDA regulations, where fever screening systems work effectively only when the systems are used in the right environment or location[57]. On the contrary, we showed a possibility of fever screening in changing ambient temperatures. Lastly, the temperature screening distances with $\geq 90\%$ for sensitivity and specificity at different ambient temperatures are shown in Table 11.

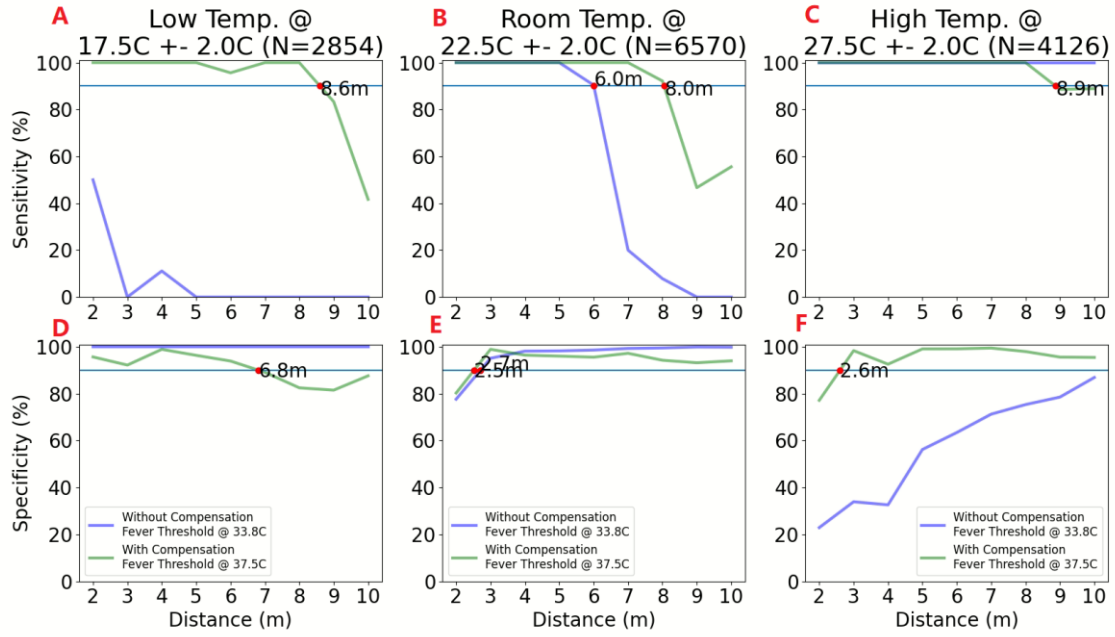


Figure 4-17: Sensitivity and specificity of fever screening with and without our thermal compensation at different distances and different ambient temperatures.

	Low Temp. (17.5°C)	Room Temp. (22.5°C)	High Temp. (27.5°C)
Without Compensation	-	2.7m – 6.0m	-
With Compensation	2m – 6.8m	2.5m – 8m	2.6m – 8.9m

Table 11: Comparison of the temperature screening distance ($\geq 90\%$ sensitivity and specificity) with and without our thermal compensation.

4.4 Discussion and Conclusion

This chapter studies the joint effects of distance and ambient temperature for non-invasive temperature measurement for temperature screening applications. We found that decreasing ambient temperature significantly reduces the values of the non-invasive temperature measurements. Furthermore, there is a linear relationship between the changes in ambient temperature and non-invasive temperature measurement. A drop in ambient temperature from 28°C to 14°C can reduce non-invasive temperature measurements by 4.1°C to 7.2°C on average. Moreover, the decrease in the non-invasive temperature measurements also depends on the distance. Our data showed a significant interaction between distance and ambient temperature on the non-invasive temperature measurements.

With our proposed enhanced thermal compensation model, the MAE and the RMSE drop from 4.799°C to 0.607°C and 5.158°C to 0.836°C, respectively. The results suggest that our thermal compensation model creates a possibility of fever screening with infrared thermography (IRT) in a semi-outdoor environment where the ambient temperature changes.

As data collected on the field did not include fever suspects, we conducted a simulation with the reference fever data in study one. Our simulation results show that it is impossible to detect fever with $\geq 90\%$ sensitivity and specificity with changing ambient temperature without any thermal compensation. This finding is consistent with ISO and FDA regulations, where fever screening systems work effectively only when the systems are used in the right environment or location. However, we enabled fever screening at different ambient temperatures and distances with our proposed model and compensation.

Nonetheless, other factors can affect the temperature measurement and need to be considered in a more general thermal compensation model. One possibility to counteract the noise from those factors is to utilize temporal information of the same person to suppress the temperature measurement noise from some of the factors. The investigation of using temporal information with human subject tracking is described in the following chapter.

Chapter 5 STUDY THREE: REDUCTION OF NOISE IN NON-INVASIVE TEMPERATURE MEASUREMENT WITH HUMAN TRACKING

Summary

This chapter reports using the temporal consistency in human body temperature to suppress the noise in non-invasive temperature measurement.

5.1 Introduction

Non-invasive temperature measurement is challenging at longer distances and under uncontrolled situations. Apart from the distance and ambient temperature, more factors can introduce undesirable noise in non-invasive temperature measurements. As reviewed in [58], the factors are classified into three major classes, environment factors (like atmospheric pressure, sources radiation), individual factors (like gender, age, skin emissivity), and technical factors (like camera features, region of selection for temperature measurement). Unfortunately, it is impossible to suppress the noise from all the factors. In this chapter, we investigate the possibility of human subject tracking in noise suppression to increase the confidence in temperature estimation for each of the individuals.

5.2 Method

5.2.1 Data Collection

The data collection is similar to section 4.2.2. The data used in this chapter were collected with our developed RFSS installed at the north gate (NG) on the HKUST campus. Data collected on 2020-10-01 was used for this study. The sensor-subject distances range from 0.9m to 24.4m. The ambient temperature on that day was 26.7°C to 28.9°C, with a mean of 27.9°C.

5.2.2 Data Processing and Data Filtering

This chapter aims to study the possibility of noise suppression in non-invasive temperature measurement by utilizing the temporal consistency in human body temperature. A simple proximity tracker which associates the nearest human together in the present and past frames is being applied on the collected at HKUST north gate system.

Subjects who appeared less than 5 seconds were being discarded from the study. In addition, subjects with less than 8 data points per second are discarded. Lastly, subjects who do not

have any “good face” captured by the system during the whole tracking period are also discarded. The “good face” is defined as the photo of the face in a thermal image (“thermal face”) that is forward-facing, such that the forehead is clearly visible. A series of filters similar to section 4.2.3 is applied to acquire high-quality subject data. The filters are defined as the following:

- I. Removing unsynchronized data
 - a. Percentage of activated thermal pixels in the thermal face box > 0.8
 - b. The hottest pixel on the face is not on the edges (within 50% center left-right and 60% top-bottom and starting from 10% from the top)
- II. Removing extraordinary long and broad faces (caused by key-points errors), the face ratio is defined as the height of the face divided by the width of the face.
 - a. The ratio of the color face is within (0.8, 2)
 - b. The ratio of the thermal face is within (0.8, 2)
- III. Patch filter (removing forehead covered by hairs, hat or, other things)
 - a. Percentage of the pixels with temperature between $T_{\text{peak}} - 1.5^{\circ}\text{C}$ and $T_{\text{peak}} > 0.1$
- IV. Head orientation filter to get people who are facing the camera.
 - a. Confidence of the left and right eyes > 0.75
 - b. Confidence of the left and right ears > 0.5
 - c. Confidence difference in left and right ears < 0.05
- V. Temperature filter to filter out invalid temperature
 - a. Valid temperature is within (20°C , 40°C)

5.2.3 Temperature Correction with the Thermal Compensation Model and Temporal Information

Valid temperature is defined as the temperature measurement that falls into the temperature range of an average human ($35^{\circ}\text{C} - 37.5^{\circ}\text{C}$) [56]. The oral temperature has a mean of 36.57°C and S.D. of 0.42°C , as reported in [59]. The forehead temperature usually is 0.3 to 0.6 degrees lower than an oral temperature [60]. Specifically, a temperature larger than 34.9°C is counted as a valid temperature.

Assuming temporal consistency in the human body temperature within a subject, utilizing the historical temperature measurements of the same person can improve the accuracy and

robustness of the temperature estimation for that subject. Figure 5-1 shows the temperature and distance information of a subject with ID 397 over time. The measured temperature, compensated temperature, and estimated temperature (utilizing temporal consistency) of the subject are shown. There are two steps in our proposed method. First, we applied our thermal compensation to the measured temperature to get the compensated temperature (blue dots to cyan dots). Then, a rolling median (yellow line) is applied to the historical valid compensated temperature values (green dots) to estimate the temperature of the subjects.

In Figure 5-1, the subject was back-facing the camera from time to time while walking away from our system. It caused the measured temperature to be much lower than an average human temperature more than 50% of the time, even after our thermal compensation for distance and ambient temperature. Thus, utilizing temporal information of the subject can suppress the noise due to backward-facing.

Figure 5-2 shows the temperature and distance information of a subject with ID 5250 over time. This pattern shows a typical subject that walked towards and left the field of view of our system.

ID=397, median:35.8C, 70%-tile: 35.9C @ Tamb = 27.1C
percentage of valid temperature over whole period before temporal correction: 49.1%
percentage of valid temperature over whole period after temporal correction: 96.1%

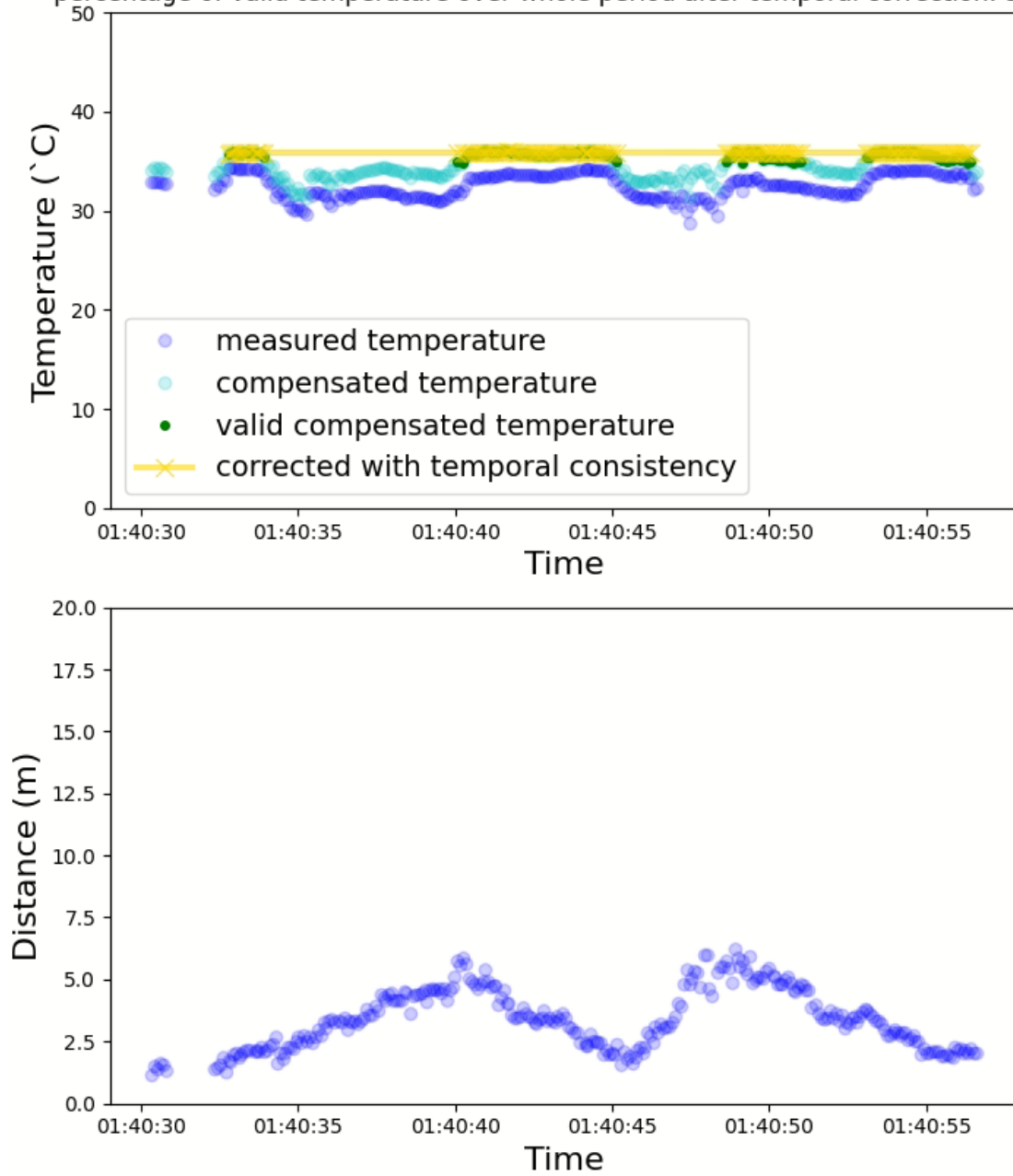


Figure 5-1: Temporal information of the subject with ID 397. Back-facing the camera causes the measured temperature to be much lower than an average human temperature. Utilizing temporal information can suppress the noise due to back-facing.

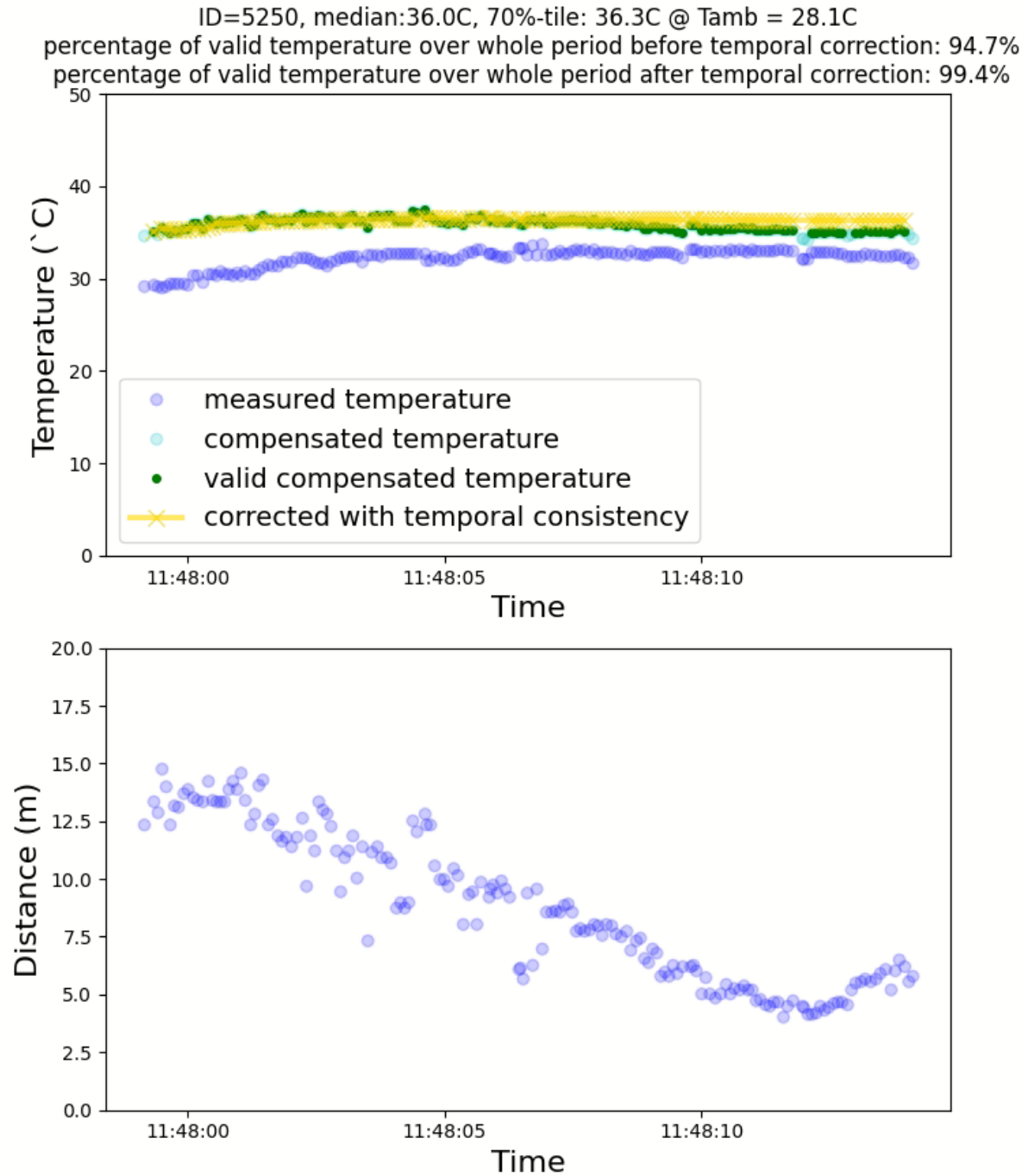


Figure 5-2: Temporal information of the subject with ID 5250. A typical subject walked towards and left the field of view of our system.

5.3 Results and Analysis

5.3.1 Sensitivity Analysis on the Percentile of Temperature Distribution Used for Temperature Estimation

Figure 5-3 shows that the temperature distribution of the 53 subjects changes when choosing different percentile values for the temperature estimation.

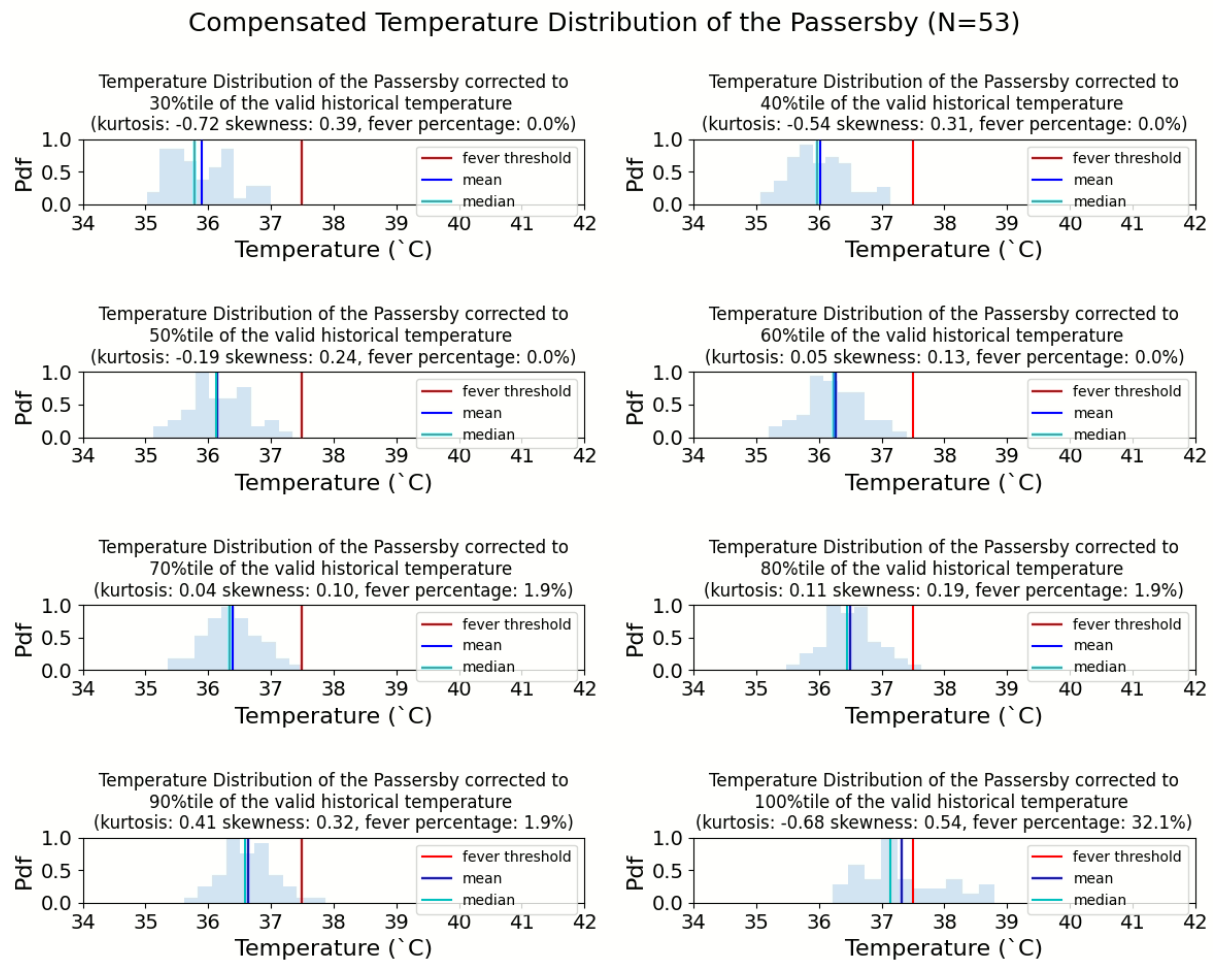


Figure 5-3: The effects of percentile of the valid historical temperature distribution chosen for temperature estimation.

Figure 5-4 shows the analysis of the percentile chosen for the temperature estimation with the valid historical temperatures. Figure 5-4a, b, and c show the kurtosis and skewness of the temperature distribution of the 53 subjects, the percentage of passersby having fever, and the mean and median temperatures of the 53 subjects, respectively. Ideally, the kurtosis and skewness should close to zero as the temperature distribution should be a normal distribution when the number of subjects is large (by central limit theorem). Next, the fever percentage among the population should be close to zero as there should be less or no fever suspect passing through the north gate of HKUST. Last but not least, the mean temperature of the subjects should be close to 36.5°C, as shown in the data in study one. As a result, 70%-tile is

chosen for this dataset and consequent study as it is the best option to match the three mentioned criteria.

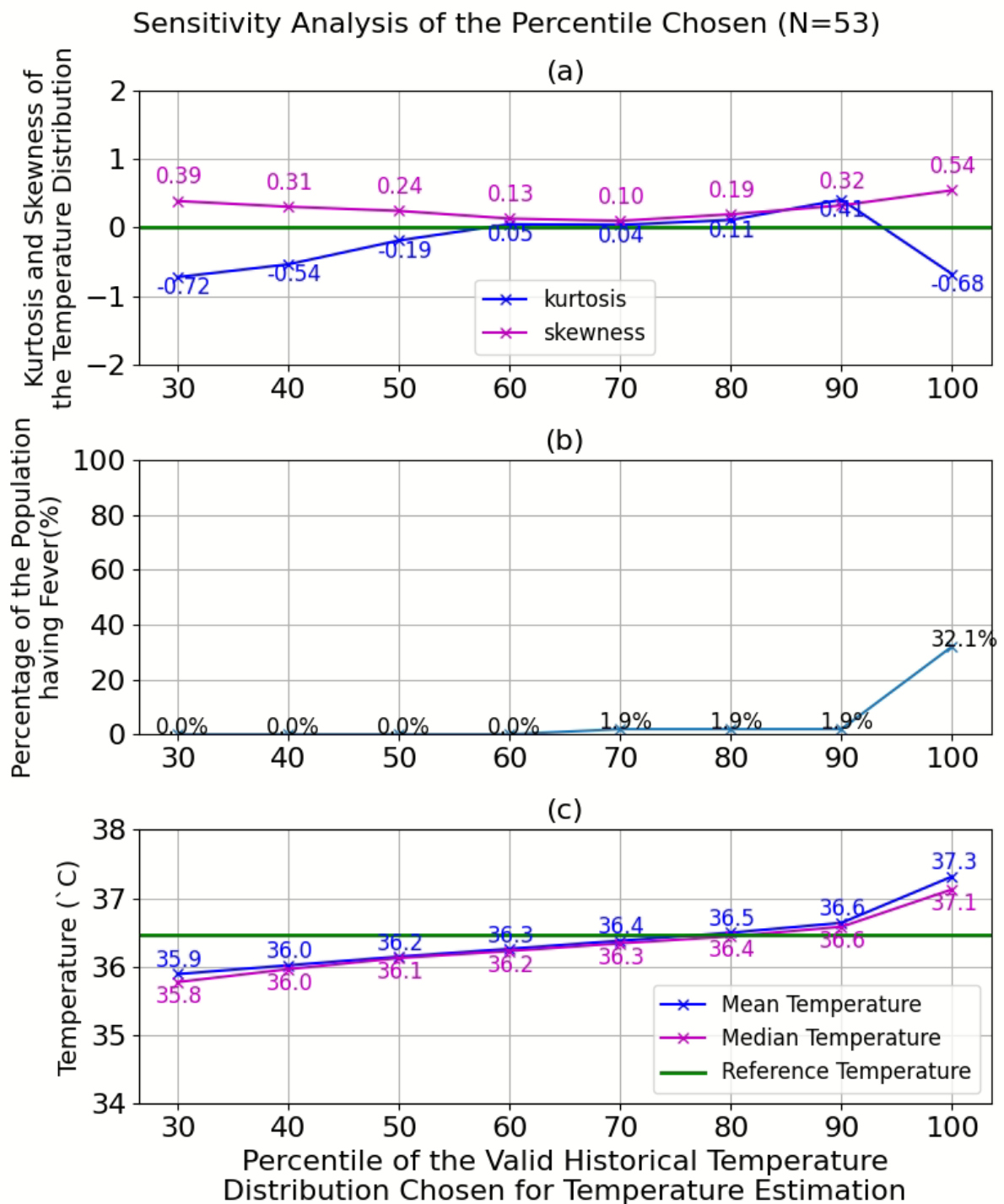


Figure 5-4: The analysis of the percentile of the valid historical temperature distribution chosen for temperature estimation. (a) The kurtosis and skewness of the temperature distribution of 53 subjects with different percentile chosen. (b) The percentage of the passersby having fever. (c) The mean and median temperature of the passersby.

5.3.2 Improvement of Temperature Estimation of each Individual with Thermal Compensation Model and Human Tracking

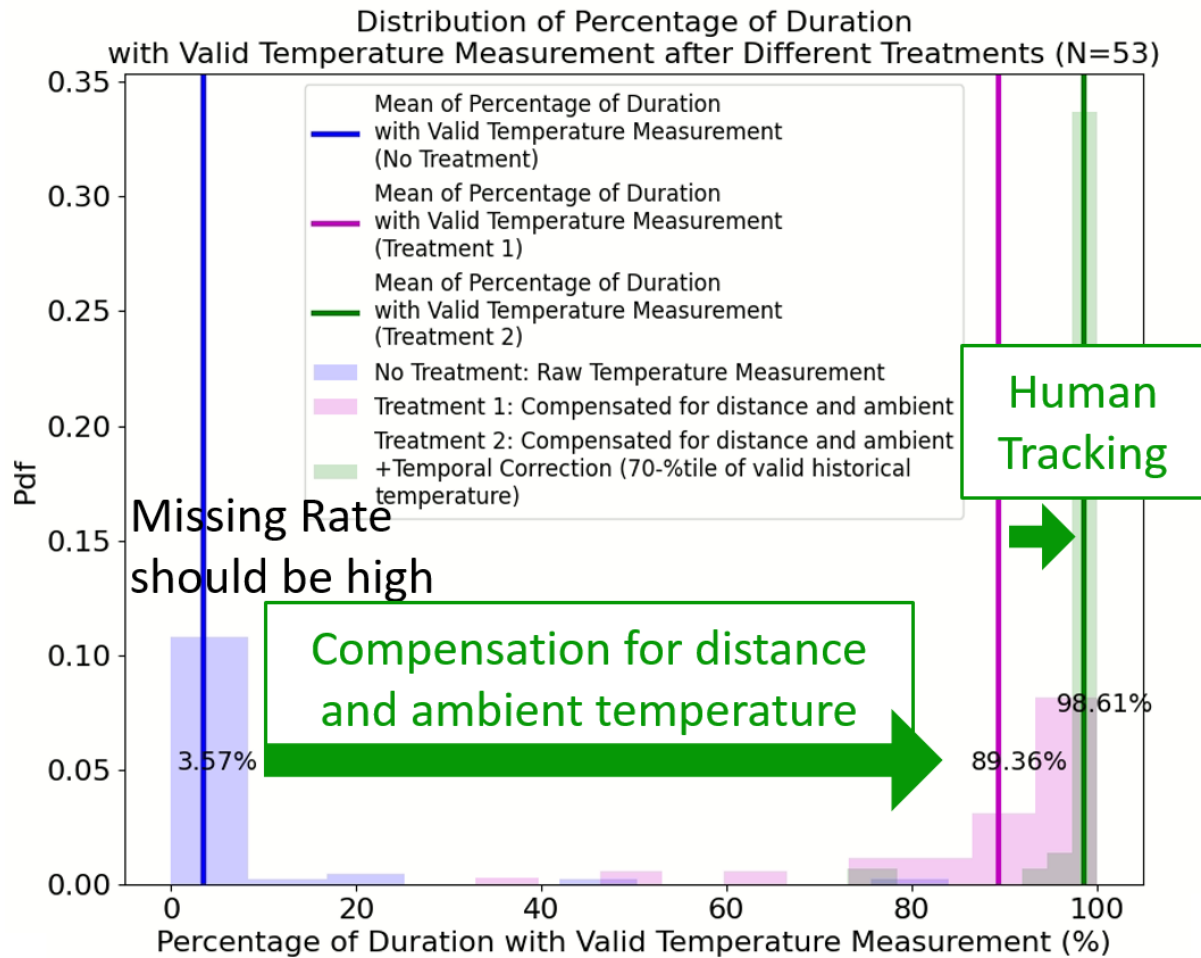


Figure 5-5: The mean and distribution of the percentage of duration with valid temperature measurement. There is a low percentage of duration with valid temperature measurement before any treatment on the raw measured temperature. The percentage of duration increases to 89.36% with treatment 1 (applied our thermal compensation) and further increases to 98.61% with treatment 2 (applied our thermal compensation and human tracking).

Figure 5-5 shows that the percentage of duration with valid temperature measurement is low at 3.57%. The low percentage of duration in the raw temperature measurement implies a high missing rate in fever screening. It increases from 3.57% to 89.36% with our thermal compensation (treatment 1) and further increases significantly to 98.61% with the combination of our thermal compensation and the human tracking (treatment 2) [F (2, 156)]>1083, $p < 0.001$]. This result suggests that our proposed thermal compensation model decreases the potential missing cases. Furthermore, data shows that our thermal compensation and human tracking combination successfully suppress the noise in non-

invasive temperature measurements. We hypothesize that the false alarm rate can be suppressed with human tracking, but this can be validated in future work.

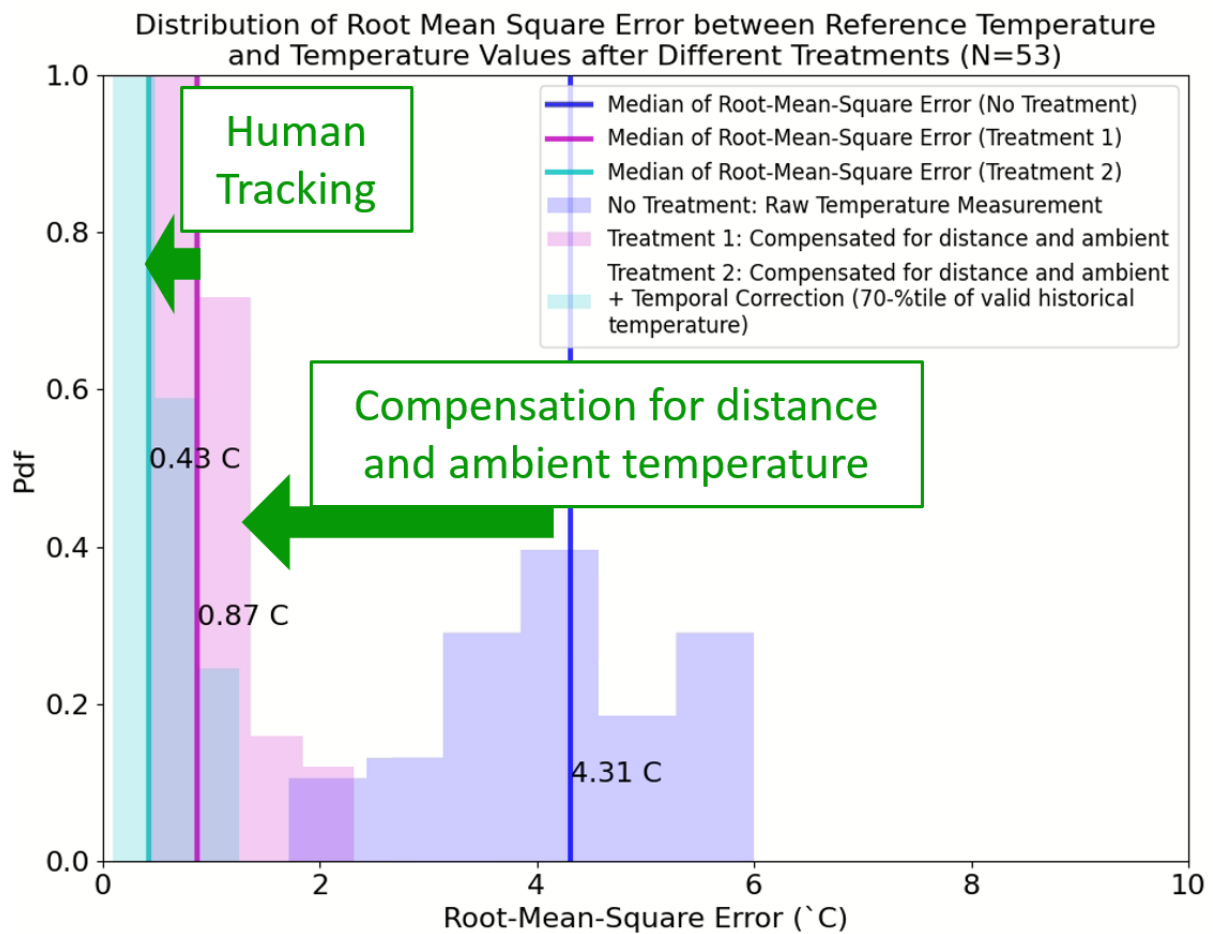


Figure 5-6: Comparing with no treatment, root-mean-square error (RMSE) decreases with treatment 1 and further decreases with treatment 2. Results show that our thermal compensation and the human tracking improve the accuracy of non-invasive temperature measurement.

Figure 5-6 shows the distribution of the RMSE of the reference temperature against three types of temperature values: raw temperature measurements (no treatment), compensated temperatures for distance and ambient temperature with our thermal compensation (treatment 1), and the combination of our compensation and human tracking (treatment 2). The reference temperature is the forehead temperature of the normal people in study one with a mean of 36.5°C and an S.D. of 0.1°C. Results show that RMSE decreases significantly from 4.31°C to 0.87°C with treatment 1 and further decreases significantly to 0.43°C with treatment 2 [$F(2,156)] > 474$, $p < 0.001$]. As a result, the finding suggests a promising direction of human subject tracking to suppress the noise in non-invasive temperature measurements.

5.4 Discussion and Conclusion

This chapter studies the possibility of tracking to reduce noise in temperature measurement for each of the individuals. We found that 3.56% of the time, on average, the temperature measurement values are within an average of human temperatures. Furthermore, the RMSE of the raw temperature measurements against the reference forehead temperature of the normal persons is 4.31 °C. This data demonstrates that non-invasive temperature measurement in practice does suffer much noise due to many uncontrollable factors.

The duration of having valid temperature increase to 89.36%, and the RMSE decreases to 0.87 °C with our thermal compensation for distance and ambient temperature. In addition, the duration of having valid temperature further and the RMSE further improve to 98.61% and 0.43 °C, respectively. Our study shows that temporal information by human tracking suppresses the noise in non-invasive temperature measurements. We hypothesize that the false alarm rate for fever screening can be suppressed by utilizing human tracking, but this can be validated in future work.

This is the beginning of noise suppression in non-invasive temperature measurements using information from human tracking. Future researches can explore the potential of human tracking in noise suppression for fever screening applications.

Chapter 6 STUDY FOUR: ONLINE DECISION ANALYTICS SYSTEM: LIVE-STREAMING AI FEVER SCREENING SYSTEM

Summary

This chapter details the design and deployment of an online decision analytics system on non-invasive fever screening. The emphasis is on real-life implementation and site trials rather than laboratory experiments.

6.1 Introduction

Fever is one of the most apparent symptoms of infections, for example, severe acute respiratory syndrome (SARS), influenza, and Ebola. Since the global SARS outbreak in 2003, fever-screening systems have been set up at many national borders as the first line of defense to protect the health of residents. For example, the conventional Thermal Imaging Systems (TIS) have been installed at multiple border control points in Hong Kong for fever screening purposes. However, this setup requires human operators from the Department of Health of the HKSAR government to perform intensive manual checking by gazing between color images and thermal images to identify potentially infected persons for further investigation. In addition, the operators need to stop the suspects before they walk away. This task imposes time pressure and can increase human errors that will go undetected.

We propose an online decision analytics system on non-invasive fever screening that minimizes the work stress of human operators and therefore reduces human errors. The system consists of an automated fever suspect detection with artificial intelligence (AI) and a virtual floor plan technology. It can ease the detection of fever suspects over a large area. The design and deployment of the online decision analytics system are detailed in this chapter.

6.2 Data and Design Requirements

In this section, input data and modeling processes are described. We also summarize the design requirements for the system.

6.2.1 Data Description

The input data mainly consists of two kinds of video data. The first one is a high resolution (3840 x 2160) color video stream at 30 frames per second (fps), and the second one is a lower resolution (320 x 240) raw temperature stream at 30 fps. The purpose of these two video streams is for non-invasive temperature measurement and photo capturing of fever suspects.

The output results are the following:

- Location of the people on a 2D floor plan.
- Status of the person (normal or fever).
- Photo of the face and photo of an entire body.

6.2.2 Design Requirements

We worked closely with the Department of Health in Hong Kong (DH) and the Electrical and Mechanical Services Department in Hong Kong (EMSD) during the entire project. As a result, many iterations of designing, developing, refining, and site-testing the system gradually improved our system. The primary requirements are as follows:

- a) Automatic detection of the fever suspects.
- b) Stable tracking and localization of the fever suspects across cameras.
- c) Suppression of false alarm from hot objects.
- d) System running in real-time at 10fps or above.

6.3 System Architecture and Design

In order to support temperature screening of high human traffic in broad spaces, especially at border control points, multiple color and thermal cameras are required to capture everyone going through the checkpoints. The hardware configurations and software designs are described as follows.

6.3.1 Hardware

The hardware of the proposed system includes two GPU server (2 x Intel® Xeon® Gold 6136 Processor 24.75M Cache, 3.00 GHz, 6 x NVIDIA (INNO3D) GeForce RTX 2080Ti Jet, 256GB RAM), two 24-port Cisco Power-over-Ethernet (PoE) LAN Switch, a Wi-Fi router, four sets of Thermal Units (TU), two Scene Camera (12MP Hikvision Smart Network Box Camera) [Appendix 6.1, page 113]. Each thermal unit consists of an 8MP Hikvision Smart Network Box Camera and a FLIR A315 Thermal infrared camera. The hardware connection diagram is shown in Figure 6-1.

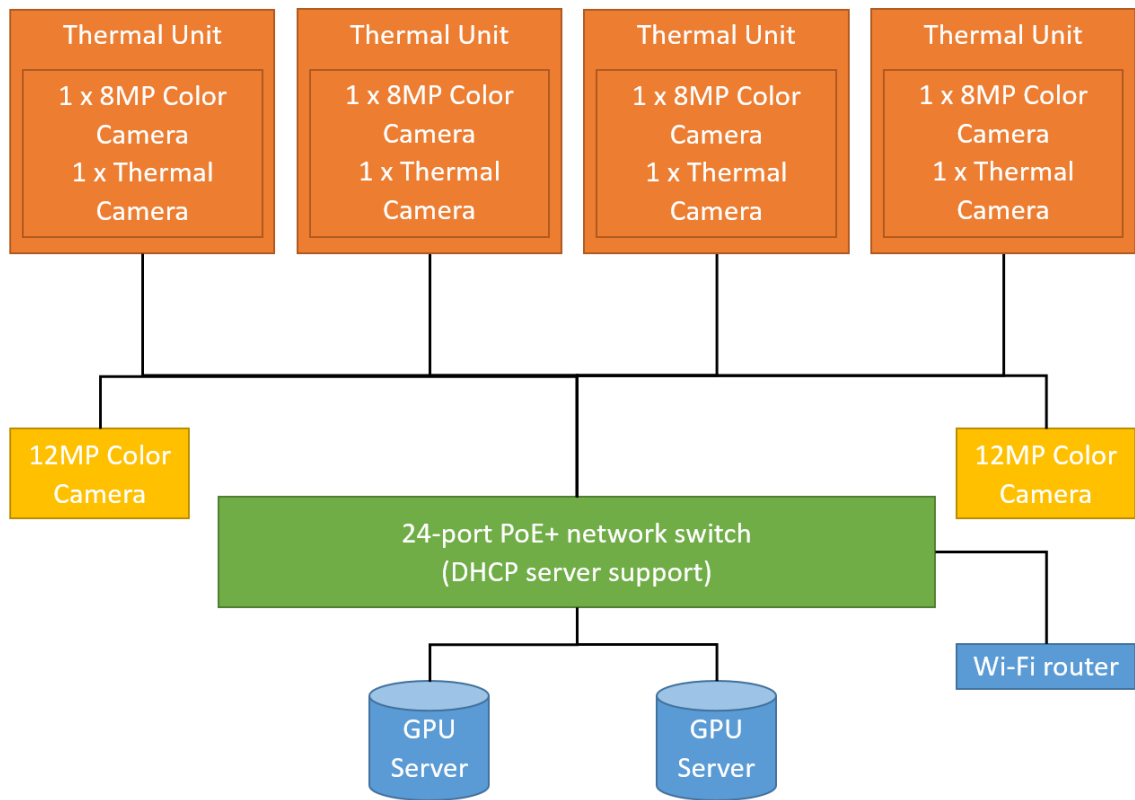


Figure 6-1: Hardware Connection Diagram

6.3.2 Software

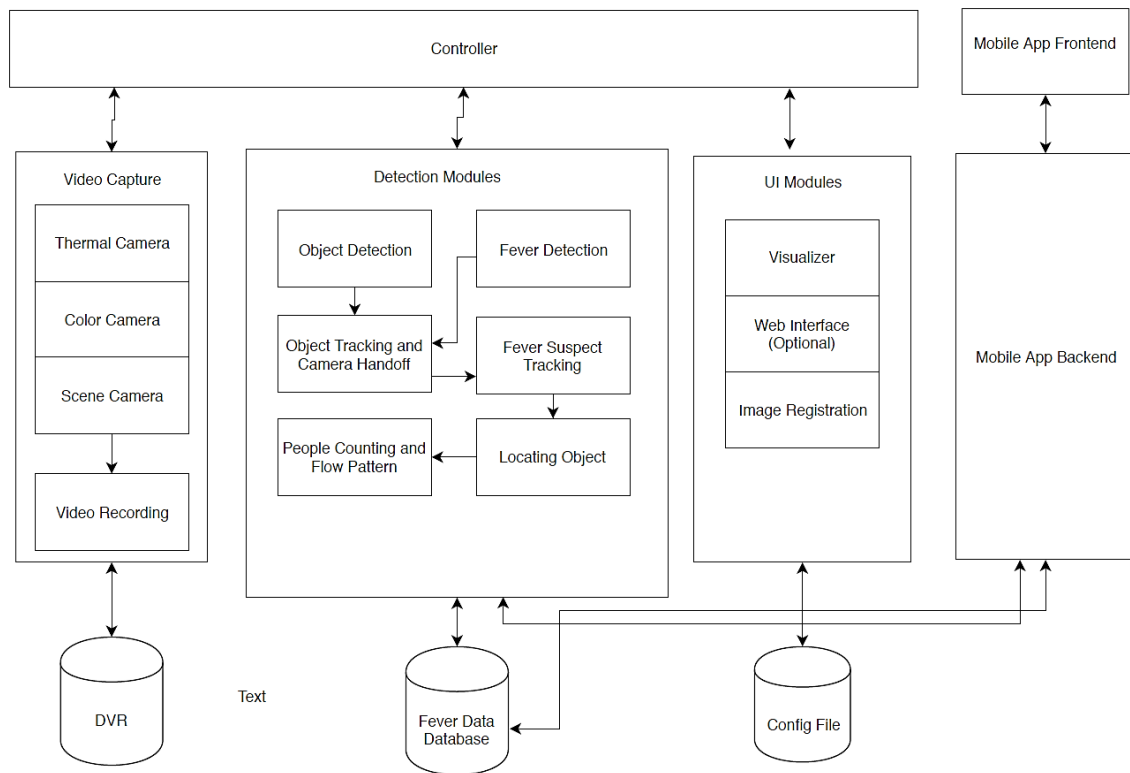


Figure 6-2: Software Architecture of Smart Fever Screening System (SFSS)

The software architecture is shown in Figure 6-2. There are one controller and four modules: a video capture module, a detection module, a user interface (UI) module, and a mobile app backend module. The controller is responsible for the inputs and outputs (I/O) and data passing within the system. The first module is the video capture module. Video stream from the cameras is being captured, recorded, and passed to the controller for further processing. The software stack (software libraries used) is shown in Figure 6-3.

All of the thermal units and scene cameras are connected to the two GPU servers via the network switches. One of the GPU servers is called the *master server*, and the other is called the *slave server*. Each of the servers is responsible for processing the video streams from 2 thermal units and 1 scene camera. In addition to the video processing, the *master server* is also responsible for integrating the location information (dots) of the detected people from all the cameras onto a single floor plan. Finally, the location (on the floor plan) and photos of the fever suspects are sent to a tablet PC or web application for visualization.

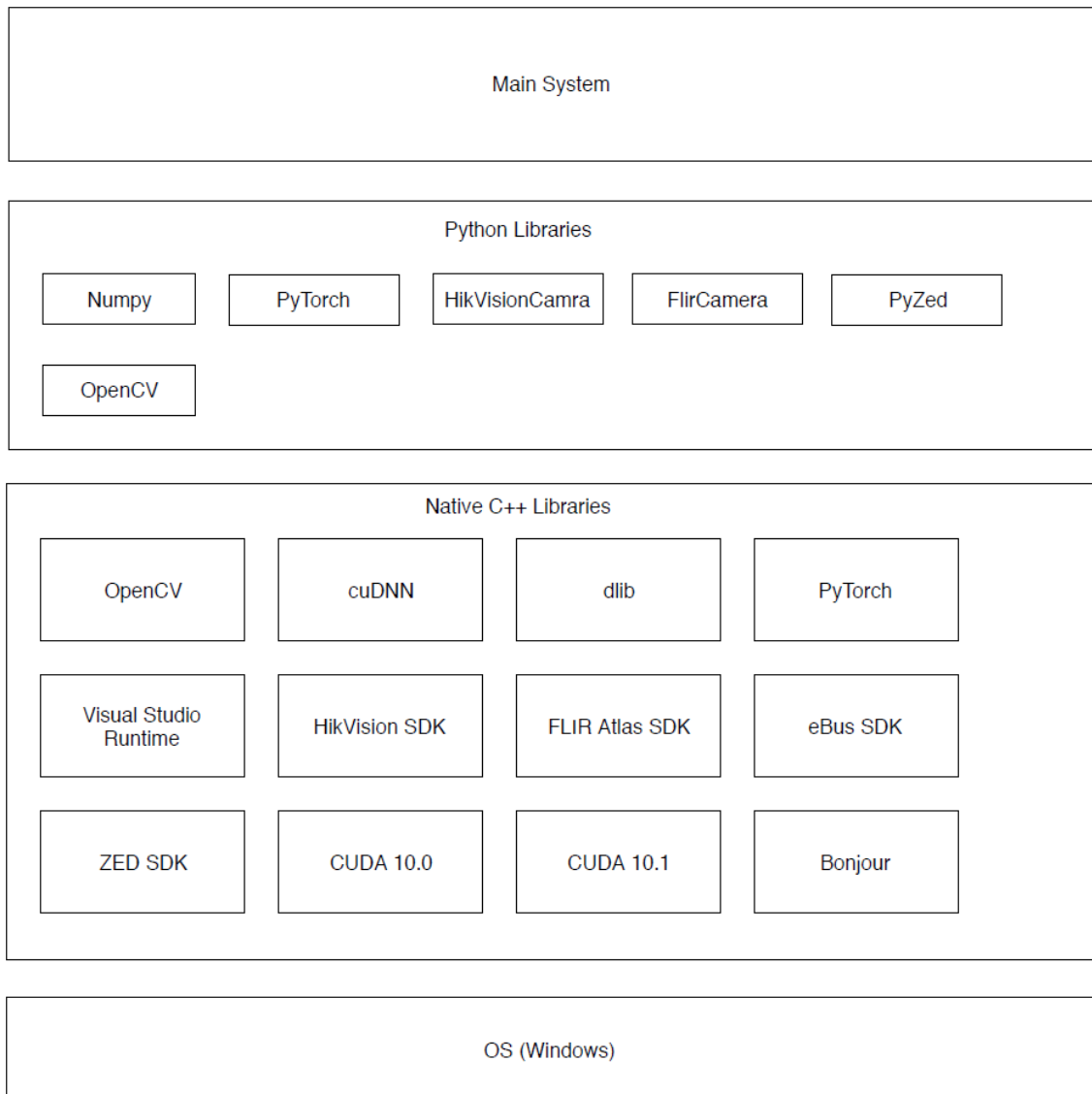


Figure 6-3: Software Stack of SFSS

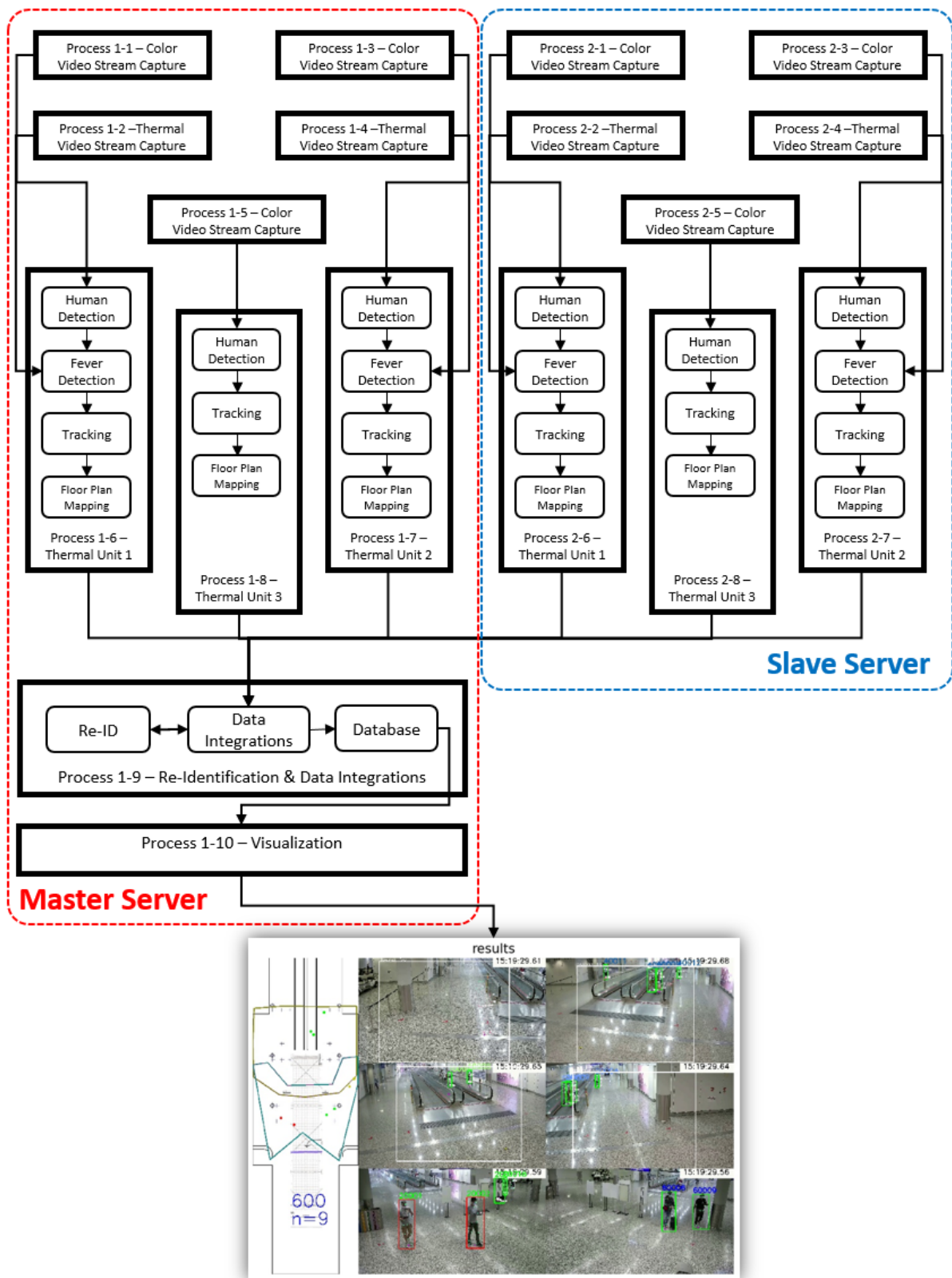


Figure 6-4: System Diagram

Figure 6-4 shows the basic system diagram of the Smart Fever Screening System (SFSS). First, the system receives multiple video streams as data input; in this case, 4 x 4K color video

streams from 8MP color cameras, 4 x low-resolution raw temperature streams from thermal cameras, and 2 x DCI 4K color video streams from 12MP color cameras. After that, a human detection algorithm is run on each color video stream to extract the human key-points information. Thirdly, the thermal video streams are used for fever detection, and the photos of the fever suspects will be taken for visualization. Next, the location of the persons on the 2D floor plan is being calculated. Then, the information will be sent for integration before visualizing it in the UI.

The following section details each of the modules and the overall structure of the systems.

I. Parallel Architecture

Figure 6-4 shows ten processes and nine processes in the master GPU server and slave GPU server, respectively. There are five processes for each of the resources-hungry video stream capturing in each GPU server (3 for 4k color video streams, 2 for thermal video streams). Since there are three “thermal units” (TU) in each GPU server, three main separate processes are needed for each of the TUs to power the computational intensive Open-Pose algorithm for human detection, face box prediction, and feet prediction. Within each of the three processes, multi-threads were used to share CPU time for fever detection, tracking, and floor plan mapping.

The results of the three main processes will be sent to the 9th process in the master GPU server for person re-identification from different camera sets and for data integrations to remove duplicated information. Finally, the results will be sent to *Visualization Process* for further processing before visualizing it on the web application or the mobile APP.

II. Video Capture

Each of the video streams from connected cameras is streamed to the video capturing module. Then, the decoding of the video streams is done to obtain the raw images for further processing in other modules. The decoded images are also recorded and stored in the server for our further analysis. However, the recording function is optional and can be disabled for privacy concerns.

III. Fever Suspect Detection

a. Human and Face Detection

Many face detection algorithms work well when human faces appear more prominent in the image, and some can work even when the human faces are small in the image (further away from the camera). However, the performance drops when occlusion happens. Therefore, pure face detection algorithms might not be the best solution for applications like fever screening in a moving crowd where occlusion happens frequently. Human detection with object detectors like [14], [15], [61], [62] can detect humans or faces, but separate depth information of feet detector is required to determine the location of the persons on the floor plan. Alternatively, face prediction with pose estimation algorithms can better tackle the occlusion problem. The reason is that the algorithms detect the key points on the faces and utilize the information from the entire human body. Open-Pose [31] was chosen for human detection. It provides enough information to estimate the location of the face (coordinates of the face boxes) and the location of the feet for each individual in real-time. The output of the Open-Pose is 25 key points. The face box can be predicted using the key points of eyes, ears, nose, neck and, shoulders.

b. Fever Suspect Identification

The color images were spatially registered to the thermal images using the homography transformation [51]. The location of the face box in thermal images can be calculated using the formula described in [51] and the coordinates of the face box in the color images. Temperature information within the face boxes in the thermal image can be acquired to estimate each individual's temperature value. If the temperature value is higher than 35.5°C (recommended and used by the Hong Kong Department of Health), the detected person will be classified as a fever suspect.

IV. Fever Suspect Tracking

Each person will be given an ID internally to keep track of the critical information. The tracking of the fever suspects is required to be accurate so that the staff in the Department of Health (DH) can successfully capture the fever suspects with the information provided by our system before the fever suspects leave the temperature screening station. Inspired by quick and straightforward tracking-by-detection

trackers [33], we customized a fever priority proximity tracker to track the fever suspects.

The procedures are as follows:

- a. The detected persons in each frame are being separated into two groups for tracking: the normal group (people with green ID) and the fever group (people with red ID).
- b. The priority for associating is given to the fever group, and the red ID is being associated with the spatially closest red ID in the previous frame.
- c. The remaining red ID in the previous frame without matches will be associated with the closest green IDs in the current frame.
- d. The green ID in the current frame is associated with the closest green ID in the previous frame.
- e. Data association in the current frame is done.

V. Floor Plan Mapping

The localization of the detected persons on the 2D floor plan is based on the feet and homography transformation [51]. The calculation can be expressed as follows:

$$p_{x,y} = \mathbf{H}_{ImgReg} * p_{u,v}$$

$p_{u,v}$ denotes the feet coordinates of a person on the color image, $p_{x,y}$ denotes the coordinates of the person on the 2D floor plan. \mathbf{H}_{ImgReg} is a 3 x 3 matrix with eight degrees of freedom. Four pairs of correspondence points are sufficient to solve for the \mathbf{H}_{ImgReg} . During the calibration, at least four pairs of correspondence points on the color image and 2D floor plan are given to the system to solve \mathbf{H}_{ImgReg} . It can be used directly during the system operation in real-time to calculate the location of the person on a 2D floor plan.

VI. Person Re-identification and data integrations

Person re-identification is a task to associate the same person from different cameras. Our system design consists of multiple color cameras to enlarge the tracking zone of the fever suspects. Therefore, the person re-identification and data integration module identifies the same person and eliminates the duplicated information. The structure of the deep learning model used for person re-identification (modified based on [50]) is shown in Figure 6-5.

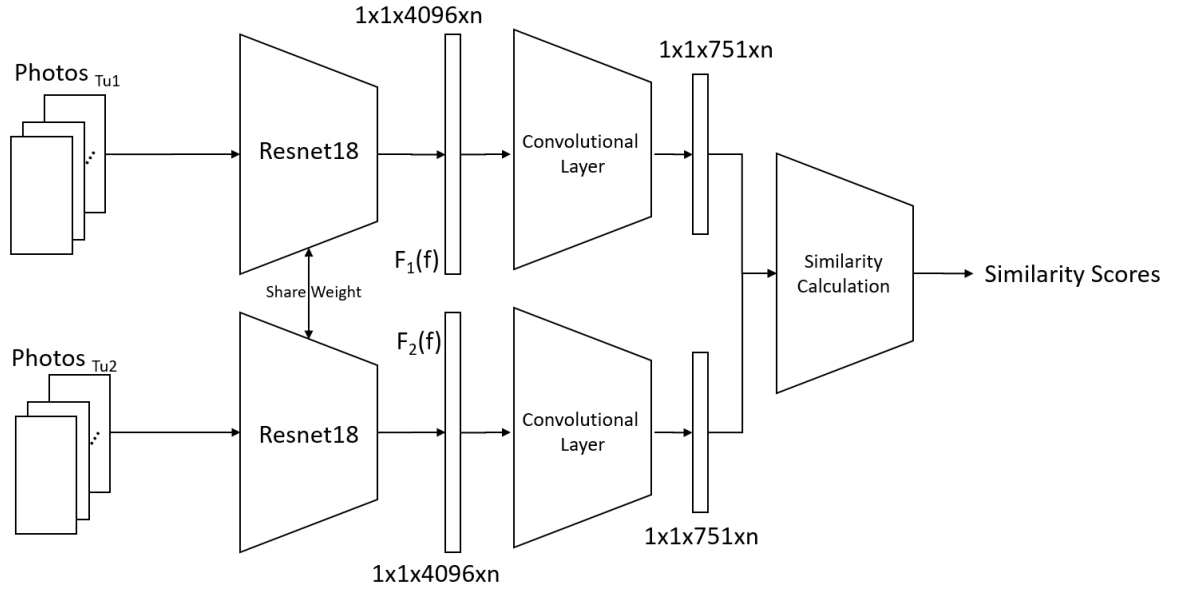


Figure 6-5: ReID Network Structure

The photos of each person in different cameras are captured and sent to the re-identification and data integration module in the master GPU server. Feature extraction is done on all the photos, and the similarity scores are calculated between photos. We retrained the backbone with Resnet18 to balance the accuracy and computational cost for the ReID module. The threshold for similarity score can be adjusted, and it is site-dependent. The typical threshold is around 0.85.

VII. Database

MongoDB database [63] is used to store the information of the passersby. Heat map, the people count, the location of the green dots, and critical suspect's information (like coordinates on the 2D floor plan, the ear temperatures, and photos) are stored. The example is shown in Figure 6-6.

meteor.heat_map_db

Documents

Aggregations

Schema

FILTER { field: 'value' }

ADD DATA

VIEW

```

_id: "20210210"
deviceId: "datacenter-meteor"
heatMap: "data:image/png;base64,iVBORw0KGgoAAAANSUHEUGAAA
siteId: null
timestampPost: 2021-02-10T15:59:20.718+00:00

_id: "20210211"
deviceId: "datacenter-meteor"
heatMap: "data:image/png;base64,iVBORw0KGgoAAAANSUHEUGAAA
siteId: null
timestampPost: 2021-02-11T04:19:49.423+00:00

_id: "20210218"
deviceId: "datacenter-meteor"
heatMap: "data:image/png;base64,iVBORw0KGgoAAAANSUHEUGAAA
siteId: null
timestampPost: 2021-02-18T04:14:20.201+00:00

```

meteor.people_counts_db

Documents

Aggregations

Schema

FILTER { field: 'value' }

ADD DATA

VIEW

```

_id: ObjectId("63c942708cdb414977858e5")
deviceId: "datacenter-meteor"
siteId: null
count: 0
timestampPost: 2021-02-10T13:33:31.094+00:00

_id: ObjectId("55bc7f4b16caaa1516238f0a")
deviceId: "datacenter-meteor"
siteId: null
count: 64
timestampPost: 2021-02-10T13:34:31.110+00:00

_id: ObjectId("dbec990f7f5939d3fb6abbb5")
deviceId: "datacenter-meteor"
siteId: null
count: 91
timestampPost: 2021-02-10T13:35:31.150+00:00

```

meteor.suspects_db

Documents

Aggregations

Schema

FILTER { field: 'value' }

ADD DATA

VIEW

```

_id: "6023fa32dc2412357812402c_12"
sessionId: ObjectId("6023fa32dc2412357812402c")
sid: "12"
fever: true
> coordinates: Object
> images: Array
> lock: Object
> close: false
> leftEarTemperature: Object
> rightEarTemperature: Object
> profile: Object
timestampOpen: 2021-02-10T15:35:16.630+00:00
timestampPost: 2021-02-10T15:35:24.313+00:00

_id: "6023fd345d606ff5879ffe48_3"
close: false
> coordinates: Object
fever: true
followup: ""
> images: Array
> leftEarTemperature: Object
> lock: Object
> profile: Object
> rightEarTemperature: Object
sid: "3"
timestampOpen: 2021-02-10T15:35:19.422+00:00
timestampPost: 2021-02-11T04:17:10.170+00:00

```

meteor.dots_db

Documents

Aggregations

Schema

FILTER { field: 'value' }

ADD DATA

VIEW

```

_id: 0
> greens: Array
> 0: Object
> 1: Object
> 2: Object
> 3: Object
> 4: Object
> 5: Object
> 6: Object
> 7: Object
> 8: Object
timestamp: 2021-02-11T04:18:19.355+00:00

```

Figure 6-6: Examples of data stored in database.

VIII. User Interface Module

The user interface (UI) module is responsible for processing the data in the database and send to either the mobile app or web application for visualization. The UI of our system is shown in Figure 6-7.

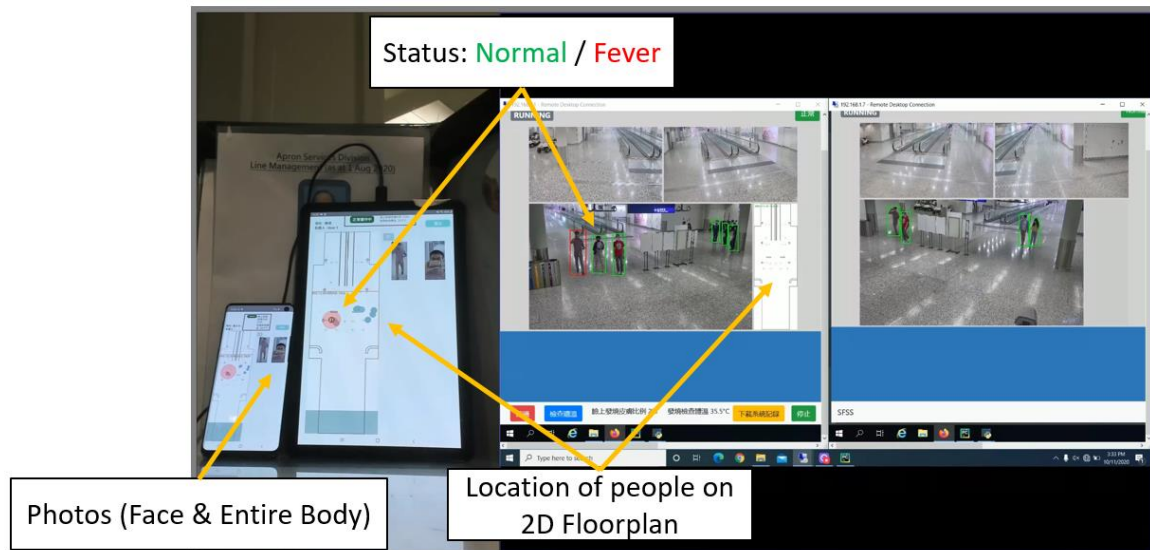


Figure 6-7: Example of user interface (UI) of our system. The left part of the photo shows the UI on the mobile phones and tablet PC, the right part of the photo shows the UI in the web application on the desktop PC or laptop.

6.4 Multi-person Loading Test and Mass Temperature Screening ($N \geq 40$)

We set up our system in HKUST for a multi-person loading test. Figure 6-8 demonstrates that our system can detect two fever suspects at different distances simultaneously among the crowd of more than forty people in real-time. Two persons were holding a thermal block [Appendix 6.2, page 114] at roughly 38.5°C to simulate the fever suspects. Processed images of two “thermal units” and one scene unit (without a thermal camera) are shown on the left, the location of the persons on the 2D floor plan is shown on the right. The results show that our system is promising for mass temperature screening. However, more testing in real sites is needed to verify the system performance in terms of the error rates under different crowd sizes.

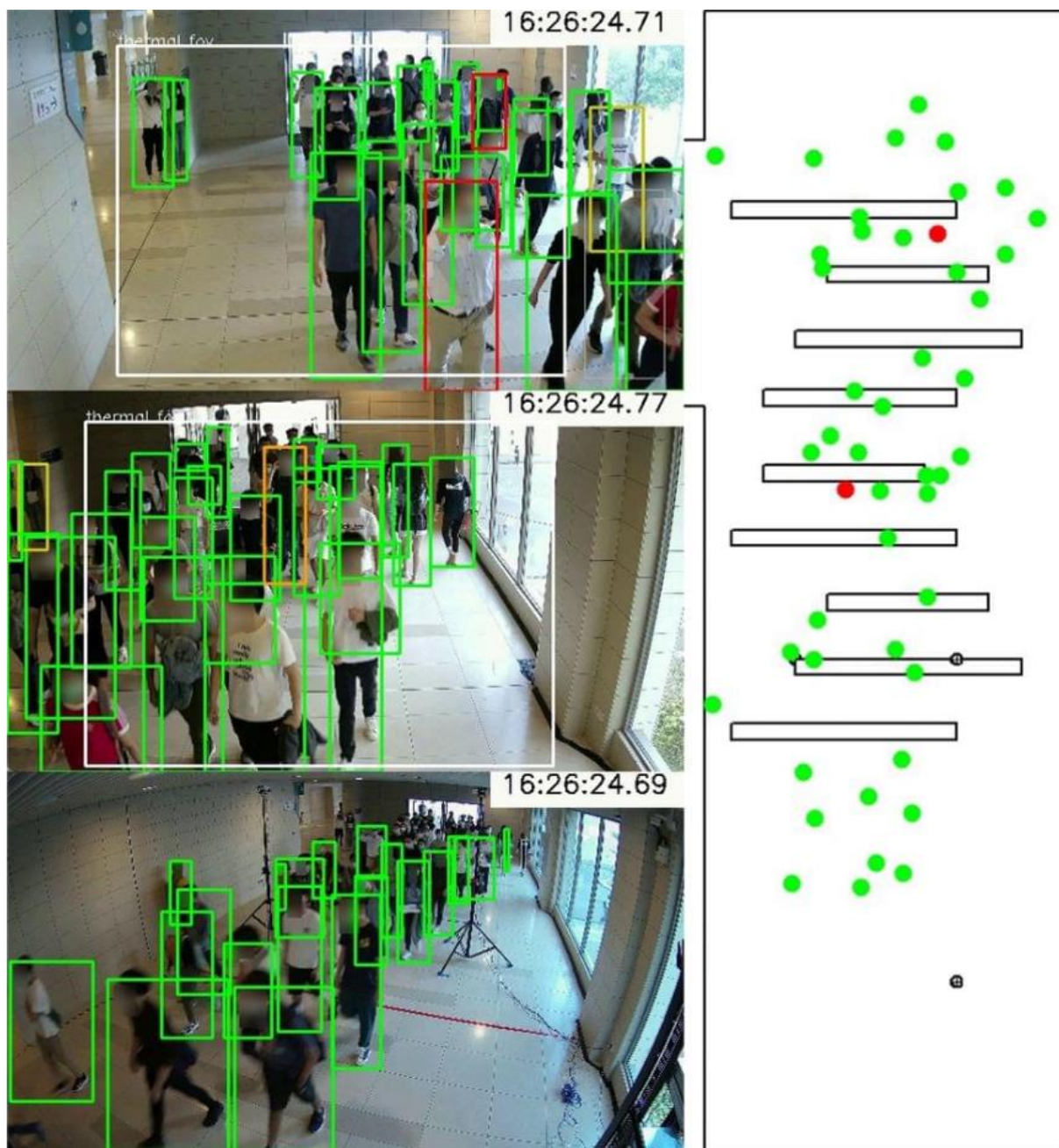


Figure 6-8: Mass temperature screening for moving crowds with our system ($N \geq 40$).

6.5 Role-play Simulation

Due to Covid-19, it is impractical to make an appointment with a team of staff from the Hong Kong Department of Health (DH) in a short time to trial and compare the conventional thermal imaging system (TIS) and our developed smart fever screening system (SFSS). However, a role-play simulation was designed to compare the two systems mainly on the response time, resources required, and features.

During the role-play simulation, the conventional TIS system and our smart fever screening system were set up side-by-side. The conventional TIS consists of a 4k color camera, a thermal camera, and three staff to perform the fever screening task. Three staff required to operate the conventional TIS. Two staff perform “eye-ball” checking for the identification of the fever suspects, and one staff catches the fever suspects. On the other hand, our SFSS consists of a thermal unit (a thermal camera and a 4k color camera), a scene camera, a personal computer (PC), a tablet PC, and a staff. The thermal camera and the 4k color camera used in the setup were a FLIR A315 and a Hikvision 8 MP Smart Network Box Camera. They were shared between the conventional TIS and our SFSS during the role-play simulation. Last but not least, three persons acted as passersby in front of the system, with one of them holding a heated thermal block (surface temperature of 38.5 °C) to simulate fever suspect. The role-play simulation setup is showed in Figure 6-9.

The procedures of the role-play simulation are the following:

- I. Three passersby walk from the door entrance towards the cameras, turn left and exit the temperature screening zone.
- II. During the walk, one of the passersby holds the heated thermal block up on the face near the forehead region to simulate a real fever suspect passing by.
- III. For the conventional TIS setup, the two staffs need to constantly perform “eye-ball” checking between color and thermal images and scrutinize the information to identify the fever suspect. Once the fever suspect is identified, they describe the appearance of the fever suspect to the third staff standing in the fever screening zone by walkie-talkie. After that, the third staff needs to search for the correct person among the three persons and catch the fever suspect before leaving the fever screening zone.
- IV. For the SFSS setup, a staff stands in the fever screening zone and holds the tablet PC connected to our SFSS. When a fever suspect is detected, the photo and the location information are sent to the tablet in real-time. The tablet PC will alarm the staff with beep sounds, and the staff will search and catch the fever suspect with the photo and location information shown on the tablet before he or she leaves the fever screening zone.

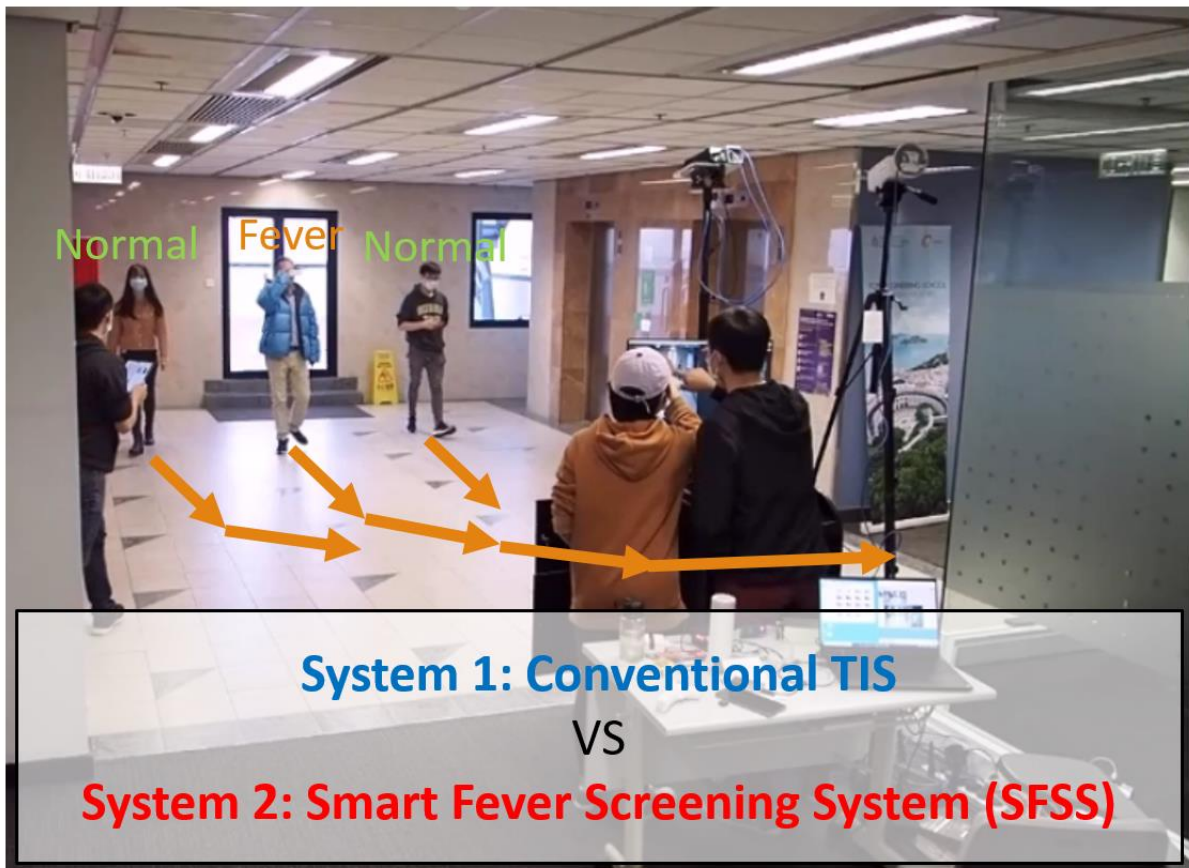


Figure 6-9: The setup for measuring the response time of the SFSS and the conventional TIS

6.6 Benchmark Results

Results of Response Time of conventional TIS versus SFSS

The role-play simulation was repeated nine times. In addition, the required time for identifying and successfully capturing the fever suspect for both of the systems was recorded.

Figure 6-10 shows the comparison of the response times between the two systems. For conventional TIS, the average response times to identify and capture the fever suspect are 6.41 seconds and 9.25 seconds, respectively. For our SFSS, the average response times are 1.86 seconds and 4.69 seconds. Thus, our system is 3.45x faster than conventional TIS on the fever suspect detection task and 1.97x faster in total response time from detection to capture the suspect successfully. The results are significant [$F(3, 32) = 89.9, p < 0.001$]. However, the average time between successfully identify and successfully capture the suspect is 2.840 seconds for the conventional TIS and 2.835 seconds for the SFSS setup. Thus, there is no significant difference between the two systems on time needed to capture the fever suspect once the suspect is identified.

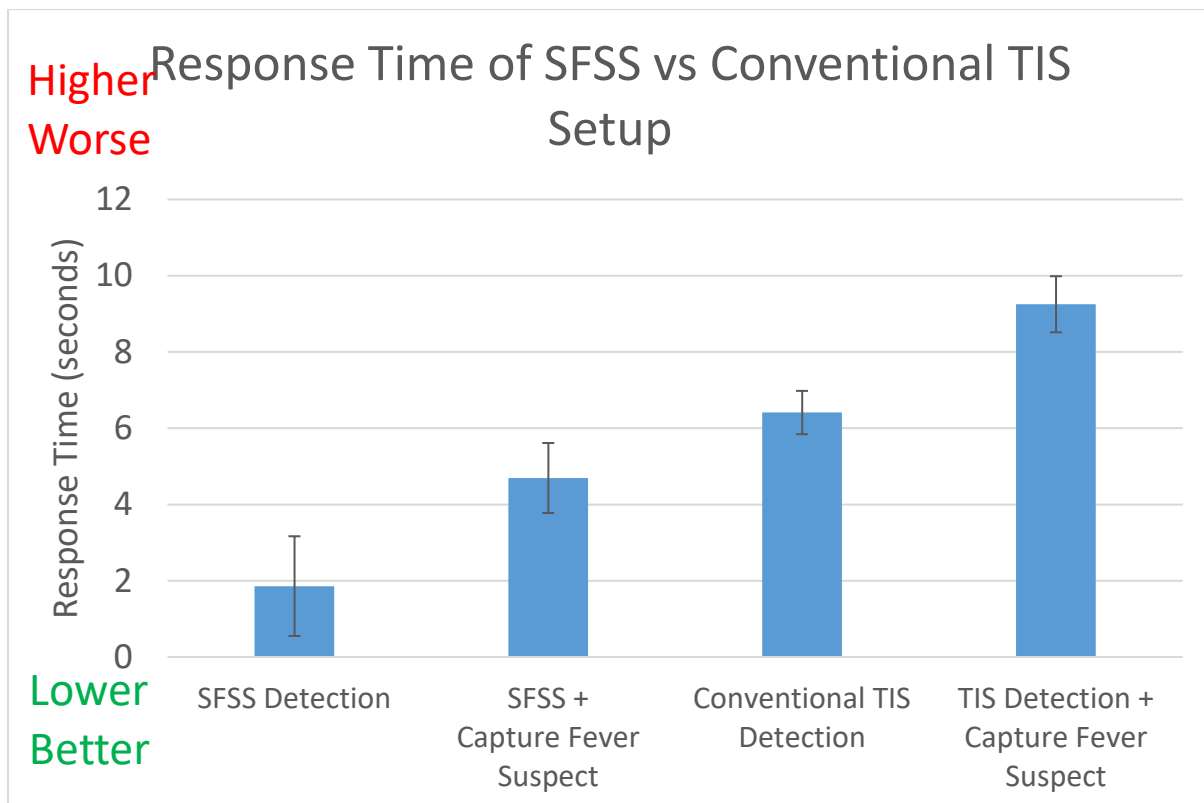


Figure 6-10: Our system detects fever suspects in a shorter time consistently

Nevertheless, our SFSS offers a shorter detection time and saves two operators on the same fever screening task under this simple setup for the role-play simulation. The result suggests that it will be beneficial if the system is installed at the border control points with much larger human traffics. It will be interesting to study and compare the conventional TIS and our SFSS with the Department of Health of the HKSAR government at one of the border control points.

6.7 Deployments of Live-Streaming AI Fever Screening System in the Public

The RFSS is one of our developed systems. The deployment of our systems has been site trialed and accepted by five schools, three libraries, one Non-Governmental Organization (NGO), one museum, nine elderly centers, the Electrical and Mechanical Services Department

(EMSD), and the Department of Health of the HKSAR Government. Figure 6-11 shows the locations of our deployed systems.

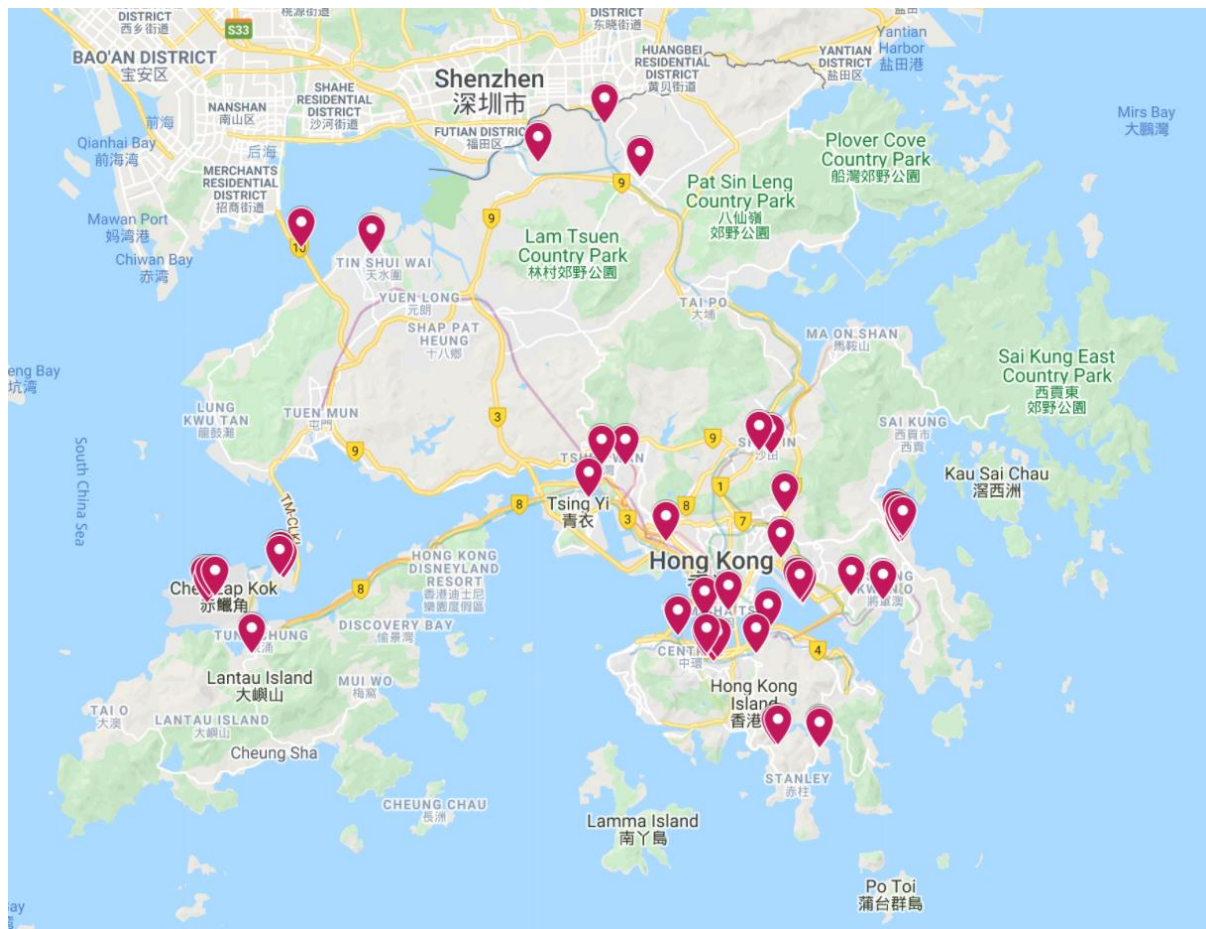


Figure 6-11: The locations of our deployed systems

6.7.1 Installation at Hong Kong International Airport



Figure 6-12: The Installations of the SFSS at the Hong Kong International Airport (HKIA)

6.7.2 Installation at Kai Tak Cruise Terminal



Figure 6-13: The Installation of the SFSS at the Kai Tak Cruise Terminal (KTCT)

6.7.3 Installation at Hong Kong International School (HKIS)

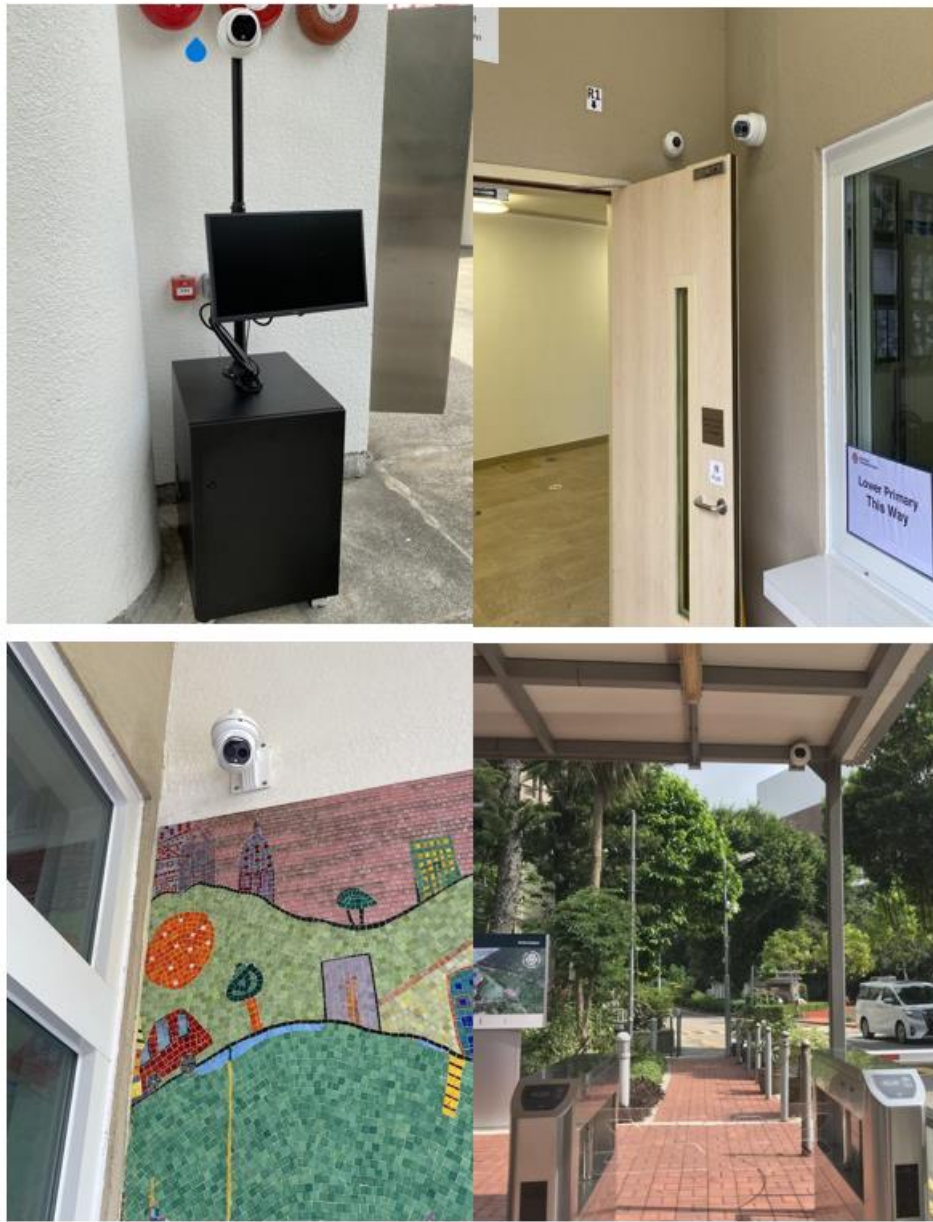


Figure 6-14: Our system at Hong Kong International School (HKIS)

6.7.4 Installation at four primary schools



Figure 6-15: The Salvation Army William Booth Secondary School, The Salvation Army Shek Wu School, The Salvation Army Lam Butt Chung Memorial School, The Salvation Army Tin Ka Ping School

6.7.5 Installation at five elderly day care centers

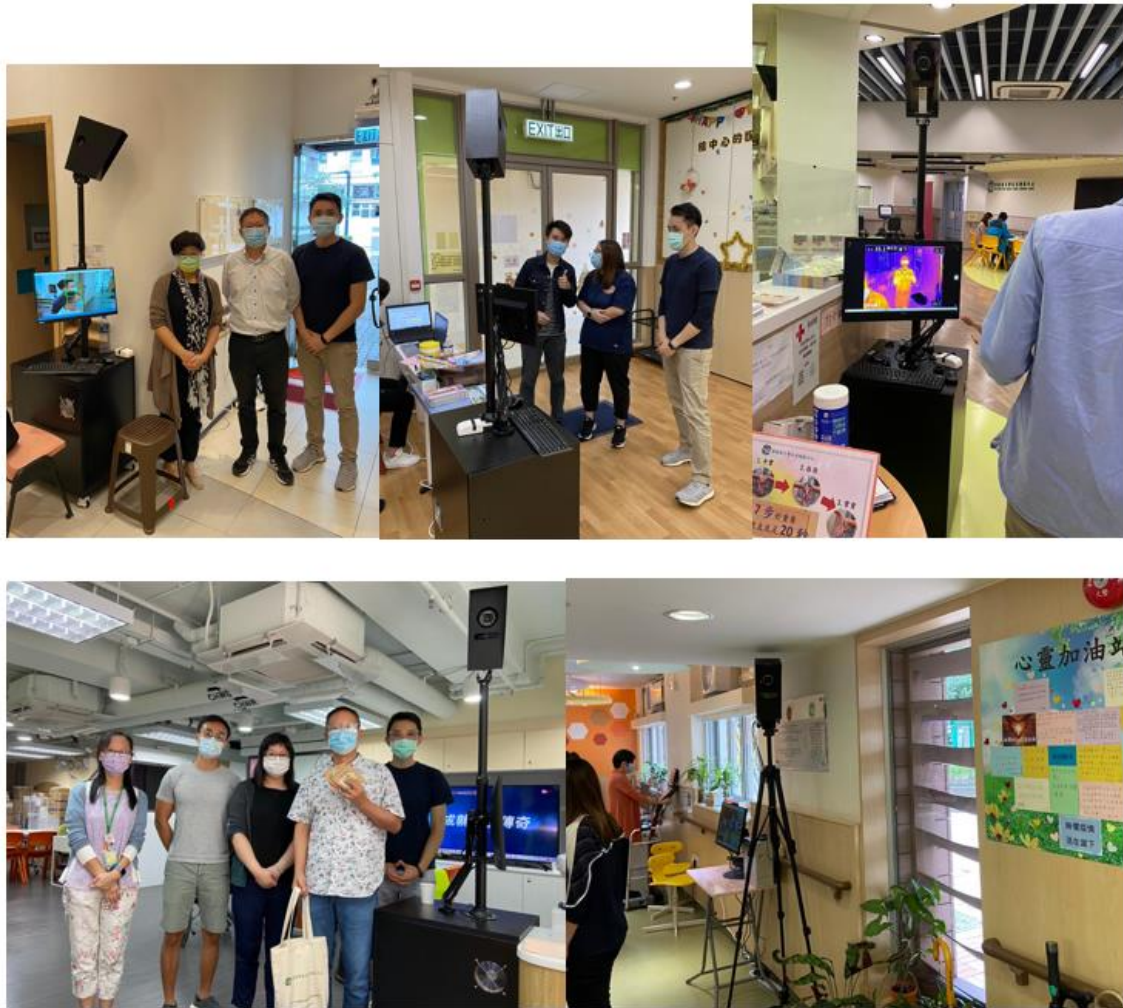


Figure 6-16: Five elderly daycare centers

6.7.6 Installation at two public libraries

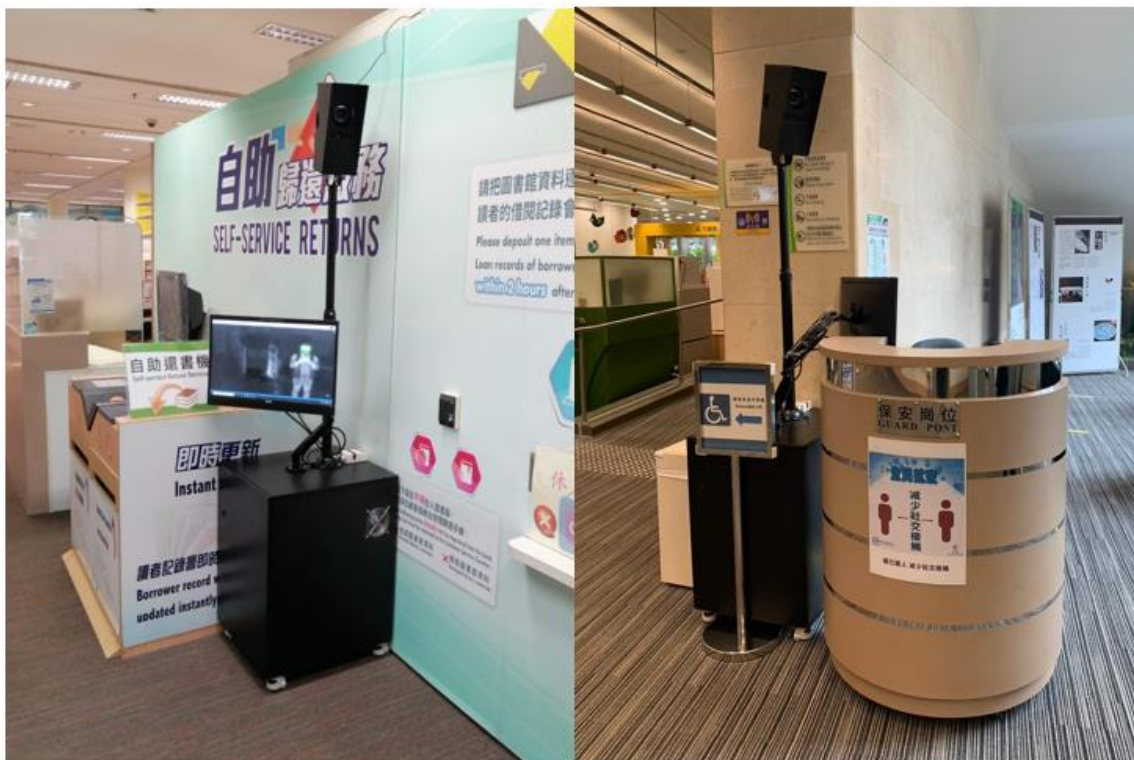


Figure 6-17: Tsing Yi Public Library and Tiu Keng Leng Public Library

6.7.7 Installation at the Science Museum



Figure 6-18: The installation of our system at the entrance of science museum

6.7.8 Installation at Seven Border Control Points and Major Government Offices



Figure 6-19: The installation at a government building and one of the border control points

6.7.9 Installation at HKUST

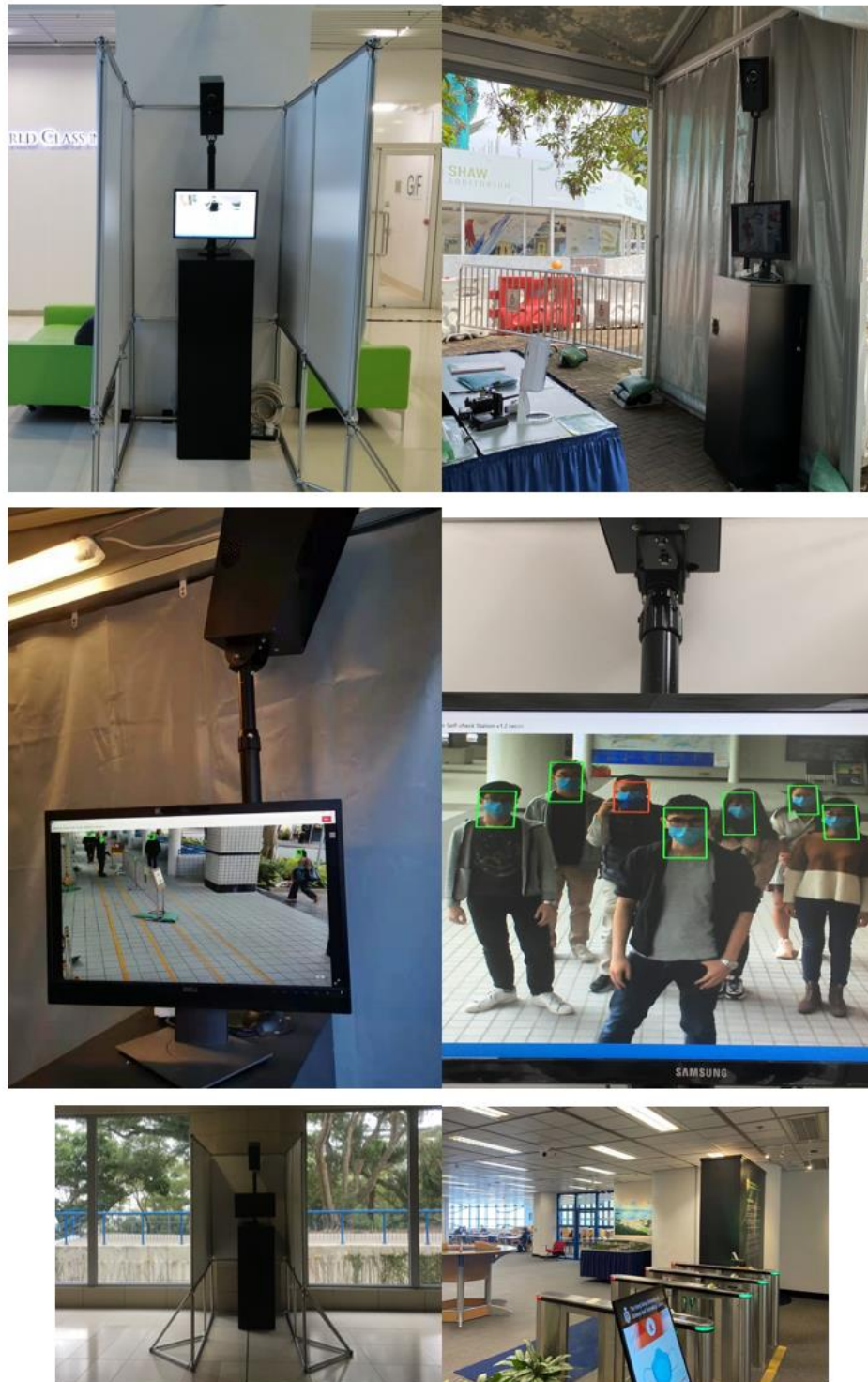


Figure 6-20: The installation at HKUST: Lee Shau Kee Business Building, South Gate, North Gate, Atrium, Cheng Yu Tung Building, and the HKUST Library

6.8 User Surveys and Feedbacks

We have collected the user feedback from eleven of the sixteen trial partners. Three of them are schools, and eight are either elderly centers or elderly homes. Figure 6-21 shows the survey results, and positive feedbacks have been received. All of them are satisfied with our technology and system. Our system brought benefits to their operation in terms of process enhancements. In addition, five out of the eight elder centers reported that our system also improves their service quality. Moreover, 73% of the users are willing to adopt our technology into their daily operations. The remaining users have concerns about the cost and aesthetics of our system. [Appendix 6.3, page 115]

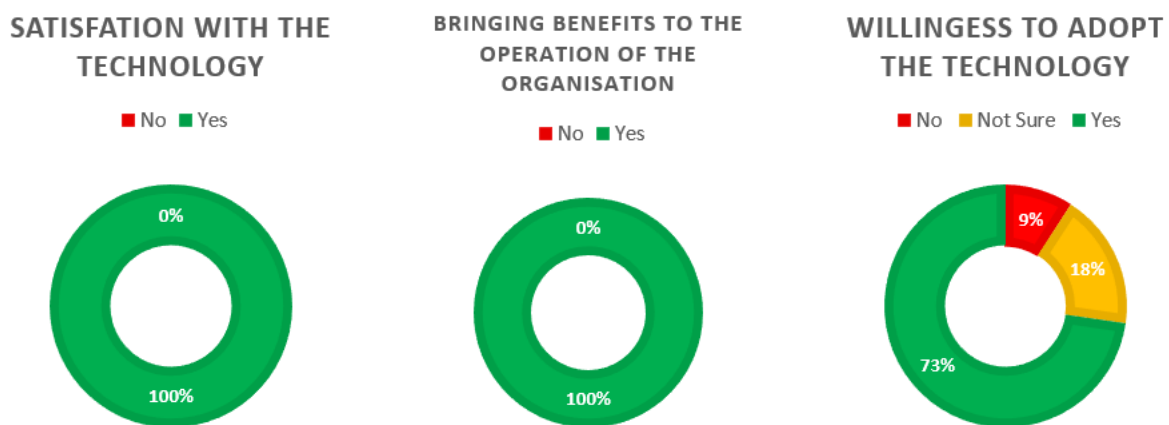


Figure 6-21: The survey results regarding to our technology and system.

6.9 Discussions and Conclusions

Challenges in the design, implementation and deployment of multiple AI in computer vision to create LAFSS to replace human decisions on non-invasive fever screening in moving crowds have been studied. The first part documented the design and implementation of the LAFSS, followed by testing and validating the proposed system. The second part provided details on the deployment of the RFSS at five schools, three libraries, one Non-Governmental Organization (NGO), one museum, nine elderly centers, the Electrical and Mechanical Services Department (EMSD), and Department of Health of HKSAR Government.

Due to Covid-19, the site trial at one of the border control points was canceled, and a role-play simulation to mimic fever screening at border control points was conducted at HKUST instead. Results show that the average response times to identify and capture the fever suspect using our system are 1.86 seconds and 4.69 seconds accordingly. Data shows 3.45x

and 1.97x faster than the conventional Thermal Imaging System (TIS) setup used at the border control points in Hong Kong for almost two decades. Furthermore, the number of staff required to operate our system decreased from three to one. The system is new and shows promising results for replacing human decisions on non-invasive fever screening in moving crowds.

Positive feedbacks have been received from the site trials partners of RFSS. The deployments of RFSS at various locations in Hong Kong created a positive impact on human society and helped our fight against the Coronavirus pandemic. In addition, the non-personal identifiable data collected (such as temperature, distance, ambient temperature) may also facilitate future research on non-invasive temperature measurement and screening applications.

Chapter 7 CONCLUSIONS, LIMITATIONS AND FUTURE WORKS

7.1 Conclusions

In this thesis, we studied the challenges of non-invasive fever screening for a moving crowd using AI technology in computer vision to assist or even replace humans in decision-making. We proposed, developed, and tested two thermal compensation models for non-invasive temperature measurements. The two models incorporate the statistical model of interacting effects of measuring distance and ambient temperature and the physics model of atmospheric absorption. Furthermore, we investigated the possibility of noise suppression in non-invasive temperature measurements. Our proposed model showed effectiveness in noise suppression with human tracking. In addition, we also proposed, developed, and site-trialed multiple versions of the live-streaming AI fever screening system (LAFSS). The deployments of our systems have been site-trialed and accepted by five schools, three libraries, one Non-Governmental Organization (NGO), one museum, nine elderly centers, the Electrical and Mechanical Services Department (EMSD), and the Department of Health of the HKSAR Government.

The influence of the measurement distance on non-invasive temperature measurement has been studied. The error of the temperature measurement by the thermal infrared camera increases linearly as the distance between the subject and the camera increased. The mean absolute error (MAE) and the root-mean-square error (RMSE) can be as large as 3.707°C and 3.875°C , respectively. Regardless of the errors in temperature measurements, separating the normal and febrile groups of people with a lower alarm threshold is still possible. However, the temperature screening is limited to a short range of distances up to 3.2m with this approach. On the contrary, the MAE and the RMSE were reduced to 0.474°C and 0.567°C with our proposed model and compensation, respectively. Thus, the distance for temperature screening increased to 8.2m. The improvements in screening distance can effectively increase the efficiency of temperature screening. These analyses are new and could not be found in the literature.

The influence of ambient temperature on non-invasive temperature measurement has been studied. We found that decreasing ambient temperature significantly reduces non-invasive temperature measurements linearly. Moreover, a drop in ambient temperature from 28°C to 14°C can reduce non-invasive temperature measurements by 4.1°C to 7.2°C on average. The

reduction of the non-invasive temperature measurements depends on the distance. Our data also show a significant interaction between distance and ambient temperature on the non-invasive temperature measurements. With our proposed enhanced thermal compensation model, the MAE and the RMSE drop from 4.799°C to 0.607°C and 5.158°C to 0.836°C, respectively. The results suggest that our thermal compensation model creates a possibility of fever screening with infrared thermography (IRT) in a semi-outdoor environment where the ambient temperature changes. A simulation study was conducted to study the fever screening in different ambient temperatures. Our simulation results show that it is impossible to detect fever with $\geq 90\%$ sensitivity and specificity with changing ambient temperature without any thermal compensation. This finding is consistent with ISO and FDA regulations, where fever screening systems work effectively only when the systems are used in the right environment or location. However, we enabled fever screening at different ambient temperatures and distances with our proposed model and compensation. This system is the first of its kind.

The possibility of tracking the same person and utilizing the temporal consistency of the body temperature to suppress temperature measurement noise introduced by other factors has been studied. We found that 3.56% of the time, on average, the temperature measurement values are within an average of human temperatures. Furthermore, the RMSE of the raw temperature measurements against the reference forehead temperature of the normal persons is 4.31°C. This data demonstrates that non-invasive temperature measurement in practice does suffer much noise due to many uncontrollable factors. However, the duration of having a valid temperature increase to 89.36%, and the RMSE decreases to 0.87°C with our thermal compensation for distance and ambient temperature. In addition, the duration of having a valid temperature further and the RMSE further improve to 98.61% and 0.43°C, respectively. Our study shows that using temporal information from human tracking suppresses the noise in non-invasive temperature measurements. We hypothesized that the false alarm rate for fever screening can be suppressed by utilizing human tracking, but this hypothesis can be validated in future work.

Finally, the challenges of design, implementation, and deployment of multiple AI in computer vision to create LAFSS to replace human decisions on non-invasive fever screening in moving crowds have been studied. We detailed the design and implementation of the LAFSS, followed

by testing and validating the proposed system. In addition, we detailed the deployments of our Remote Fever Screening System (RFSS) at five schools, three libraries, one Non-Governmental Organization (NGO), one museum, nine elderly centers, the Electrical and Mechanical Services Department (EMSD), and Department of Health of HKSAR Government. A role-play simulation of the fever screening operations at the border control points had been conducted at HKUST. Results show that the average response times to identify and capture the fever suspect using our system are 1.86 seconds and 4.69 seconds accordingly. Data shows 3.45x and 1.97x faster than the conventional Thermal Imaging System (TIS) setup used at the border control points in Hong Kong for almost two decades. Furthermore, the number of staff required to operate our system decreases from three to one. The system is new and shows promising results for replacing human decisions on non-invasive fever screening in moving crowds.

7.2 Limitations and Future Works

This thesis shows the start of integrating non-invasive temperature screening with infrared technology, deep learning technologies, and computer vision technologies.

In our study, only two of many factors for non-invasive temperature measurement with a thermal infrared camera have been studied. There are many other essential factors like humidity, time of day, head orientation, the emissivity of the skin, sweating effect, influences of the hardware, and more, which can introduce noise in temperature measurement. Thus, there are still many unknowns for non-invasive temperature measurement, especially under uncontrolled environments and at longer distances. There are rooms for future studies to investigate those factors and further improve the accuracy and robustness of non-invasive temperature measurements.

A simulation was conducted to study fever screening in different ambient temperatures. The results show that our thermal compensation model is promising for temperature screening in a semi-outdoor environment. However, the actual data of heated forehead in different conditions is missing. Therefore, the data of heated forehead in different conditions, especially in different ambient temperatures, can be collected to validate the simulation results. Furthermore, an experiment can be conducted to study and validate if human tracking can suppress the false alarm rate for fever screening.

The evolution of AI and deep learning technologies enable our LAFSS to apply our thermal compensation algorithm only on the thermal pixels that belong to humans in real-time. We conducted a multi-person loading test with our system, but the testing and validation of the system in real sites remain an open challenge. Moreover, there are still many deficiencies in the current technology. For example, there are false alarms introduced by the hot background, miss detection because of occlusion of the faces, and more. Another possible direction for future work on non-invasive temperature screening technology can be on the algorithms that can improve the accuracy and robustness of non-invasive temperature screening with infrared thermography (IRT). For example, segmenting the person's skin in low-resolution thermal images for hot background suppression, occlusion detection in the faces to alarm the users, human or face detection in thermal images are also possible future work. Last but not least, more efficient deep learning AI technologies that can run on cheaper GPU-enabled edge devices in real-time are also promising directions for future work.

REFERENCE

- [1] M.-F. Chiang *et al.*, “Mass screening of suspected febrile patients with remote-sensing infrared thermography: alarm temperature and optimal distance,” *J. Formos. Med. Assoc.*, vol. 107, no. 12, pp. 937–944, 2008.
- [2] E. Y. K. Ng, G. J. L. Kawb, and W. M. Chang, “Analysis of IR thermal imager for mass blind fever screening,” *Microvasc. Res.*, vol. 68, no. 2, pp. 104–109, 2004.
- [3] D. M. Bell, “Public health interventions and SARS spread, 2003,” *Emerg. Infect. Dis.*, vol. 10, no. 11, p. 1900, 2004.
- [4] J. R. Speakman and S. Ward, “Infrared thermography: principles and applications,” *Zoology-Jena-*, vol. 101, pp. 224–232, 1998.
- [5] M. Vollmer and K.-P. Möllmann, *Infrared thermal imaging: fundamentals, research and applications*. John Wiley & Sons, 2017.
- [6] Y. Zhou *et al.*, “Clinical evaluation of fever-screening thermography: impact of consensus guidelines and facial measurement location,” *J. Biomed. Opt.*, vol. 25, no. 9, p. 97002, 2020.
- [7] G. Sun, T. Matsui, T. Kirimoto, Y. Yao, and S. Abe, “Applications of infrared thermography for noncontact and noninvasive mass screening of febrile international travelers at airport quarantine stations,” in *Application of Infrared to Biomedical Sciences*, Springer, 2017, pp. 347–358.
- [8] A. Shajkofci, “Correction of human forehead temperature variations measured by non-contact infrared thermometer,” *IEEE Sens. J.*, 2021.
- [9] P. Viola, M. J. Jones, and D. Snow, “Detecting pedestrians using patterns of motion and appearance,” *Int. J. Comput. Vis.*, vol. 63, no. 2, pp. 153–161, 2005.
- [10] N. Dalal and B. Triggs, “Histograms of oriented gradients for human detection,” in *2005 IEEE computer society conference on computer vision and pattern recognition (CVPR’05)*, 2005, vol. 1, pp. 886–893.
- [11] R. Girshick, J. Donahue, T. Darrell, and J. Malik, “Region-based convolutional networks for accurate object detection and segmentation,” *IEEE Trans. Pattern Anal. Mach. Intell.*, vol. 38, no. 1, pp. 142–158, 2015.
- [12] S. Ren, K. He, R. Girshick, and J. Sun, “Faster r-cnn: Towards real-time object detection with region proposal networks,” *arXiv Prepr. arXiv1506.01497*, 2015.
- [13] J. Redmon, S. Divvala, R. Girshick, and A. Farhadi, “You only look once: Unified, real-time object detection,” in *Proceedings of the IEEE conference on computer vision and pattern recognition*, 2016, pp. 779–788.
- [14] W. Liu *et al.*, “Ssd: Single shot multibox detector,” in *European conference on computer vision*, 2016, pp. 21–37.
- [15] T.-Y. Lin, P. Goyal, R. Girshick, K. He, and P. Dollár, “Focal loss for dense object detection,” in *Proceedings of the IEEE international conference on computer vision*, 2017, pp. 2980–2988.

- [16] M. A. Fischler and R. A. Elschlager, "The representation and matching of pictorial structures," *IEEE Trans. Comput.*, vol. 100, no. 1, pp. 67–92, 1973.
- [17] Y. Yang and D. Ramanan, "Articulated pose estimation with flexible mixtures-of-parts," in *CVPR 2011*, 2011, pp. 1385–1392.
- [18] A. Toshev and C. Szegedy, "DeepPose: Human pose estimation via deep neural networks," in *Proceedings of the IEEE conference on computer vision and pattern recognition*, 2014, pp. 1653–1660.
- [19] S. Johnson and M. Everingham, "Clustered Pose and Nonlinear Appearance Models for Human Pose Estimation.," in *bmvc*, 2010, vol. 2, no. 4, p. 5.
- [20] S. Johnson and M. Everingham, "Learning effective human pose estimation from inaccurate annotation," in *CVPR 2011*, 2011, pp. 1465–1472.
- [21] B. Sapp and B. Taskar, "Modec: Multimodal decomposable models for human pose estimation," in *Proceedings of the IEEE Conference on Computer Vision and Pattern Recognition*, 2013, pp. 3674–3681.
- [22] K. He, G. Gkioxari, P. Dollár, and R. Girshick, "Mask r-cnn," in *Proceedings of the IEEE international conference on computer vision*, 2017, pp. 2961–2969.
- [23] G. Papandreou *et al.*, "Towards accurate multi-person pose estimation in the wild," in *Proceedings of the IEEE Conference on Computer Vision and Pattern Recognition*, 2017, pp. 4903–4911.
- [24] H.-S. Fang, S. Xie, Y.-W. Tai, and C. Lu, "Rmpe: Regional multi-person pose estimation," in *Proceedings of the IEEE International Conference on Computer Vision*, 2017, pp. 2334–2343.
- [25] E. Insafutdinov, L. Pishchulin, B. Andres, M. Andriluka, and B. Schiele, "Deepercut: A deeper, stronger, and faster multi-person pose estimation model," in *European Conference on Computer Vision*, 2016, pp. 34–50.
- [26] L. Pishchulin *et al.*, "Deepcut: Joint subset partition and labeling for multi person pose estimation," in *Proceedings of the IEEE conference on computer vision and pattern recognition*, 2016, pp. 4929–4937.
- [27] S. Kreiss, L. Bertoni, and A. Alahi, "Pifpaf: Composite fields for human pose estimation," in *Proceedings of the IEEE/CVF Conference on Computer Vision and Pattern Recognition*, 2019, pp. 11977–11986.
- [28] Y. Raaj, H. Idrees, G. Hidalgo, and Y. Sheikh, "Efficient online multi-person 2d pose tracking with recurrent spatio-temporal affinity fields," in *Proceedings of the IEEE/CVF Conference on Computer Vision and Pattern Recognition*, 2019, pp. 4620–4628.
- [29] A. Newell, Z. Huang, and J. Deng, "Associative embedding: End-to-end learning for joint detection and grouping," *arXiv Prepr. arXiv1611.05424*, 2016.
- [30] F. Xia, P. Wang, X. Chen, and A. L. Yuille, "Joint multi-person pose estimation and semantic part segmentation," in *Proceedings of the IEEE conference on computer vision and pattern recognition*, 2017, pp. 6769–6778.

- [31] Z. Cao, G. Hidalgo, T. Simon, S.-E. Wei, and Y. Sheikh, "OpenPose: realtime multi-person 2D pose estimation using Part Affinity Fields," *IEEE Trans. Pattern Anal. Mach. Intell.*, vol. 43, no. 1, pp. 172–186, 2019.
- [32] W. Luo, J. Xing, A. Milan, X. Zhang, W. Liu, and T.-K. Kim, "Multiple object tracking: A literature review," *Artif. Intell.*, p. 103448, 2020.
- [33] E. Bochinski, V. Eiselein, and T. Sikora, "High-speed tracking-by-detection without using image information," in *2017 14th IEEE International Conference on Advanced Video and Signal Based Surveillance (AVSS)*, 2017, pp. 1–6.
- [34] N. Wojke, A. Bewley, and D. Paulus, "Simple online and realtime tracking with a deep association metric," in *2017 IEEE international conference on image processing (ICIP)*, 2017, pp. 3645–3649.
- [35] P. Voigtlaender *et al.*, "Mots: Multi-object tracking and segmentation," in *Proceedings of the IEEE/CVF Conference on Computer Vision and Pattern Recognition*, 2019, pp. 7942–7951.
- [36] Z. Wang, L. Zheng, Y. Liu, and S. Wang, "Towards real-time multi-object tracking," *arXiv Prepr. arXiv1909.12605*, vol. 2, no. 3, p. 4, 2019.
- [37] X. Wang, "Intelligent multi-camera video surveillance: A review," *Pattern Recognit. Lett.*, vol. 34, no. 1, pp. 3–19, 2013.
- [38] M. Farenzena, L. Bazzani, A. Perina, V. Murino, and M. Cristani, "Person re-identification by symmetry-driven accumulation of local features," in *2010 IEEE computer society conference on computer vision and pattern recognition*, 2010, pp. 2360–2367.
- [39] L. Bazzani, M. Cristani, A. Perina, M. Farenzena, and V. Murino, "Multiple-shot person re-identification by hpe signature," in *2010 20th International Conference on Pattern Recognition*, 2010, pp. 1413–1416.
- [40] D. Gray and H. Tao, "Viewpoint invariant pedestrian recognition with an ensemble of localized features," in *European conference on computer vision*, 2008, pp. 262–275.
- [41] R. Zhao, W. Ouyang, and X. Wang, "Unsupervised salience learning for person re-identification," in *Proceedings of the IEEE conference on computer vision and pattern recognition*, 2013, pp. 3586–3593.
- [42] D. Chen, Z. Yuan, B. Chen, and N. Zheng, "Similarity learning with spatial constraints for person re-identification," in *Proceedings of the IEEE conference on computer vision and pattern recognition*, 2016, pp. 1268–1277.
- [43] Z. Li, S. Chang, F. Liang, T. S. Huang, L. Cao, and J. R. Smith, "Learning locally-adaptive decision functions for person verification," in *Proceedings of the IEEE conference on computer vision and pattern recognition*, 2013, pp. 3610–3617.
- [44] W.-S. Zheng, S. Gong, and T. Xiang, "Reidentification by relative distance comparison," *IEEE Trans. Pattern Anal. Mach. Intell.*, vol. 35, no. 3, pp. 653–668, 2012.
- [45] B. J. Prosser, W.-S. Zheng, S. Gong, T. Xiang, and Q. Mary, "Person re-identification by

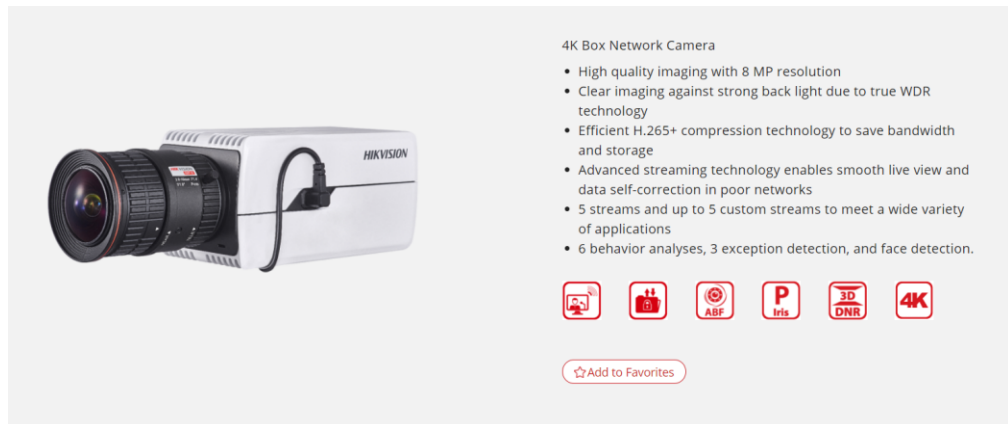
- support vector ranking,” in *BMVC*, 2010, vol. 2, no. 5, p. 6.
- [46] W. Li, R. Zhao, T. Xiao, and X. Wang, “Deepreid: Deep filter pairing neural network for person re-identification,” in *Proceedings of the IEEE conference on computer vision and pattern recognition*, 2014, pp. 152–159.
 - [47] D. Yi, Z. Lei, S. Liao, and S. Z. Li, “Deep metric learning for person re-identification,” in *2014 22nd International Conference on Pattern Recognition*, 2014, pp. 34–39.
 - [48] K. He, X. Zhang, S. Ren, and J. Sun, “Deep residual learning for image recognition,” in *Proceedings of the IEEE conference on computer vision and pattern recognition*, 2016, pp. 770–778.
 - [49] L. Zheng, L. Shen, L. Tian, S. Wang, J. Wang, and Q. Tian, “Scalable person re-identification: A benchmark,” in *Proceedings of the IEEE international conference on computer vision*, 2015, pp. 1116–1124.
 - [50] Z. Zheng, L. Zheng, and Y. Yang, “A discriminatively learned cnn embedding for person reidentification,” *ACM Trans. Multimed. Comput. Commun. Appl.*, vol. 14, no. 1, pp. 1–20, 2017.
 - [51] E. Dubrofsky, “Homography estimation,” *Diplomová práce. Vancouver: Univerzita Britské Kolumbie*, 2009.
 - [52] T. Togawa, “Non-contact skin emissivity: measurement from reflectance using step change in ambient radiation temperature,” *Clin. Phys. Physiol. Meas.*, vol. 10, no. 1, p. 39, 1989.
 - [53] S. Pokorni, “Error analysis of surface temperature measurement by infrared sensor,” *Int. J. Infrared Millimeter Waves*, vol. 25, no. 10, pp. 1523–1533, 2004.
 - [54] A. P. Miller, “Fitting Linear Models with Custom Loss Functions and Regularization in Python,” 2018. [Online]. Available: <https://alex.miller.im/posts/linear-model-custom-loss-function-regularization-python/>.
 - [55] Scipy.org, “Optimization and root finding (scipy.optimize).” [Online]. Available: <https://docs.scipy.org/doc/scipy/reference/optimize.html>.
 - [56] H. K. Walker, W. D. Hall, and J. W. Hurst, *Clinical methods: the history, physical, and laboratory examinations*. Butterworth-heinemann, 1990.
 - [57] “Thermal Imaging Systems (Infrared Thermographic Systems / Thermal Imaging Cameras),” *FDA*, 2021. [Online]. Available: <https://www.fda.gov/medical-devices/general-hospital-devices-and-supplies/thermal-imaging-systems-infrared-thermographic-systems-thermal-imaging-cameras%0A>.
 - [58] I. Fernández-Cuevas *et al.*, “Classification of factors influencing the use of infrared thermography in humans: A review,” *Infrared Phys. Technol.*, vol. 71, pp. 28–55, 2015.
 - [59] I. I. Geneva, B. Cuzzo, T. Fazili, and W. Javaid, “Normal body temperature: a systematic review,” in *Open forum infectious diseases*, 2019, vol. 6, no. 4, p. ofz032.
 - [60] W. H. Blahd, A. Husney, K. Romito, M. H. O’Connor, and D. Messenger, “Fever Temperatures: Accuracy and Comparison,” *C. S. Mott Children’s Hospital*, 2019.

- [Online]. Available: <https://www.mottchildren.org/health-library/tw9223>.
- [61] J. Redmon and A. Farhadi, "Yolov3: An incremental improvement," *arXiv Prepr. arXiv1804.02767*, 2018.
 - [62] S. Ren, K. He, R. Girshick, and J. Sun, "Faster r-cnn: Towards real-time object detection with region proposal networks," in *Advances in neural information processing systems*, 2015, pp. 91–99.
 - [63] MongoDB-Inc, "MongoDB Database," *MongoDB, Inc*, 2018.

Appendix

3.1 Hardware Specifications of RFSS

1. A Hikvision 8MP Box Camera: DS-2CD5085G0-(A)(P)



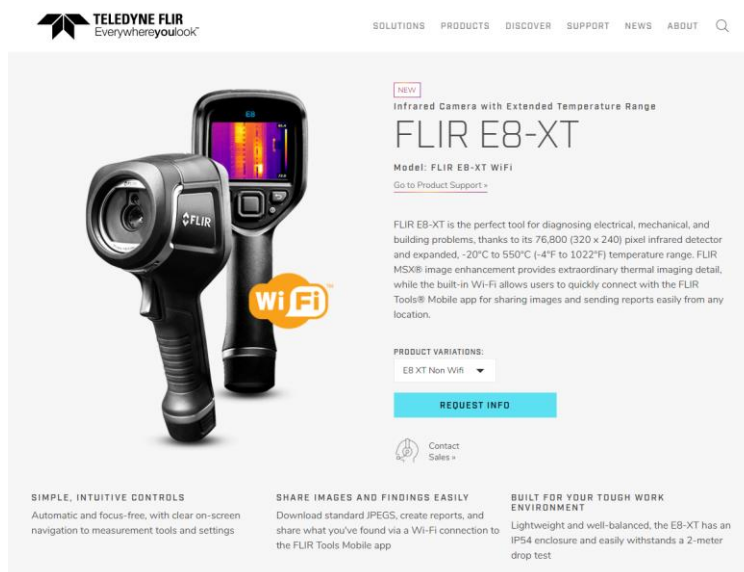
a.



DS-2CD5085G0-AP_datasheet_V5.6.0_2019C

b.

2. FLIR E8-XT



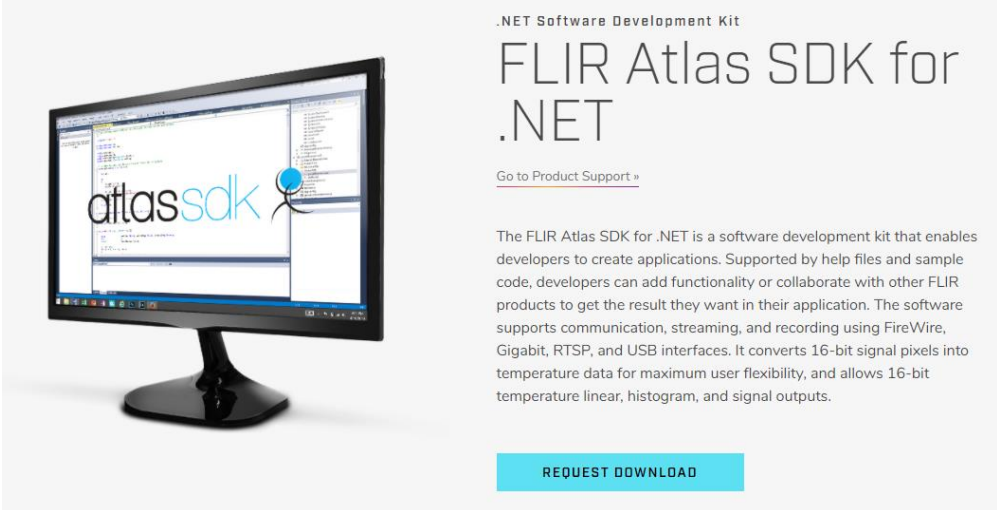
a.



Ex-Series-Datasheet-US.pdf

b.

c. FLIR ATLAS SDK:



The image shows a screenshot of the FLIR Atlas SDK for .NET product page. On the left, there is a monitor displaying the 'atlas sdk' logo and some code. On the right, the text reads: '.NET Software Development Kit', 'FLIR Atlas SDK for .NET', 'Go to Product Support »', and a paragraph describing the SDK. At the bottom right, there is a blue button labeled 'REQUEST DOWNLOAD'.

.NET Software Development Kit


FLIR Atlas SDK for .NET

[Go to Product Support »](#)

The FLIR Atlas SDK for .NET is a software development kit that enables developers to create applications. Supported by help files and sample code, developers can add functionality or collaborate with other FLIR products to get the result they want in their application. The software supports communication, streaming, and recording using FireWire, Gigabit, RTSP, and USB interfaces. It converts 16-bit signal pixels into temperature data for maximum user flexibility, and allows 16-bit temperature linear, histogram, and signal outputs.

[REQUEST DOWNLOAD](#)

3. FLIR A315



The image shows a screenshot of the FLIR A315 product page. On the left, there is a black thermal imaging camera. On the right, the text reads: 'IR Temperature Sensor with GigE (Motorized Focus)', 'FLIR A315', 'Model: FLIR A315', 'Go to Product Support »', and a paragraph describing the camera. Below the paragraph, there is a section for 'PRODUCT VARIATIONS:' with a dropdown menu showing 'FLIR A315'. At the bottom right, there is a blue button labeled 'REQUEST INFO' and a 'Contact Sales »' link.

IR Temperature Sensor with GigE (Motorized Focus)

FLIR A315

Model: FLIR A315

[Go to Product Support »](#)

The FLIR A315 is a compact and affordable thermal imaging camera, fully controlled by a PC. Due to its compliance to standards, the FLIR A315 is Plug and Play with third-party machine vision software such as National Instruments, Cognex, Matrox, MVTec, and Stemmer Imaging.

PRODUCT VARIATIONS:

FLIR A315

[REQUEST INFO](#)

[Contact Sales »](#)

a.



Ex-Series-Datasheet-US.pdf

b.

4. Logitech brio-4k-hdr-webcam



SPECS & DETAILS	SUPPORT
DIMENSIONS Webcam Height: 27 mm Width: 102 mm Depth: 27 mm Cable length: 2.2 m Weight: 63 g ATTACHABLE MOUNTING CLIP Height: 19 mm Width: 36 mm Depth: 63 mm Weight: 44 g SYSTEM REQUIREMENTS Compatible with Windows 7 or later (Windows 8.1 or higher required for resolutions greater than 1080p) macOS 10.10 or later Chrome OS™ 2 GB RAM or more needed for 1080p video streaming 1GB is typically needed for streaming 720p One USB 2 or USB 3 port (4K recording and streaming requires a USB 3.0 port and compatible third party software) Works with popular calling platforms	TECHNICAL SPECIFICATIONS Multiple resolutions 4K/30fps (up to 4096 x 2160 pixels) 1080p/30 or 60 fps (up to 1920 x 1080 pixels) 720p/30, 45, or 90 fps (up to 1280 x 720 pixels) Camera mega pixels: 13 Focus type: Autofocus Lens type: Glass Built-in mic: Stereo Mic range: Up to 1 m Diagonal field of view (dfov): 90°/78°/60° Digital zoom: 5x USB connectivity: USB-A plug-and-play, supports USB-C with third party adapter (not included) Detachable universal mounting clip fits laptops, LCD or monitors Rightlight™ 3 with HDR for clear image in various lighting environments ranging from low light to direct sunlight Image controls with optional Camera Settings application for control of pan, tilt, and zoom Infrared sensor technology for Windows (SDK available for application integration) Attachable privacy shutter
	PACKAGE CONTENTS Webcam with detachable universal mounting clip (on webcam) Attachable privacy shutter Travel bag 2.2 m USB-A to USB-C cable (USB 2.0 or 3.0) User documentation WARRANTY INFORMATION 3-year Limited hardware warranty PART NUMBER 960-001105

5. A computing unit (Intel Core i9 and NVIDIA RTX 2080 Super)

About

Your PC is monitored and protected.

[See details in Windows Security](#)

Device specifications

Device name	DESKTOP-9PT003
Processor	Intel(R) Core(TM) i9-10900KF CPU @ 3.70GHz 3.70 GHz
Installed RAM	64.0 GB
Device ID	ED8EC0B5-00D3-4C20-9586-2ADACE3BCC00
Product ID	00330-71257-35182-AAOEM
System type	64-bit operating system, x64-based processor
Pen and touch	No pen or touch input is available for this display

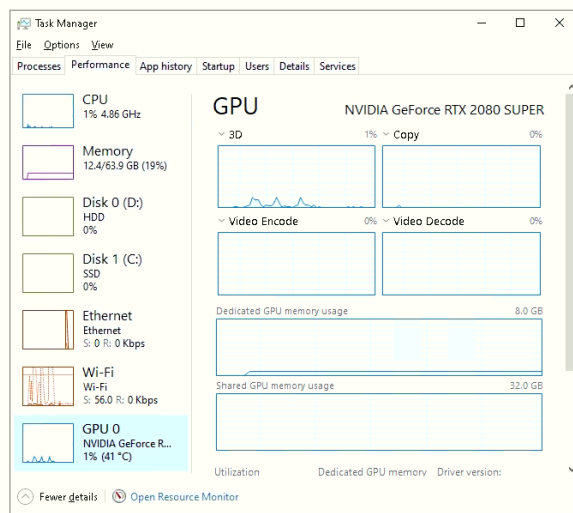
Copy

Rename this PC

Windows specifications

Edition	Windows 10 Pro
Version	20H2
Installed on	29/5/2021
OS build	19042.1052
Experience	Windows Feature Experience Pack 120.2212.2020.0

Copy



a.



DESKTOP-9PT003.txt

b. The specification of the desktop computer:

6. Environmental Sensor: 485 溫度濕度激光 PM2.5 感測器 PM10 檢測儀 MODBUS 粉塵空氣質量監測




a.

b. The specification of the environmental sensor:

产品参数

參數	技術參數
供電電	12V-24VDC
平均電流	<85mA
PM2.5/10測量範圍	0-1000ug/m3
PM2.5/10精度	<讀數的±10%(25°C)
溫度測量範圍	-40°C-80°C (可定製)
溫度精度	±0.5°C
濕度測量範圍	0-100%RH
濕度精度	±3%RH
穩定性	<2%F-S
非線性	<1%F-S
響應時間	≤120S
預熱時間	2min(可用)10min(最大精度)
質保期	整機2年(監視器質保1年)
輸出訊號	RS485/0-5V/0-10V/4-20mA
耗電	≤1.2W (@12V DC, 25°C)
工作壓力範圍	0.9-1.1atm

3.2 Infrared Thermometer FS-300



A handheld infrared thermometer with a white body and a black sensor tip. The digital display shows 36.8°C. It has buttons for 'MOD', 'MEM', and a power button.

DESCRIPTION	SPECIFICATION
Specification	
• BODY/ FOREHEAD	
Temperature range	34.0-42.50°C(93.2-108.5°F)
Accuracy	±0.2°C (36 ~39°C) ±0.3°C (34 ~35.9, 39.1-42.5°C)
• WIDE/ AMBIENT	
WIDE range	15-60°C(59-140°F)
Accuracy	±2°C or ±2%
Measurement Distance	2-3cm from the forehead center
Display type	LCD with back light
Power supply	DC3V (AAA 1.5V 2ea)
Running time	5,000 readings
Size / Weight	62.4*41.8*103.1mm / 120g

Link: <https://www.healthcarehk.com/product/hubdic-non-contact-infrared-thermometer-fs-300/>

3.3 Hot patches



3.4 Code for the analysis (the effects of distance, ambient temperature, and tracking)



analysis_code_nick_thesis.rar

3.5 Analysis of the effects of distance

Analysis on the FLIR E8 data:

Polynomial Regression Analysis: T_obj versus Distance

The regression equation is

$$T_{obj} = 35.40 - 0.7547 \text{ Distance} + 0.06273 \text{ Distance}^2 - 0.003007 \text{ Distance}^3$$

Model Summary

S	R-sq	R-sq(adj)
0.599628	71.33%	70.93%

Analysis of Variance

Source	DF	SS	MS	F	P
Regression	3	189.670	63.2235	175.84	0.000
Error	212	76.225	0.3596		
Total	215	265.896			

Sequential Analysis of Variance

Source	DF	SS	F	P
Linear	1	188.812	524.18	0.000
Quadratic	1	0.549	1.53	0.218
Cubic	1	0.309	0.86	0.355

STUDY1_NORMAL

Regression Analysis: T_obj versus Distance

Regression Equation

$$T_{obj} = 35.404 - 0.755 \text{ Distance} + 0.0627 \text{ Distance}^2 - 0.00301 \text{ Distance}^3$$

Coefficients

Term	Coef	SE Coef	T-Value	P-Value	VIF
Constant	35.404	0.524	67.63	0.000	
Distance	-0.755	0.323	-2.33	0.020	418.55
Distance*Distance	0.0627	0.0588	1.07	0.287	2062.69
Distance*Distance*Distance	-0.00301	0.00324	-0.93	0.355	675.04

Model Summary

S	R-sq	R-sq(adj)	R-sq(pred)
0.599628	71.33%	70.93%	70.25%

Analysis of Variance

Source	DF	Adj SS	Adj MS	F-Value	P-Value
Regression	3	189.670	63.2235	175.84	0.000
Distance	1	1.960	1.9597	5.45	0.020
Distance*Distance	1	0.410	0.4097	1.14	0.287
Distance*Distance*Distance	1	0.309	0.3093	0.86	0.355
Error	212	76.225	0.3596		
Lack-of-Fit	5	0.030	0.0060	0.02	1.000
Pure Error	207	76.195	0.3681		
Total	215	265.896			

Analysis on the FLIR A315 data:

STUDY1_A315

Regression Analysis: T_obj versus Distance

Regression Equation

$$T_{obj} = 36.291 - 0.454 \text{ Distance} + 0.0342 \text{ Distance}^2 - 0.00129 \text{ Distance}^3$$

Coefficients

Term	Coef	SE Coef	T-Value	P-Value	VIF
Constant	36.291	0.289	125.43	0.000	
Distance	-0.454	0.179	-2.54	0.012	418.55
Distance*Distance	0.0342	0.0325	1.05	0.294	2062.69
Distance*Distance*Distance	-0.00129	0.00179	-0.72	0.473	675.04

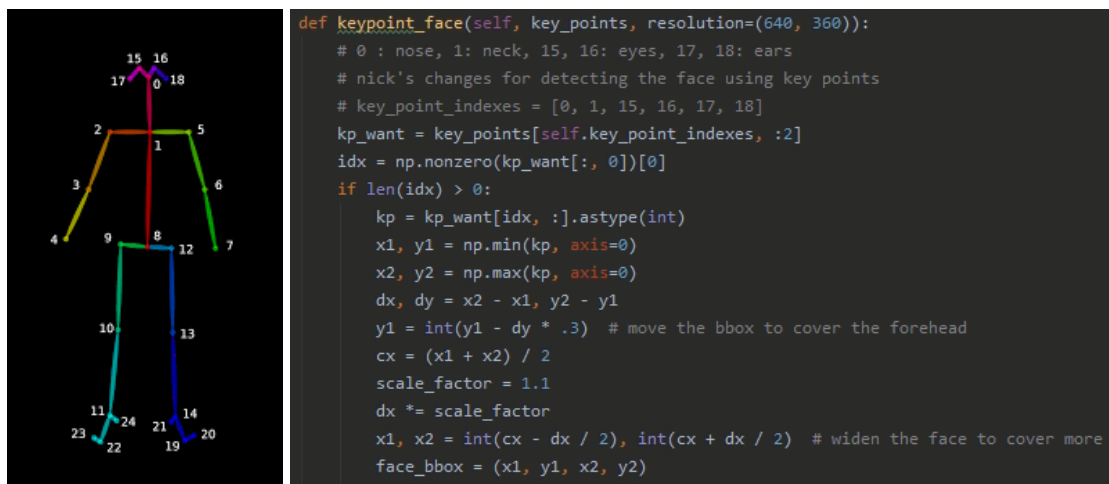
Model Summary

S	R-sq	R-sq(adj)	R-sq(pred)
0.331411	71.16%	70.75%	70.08%

Analysis of Variance

Source	DF	Adj SS	Adj MS	F-Value	P-Value
Regression	3	57.4405	19.1468	174.33	0.000
Distance	1	0.7098	0.7098	6.46	0.012
Distance*Distance	1	0.1218	0.1218	1.11	0.294
Distance*Distance*Distance	1	0.0568	0.0568	0.52	0.473
Error	212	23.2847	0.1098		
Lack-of-Fit	5	0.0403	0.0081	0.07	0.996
Pure Error	207	23.2443	0.1123		
Total	215	80.7252			

4.1 Face box estimation with Open-Pose



The photo in the left shows the 25 Open-Pose key point outputs (<https://github.com/CMU-Perceptual-Computing-Lab/openpose>), and the right shows the definition of the face box estimation from the key point.

4.2 Motion filter

KNN “Background Subtractor” was used as the motion filter. First, the raw thermal frame was converted to a gray image. The temperature value within the range of 20°C and 60°C will be mapped linearly to 0 and 255. Values below 20°C are mapped to 0, and values above 60°C are mapped to 255. The code is shown below:

```
frame_thermal_bg = temp2img(temperature_array)
motion_mask_thermal = motion_detector_thermal.apply(frame_thermal_bg)
motion_mask_thermal[motion_mask_thermal > 0] = 1
```

```
bs_buffer_len = 500 * 3
motion_detector_thermal = cv2.createBackgroundSubtractorKNN(history=bs_buffer_len, dist2Threshold=4 ** 2,
                                                             detectShadows=False)
```

```
frame_thermal_bg = temp2img(temperature_array)
motion_mask_thermal = motion_detector_thermal.apply(frame_thermal_bg)
motion_mask_thermal[motion_mask_thermal > 0] = 1
```


4.3 Data calibration at HKUST North Gate



Key point data and the diagonal length of the face bounding box are collected for calibrating the distance in the collected data from 27 September 2020 to 01 March 2021.

4.4 Analysis of the effects of ambient temperature

STUDY2

Regression Analysis: temperature versus ambient

Regression Equation

temperature = 21.34 + 0.667 ambient - 0.01342 ambient*ambient
+ 0.000186 ambient*ambient*ambient

Coefficients

Term	Coef	SE Coef	T-Value	P-Value	VIF
Constant	21.34	1.44	14.85	0.000	
ambient	0.667	0.204	3.28	0.001	5144.50
ambient*ambient	-0.01342	0.00943	-1.42	0.155	21982.17
ambient*ambient*ambient	0.000186	0.000143	1.30	0.194	6017.51

Model Summary

S	R-sq	R-sq(adj)	R-sq(pred)
1.20182	54.32%	54.31%	54.29%

Analysis of Variance

Source	DF	Adj SS	Adj MS	F-Value	P-Value
Regression	3	22224.1	7408.04	5128.94	0.000
ambient	1	15.5	15.51	10.74	0.001
ambient*ambient	1	2.9	2.92	2.02	0.155
ambient*ambient*ambient	1	2.4	2.43	1.68	0.194
Error	12938	18687.2	1.44		
Lack-of-Fit	582	2123.2	3.65	2.72	0.000
Pure Error	12356	16563.9	1.34		
Total	12941	40911.3			

6.1 Equipment list

1. Fixed System at Hong Kong International Airport

Description	Brand	Model	Qty.
8 Mega-Pixel Video Camera	HIKVISION	DS-2CD5085G0-(A)(P)	4
12 Mega-Pixel Video Camera with lens	HIKVISION	DS-2CD5AC5G0-IZ(H)S	2
Stereo Depth Sensor	StereoLabs	ZED	4
Wireless Router	ASUS	ROG Rapture GT-AC5300	1
Ethernet to USB Convertor	ORICO	UTJ-U3	2
24-port LAN Switcher	CISCO	SG550X-24MP	2
Wireless Tablet	Samsung	Galaxy Tab S4	2
Mobile Device	Samsung	Galaxy S10	1

Specification of the GPU Server:

Supermicro GPU Server: SYS-4029GP-TRT (max. support 8x 2080Ti)

Chassis: CSE-418GTS-R4000BP2, 4U Rackmount (5U for Geforce card)

PSU: 2000W (2+2) Redundant Power Supplies

M/B: X11DPG-OT-CPU, C622 / Dual Socket P (LGA 3647) / 24xDIMM / 2x10GbE

CPU: Intel® Xeon® Gold 6136 Processor 24.75M Cache, 3.00 GHz [x2]

RAM: 16GB DDR4 2666 ECC RDIMM [x16]

SSD: M.2 2.0TB NVMe Solid State Drive [x1]

SSD: 2.5" 4TB SATA3 6Gb/s Samsung 860 EVO Series MLC [x8]

GPU: NVIDIA(INNO3D) GeForce RTX 2080Ti Jet [x6]

Top Cover: MCP-230-41803-0N for 4029GP-TRT [x1]

6.2 Thermal block

- Thermal block:



XMT7100 溫控器 7110智能PID溫度控制儀

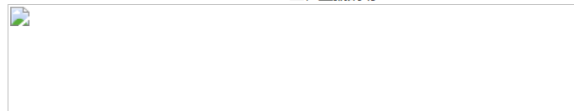
一、特點

- 小體積、高性能，全輸入，特別適合小型設備溫度控制系統
- 熱電阻、熱電偶共10種溫度訊號兼容輸入，精度高、響應快
- PID控制可選繼電器有接觸點式或SSR電平無接觸點式輸出
- XMT7100帶1路繼電器輸出，XMT7110帶2路繼電器輸出
- PID恆溫控制，上、下限區間溫度控制兼容
- PID自整定功能，自動適應被控制對象
- 儀表可按攝氏度或華氏度顯示溫度值

二、技術參數

1. 工作電源：AC/DC85~260V(其它電壓可定製)
2. 輸入訊號：熱電偶：T、R、J、B、S、K、E、WRe3-WRe25
熱電阻：Pt100、Cu50
3. 整機功耗：小於2W
4. 採樣速率：4次/秒
5. 超限顯示：“EEEE”
6. 顯示顏色：紅色LED (其它色可定製)
7. 顯示範圍：輸入訊號全量程
8. 基本誤差：0.2%FS±1個字
9. SSR電平：DC 8V/30mA
10. 接觸點容量：AC250V/3A
11. 使用環境：0~50°C；≤85% RH

三、型號說明



XMT7100 溫控器 7110智能PID溫度控制儀 一、特點 •小體積、高性能，全輸入，特別適合小型設備溫度控制系統 •熱電阻、熱電偶共10種溫度訊號兼容輸入，精度高、響應快 •PID控制可選繼電器有接觸點式或SSR電平無接觸點式輸出 •XMT7100帶1路繼電器輸出，XMT7110帶2路繼電器輸出 •PID恆溫控制，上、下限區間溫度控制兼容 •PID自整定功能，自動適應被控制對象 •儀表可按攝氏度或華氏度顯示溫度值 二、技術參數 1. 工作電源：AC/DC85~260V(其它電壓可定製) 2. 輸入訊號：熱電偶：T、R、J、B、S、K、E、WRe3-WRe25 熱電阻：Pt100、Cu50 3. 整機功耗：小於2W 4. 採樣速率：4次/秒 5. 超限顯示：“EEEE” 6. 顯示顏色：紅色LED (其它色可定製) 7. 顯示範圍：輸入訊號全量程 8. 基本誤差：0.2%FS±1個字 9. SSR電平：DC 8V/30mA 10. 接觸點容量：AC250V/3A 11. 使用環境：0~50°C；≤85% RH 三、型號說明

- 0.3mm latex sheet pasted on the thermal block:

精致款光头套（优质乳胶材质）



○

6.3 RFSS User feedbacks

		CSE	QC	LCSP	NPEC	SCO	SPWE	STEH	SW	TKP	TW	TWH	
0: not satisfied; 1: satisfied	1 Are you satisfied with the technology for trial and trial(s) conducted?	1	1	1	1	1	1	1	1	1	1	1	
0: no; 1: yes	2 Do you think that the technology will bring benefits to the operation of your organisation?	1	1	1	1	1	1	1	1	1	1	1	
	3 In what area(s) do you think the technology is of benefit to your organisation?												
	Improve production capability	0	1	0	0	0	0	0	0	0	0	0	
	Improve product quality	0	0	1	0	0	0	0	0	0	0	0	
	Improve service quality	0	0	1	1	1	1	1	0	0	0	0	
	Reduce production / product cost	0	0	0	1	0	0	0	0	0	0	0	
	Enhance job opportunities	0	0	0	0	0	0	0	0	0	0	0	
	Gain reputation from the industry	0	0	0	0	0	0	0	0	0	0	0	
	Process enhancement	1	1	1	1	1	1	1	1	1	1	1	
	Manpower saving	0	0	0	0	0	0	0	1	0	1	0	
0: no; 1: yes; 0.5: not sure.	4 Are you willing to adopt the technology if it is available in the market?	0.5	1	1	1	1	0	1	1	1	0.5	1	
		cost & needs									cost, maintenance, support		
	5 Why do you consider the technology not useful to your organisation?												
	The technology is not delivered as expected												
	The technology is no longer relevant to the needs of my organisation												
	others												
	6 Do you have any suggestions for further improving the technology from a user's points of view?	detect bac better han stability, a-aesthetic t too sensi aesthetic display ter stability of connectio display ter aesthetic											
	7 How satisfy are you with the overall performance of the Project Coordinator or project team?												
	8 Any other comments												